COMPUTATIONAL AND EXPERIMENTAL STUDIES OF TRANSITION METAL CARBONATE PRECURSORS AS CATHODES FOR LITHIUM-ION BATTERIES

by

MOGAHABO TEBOGO MORUKULADI

RESEARCH DISSERTATION

Submitted in fulfilment of the requirement for the degree of

DOCTOR OF PHILISOPHY

In

Physics

In the

FACULTY OF SCIENCE & AGRICULTURE

(School of Physical & Mineral Sciences)

at the

UNIVERISTY OF LIMPOPO (Turf loop Campus)

SUPERVISOR: Prof P.E Ngoepe

Co- SUPERVISORS: Dr M.C Masedi

: Dr N.N Ngoepe

2024

Declaration

I declare that the thesis hereby submitted to the University of Limpopo (Turf-loop Campus) for the degree Doctor of philosophy Science has not previously been submitted by me or any other person for a degree at this or any other institution, that it is my own work both in design and execution, and that all materials contained herein has been duly acknowledged.

Ms MT Morukuladi

Signature

Dedications

This work is dedicated to my delightful mom Molatelo Rebecca Morukuladi and my sisters Emily, Girly and Charlotte Morukuladi, thank you for encouraging me to further my studies, your support strengthened me daily and I really appreciate it. If it were not by your daily advices, i wound not have been here. This work is also dedicated to my kids Ofentse and Lethabo. Moreover, the work is also dedicated to my lovely late sister Maria and my late father Matee Johannes Morukuladi, may your precious souls continue to rest in peace my lovely sister and bopapa.

Acknowledgement

First and foremost, I would like to thank God of mount Zion for being with me throughout my academic journey. I also want to express my sincere gratitude and appreciation to my supervisor Prof P.E Ngoepe and core-supervisors, Dr N.N Ngoepe and Dr M.C Masedi for their great patience, professional guidance and continuous support during my studies. My colleagues at the Materials Modelling Centre (MMC) are also appreciated for the helpful discussions and countless friendship. Last but not least, I would like to express my deepest gratitude to my wonderful family, they stood by me in all circumstances i encountered during my studies and supported each and every decision I took, for that I thank and love you so much.

The financial support from the National Research Foundation SASAC is also highly appreciated for funding my PhD and also funding my research collaboration with the University of Kent for the synchroton based techniques through the SASAC mobility grant of the British council.

Abstract

This study investigates the layered oxide cathode with NMC-type $LiNixMnyCozO_2$ as the alternative cathode material for lithium ion batteries. This material has attracted the researcher's interest as alternative cathode material due to its low cost and less toxicity as compared to the most widely commercialised lithium cobalt oxide (LCO). Lithium nickel manganese cobalt oxide (often abbreviated as NMC) is a type of cathode material used in lithium-ion batteries. It's a popular choice because it offers a balance of high energy density, good cycling stability and relatively low cost compared to other cathode materials. In this study we investigate the stability properties of $Ni_{0.3}Mn_{0.5}Co_{0.2}CO_3$ and $Ni_{0.3}Mn_{0.5}Co_{0.2}O_2$, respectively. In particular, we focus on the manganese rich compositions and minor amounts of nickel and cobalt. We further doped both system ($Ni_{0.3}Mn_{0.5}Co_{0.2}CO_3$ and $Ni_{0.3}Mn_{0.5}Co_{0.2}O_2$) with fluorine, titanium, niobium and chromium to check if their contributions could improve or disprove the behaviour of $Ni_{0.3}Mn_{0.5}Co_{0.2}CO_3$ and $Ni_{0.3}Mn_{0.5}Co_{0.2}O_2$ materials.

Firstly, the structural, electronic, mechanical and vibrational properties of $Ni_{0.3}Mn_{0.5}Co_{0.2}CO_3$, $Ni_{0.3}Mn_{0.5}Co_{0.2}O_2$ and their doped systems have been calculated using the density functional theory employing the pseudo-potential plane-wave approach within the local gradient approximation with the Hubbard parameter U for strongly correlated transition metals. The structural property calculations included the equilibrium lattice parameters, density and energy of formations while electronic properties included the partial density of states (PDOS), total density of states (TDOS) and band structures for all the systems. Furthermore, mechanical properties investigated the elastic constants, Pugh ratio and anisotropy while vibrational properties investigates the phonon dispersion curves for $Ni_{0.3}Mn_{0.5}Co_{0.2}CO_3$, $Ni_{0.3}Mn_{0.5}Co_{0.2}O_2$ and their doped systems. The calculated lattice parameters and energy of formation could be

used for benchmarking in the future since no similar work was found in literature for comparison. Moreover, the calculated energy of formations revealed the relatively low and negative values for all the systems, suggesting thermodynamic stability. With the band structures, we found that $Ni_{0.3}Mn_{0.5}Co_{0.2}CO_3$ and $Ni_{0.3}Mn_{0.5}Co_{0.2}O_2$ structures were semiconductors with a direct gap of 0.004 eV and 0.036 eV with their doped systems also indicating metallic characteristics. Moreover, the partial density of states for our materials and their doped systems were also found to be metallic as there was no energy band gap observed at the Fermi line. Furthermore, the elastic constants revealed that all our systems recorded 21 independent elastic constants which falls within the triclinic lattice systems. For a material to be considered mechanically stable within the triclinic system, there are conditions to be satisfied, hence $Ni_{0.3}Mn_{0.5}Co_{0.2}CO_3$ satisfied all the conditions suggesting mechanical stability while $Ni_{0.3}Mn_{0.5}Co_{0.2}O_2$ did not satisfy all the conditions implying mechanical instability. The phonon dispersion curves revealed that $Ni_{0.3}Mn_{0.5}Co_{0.2}CO_3$ was vibrationally stable while $Ni_{0.3}Mn_{0.5}Co_{0.2}O_2$ was vibrationally unstable due to the presence of negative vibrations along the Brillouin zone. Furthermore, the phonon dispersion curves for doped systems revealed that some are vibrationally stable while some are vibrationally unstable.

Secondly, since the study focuses on manganese rich systems, cluster expansion technique was used to generate phases in the manganese rich side. From the results, various phases with varied concentrations and symmetries were produced by the ground-state phase diagram. The accuracy of new structures during cluster expansion fitting is indicated by the cross validation score (CVs) for all of the generated new structures being less than 5meV per active atom position. Since all of the developed structures have CVs below 5meV, this indicate that our calculations were valid and the newly generated structures will work realistically. From the phase diagram, we noticed that all the predicted phases are in the negative energy of formations

side (miscible constituent) which indicate thermodynamic stability. Moreover, of all the phases generated within the diagram, only phases in the manganese rich side were explored by using first principles calculations to further confirm their stability properties by determining their structural, electronic, mechanical and vibrational properties. The energy of formation results revealed that all the phases are thermodynamically stable while electronic properties revealed metallic characteristic for all the phases in the Mn-rich side. For mechanical properties, we found that few phases did not satisfy the triclinic conditions which implies mechanical instability while other phases were found to satisfy the conditions, indicating mechanical stability.

Lastly, the carbonate co-precipitation method was used in this study to synthesize the transition metal carbonate precursors using a 4L stirred tank reactor (CSTR) under steady state circumstances. We produced $Ni_{0.28}Mn_{0.53}Co_{0.19}CO_3$ and $Ni_{0.17}Mn_{0.67}Co_{0.17}CO_3$ which was later lithiated to form $LiNi_{0.33}Mn_{0.53}Co_{0.14}O_2$ and $LiNi_{0.17}Mn_{0.67}Co_{0.17}O_2$ as our layered cathodes. Both the lithiated samples were further characterized for thermogravimetric analysis, x-ray diffractions, morphologies, EDX and XRF. Thermogravimetric analysis revealed thermodynamic stability for both samples while XRD's also managed to produce the most crystalline peak at 003 indexing. The scanning electron microscopy was also tested to determine the particle size and distribution for both samples and the results revealed a homogeneous particle distribution in each sample. We further collaborated with University of Kent for the usage of the synchrotron beam of the Diamond light source to determine the effect of fluorination on our NMC samples. In particular, we wanted to check if fluorination reduces or increases the oxidation states of metals within our samples and results revealed that fluorination does not change the oxidation state of our samples.

Table of Content

List of Figures

List of Tables

List of Abbreviations

BCC : Base Centred Cubic

CE : Cluster Expansion

CVs : Coefficient of Variations

DFT : Density Functional Theory

DOS : Density of States

FCC : Face Centred Cubic

GGA : Generalized Gradient Approximation

LA : Longitudinal Acoustic

LDA : Local Density Approximation

LCO : Lithium Cobalt Oxide

LIBS : Lithium Ion Batteries

LO : Longitudinal Optical

$MnCO_3$: Manganese Carbonate

$NiCO_3$: Nickel Carbonate

NMC : Nickel Manganese Cobalt

PAW : Project Augmented Wave

PW : Plane-Waves

SIESTA : Spanish Initiative for Electronic Simulations with Thousand Atoms

TA : Transverse Acoustic

TO : Transverse Optical

U : Hubbard Parameter

UNCLE : Universal Cluster Expansion

VASP : Vienna ab initio Simulation Package

SEM : Scanning electron microscopy

XRD : X-ray Diffraction

NiCd : Nickel Cadmium

NiMH : Nickel-metal hydride

PSD : Particle size distribution

NMC : Nickel, manganese, cobalt

$LiFePO_4$: Lithium iron phosphate

LCA : Lithium Nickel Cobalt Aluminium Oxide

LTO : Lithium titanate

LMO : Lithium Manganese Oxide”

Chapter 1

1.1. Introduction

Lithium-ion batteries (LIB) are rechargeable energy storage devices that have become global in modern electronics and are increasingly important in electric vehicles and grid energy storage systems [1, 2, 3]. They are known for their high energy density, relatively low self-discharge rate, and lack of memory effect compared to other rechargeable batteries like nickel-cadmium (NiCd) or nickel-metal hydride (NiMH) batteries [4]. Of all the different types of batteries available and currently commercialised, lithium-ion batteries (LIBs) have gained a significant segmentation in the market and are the most promising and the fastest growing battery technology [5]. A LIB cell is typically made up of two opposing electrodes, a positive electrode known as the cathode and a negative electrode known as the anode, both of which are in contact with a lithium ion rich liquid or a solid (polymer or ceramic) electrolyte. A third component known as a separator separates the two electrodes, cathode and anode, and is permeable to Li-ions but impermeable to oxygen. The performance and stability of a Li-ion battery depend on the properties of its components such as cathode, anode, electrolyte, and separator [6, 7, 8]. The basic working principle of a typical LIB cell is demonstrated in Figure 1-1. Among these components, the cathode currently acts as a limiting factor that controls a large degree of the operation voltage and storage capacity [9]. Cathodes are also essential components that directly influence the LIB's performance, energy density, cycle life and safety [10, 11]. Hence, the development of high performance with low cost cathodes is necessary to reduce the cost of LIBs. Furthermore, Innovations in cathode materials and designs are critical for advancing battery technology and enabling the development of more efficient, durable, and safer energy storage solutions for various applications.

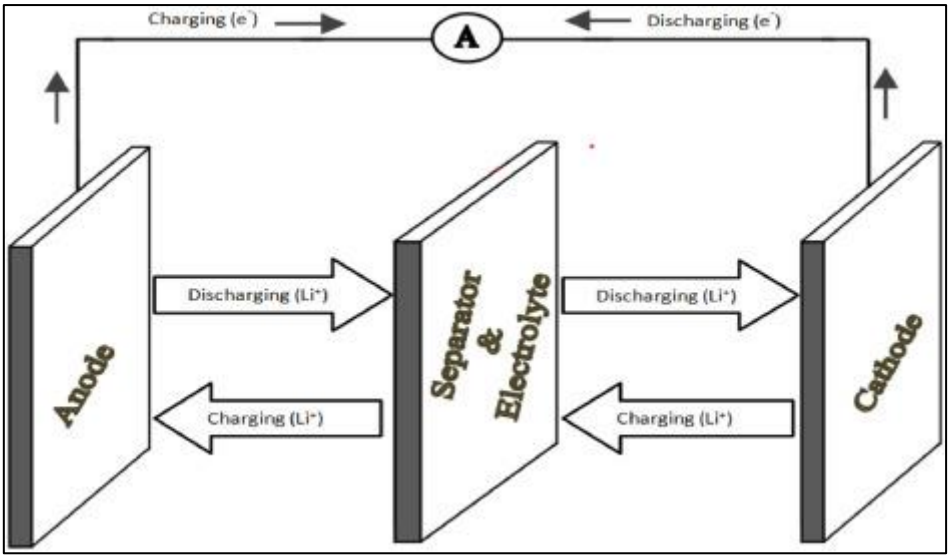

Figure 1-1. Schematic diagram of Li-ion battery cell [12].

There are several types of cathode materials used in lithium-ion batteries, each with its own unique properties, advantages, and applications. Some common types includes Lithium Cobalt Oxide ($LiCoO_2$), Lithium Iron Phosphate ($LiFePO_4$), Lithium Manganese Oxide (LMO), lithium titanate (LTO) and recently, Lithium Nickel Cobalt Aluminium Oxide (NCA) and Lithium Nickel Manganese Cobalt Oxide (NMC) [13]. Amongst all these cathode materials, $LiCoO_2$ (LCO) was the most widely used and commercialised cathode material [14], however this material was found to be toxic, very expensive and exhibiting low theoretical capacity of 140 mAh/g when cycled between 3V and 4.2V hindering the widespread application in lithium-ion batteries [15]. While lithium iron phosphate (LiFePO4) cathodes offered several advantages such as excellent thermal stability, safety, and long cycle life, they also had some disadvantages such as lower energy density, limited voltage, power density, high cost, limited temperature performance and voltage fade. Moreover, Lithium Nickel Cobalt Aluminium Oxide (NCA) cathodes offer several advantages including high energy density, good cycling stability, and high specific capacity. However, they also have some disadvantages such as thermal stability, high cost, limited cycle life and voltage fade. Furthermore, Lithium

Manganese Oxide (LMO) cathodes offer several advantages including good thermal stability, safety, and cost-effectiveness. However, they also have some disadvantages such lower energy density, limited voltage, reduced cycle life and voltage fade. Figure 1-2 compares the cost, lifespan, performance, safety, specific energy, and power of these cathode materials and among them all, the NMC cathode has the best all-around performance.

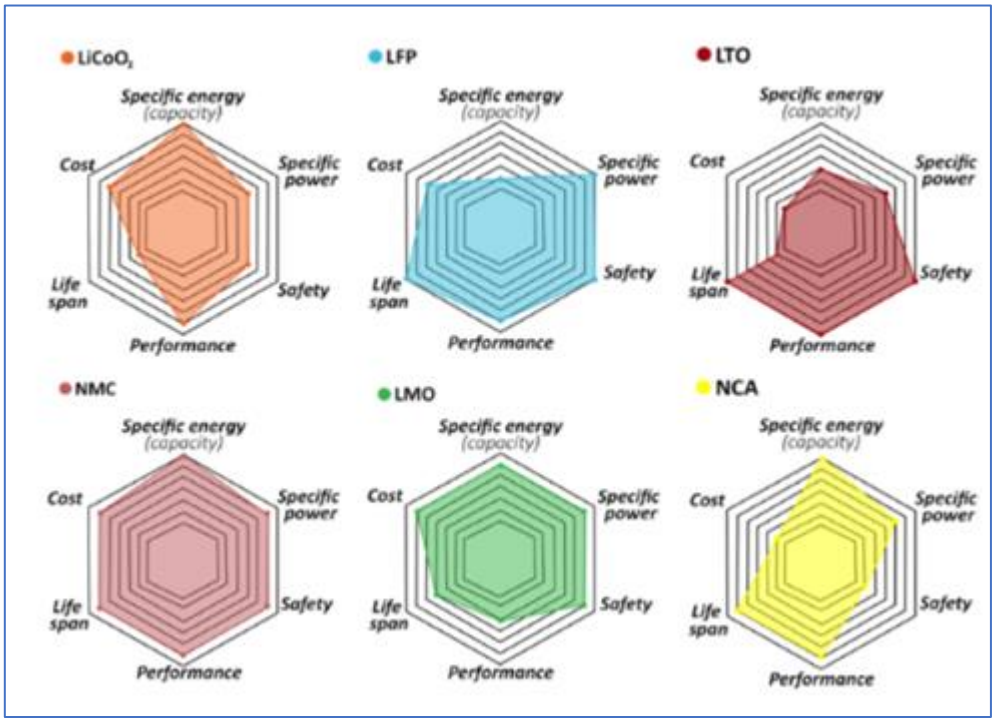

Figure 1-2. Comparison of different types of cathode materials for lithium ion batteries [16]

Due to the reported disadvantages of the well-known cathode materials for lithium ion batteries, there has been an extensive quest for researchers to find alternative cathode materials which exhibits high volumetric density and high specific reversible discharge capacity at low cost for application in Li-ion batteries [17, 18, 19]. As such, due to its advantages, NMC cathode has gained the popularity in the global LIBs market. Layered cathode materials are comprised of nickel, manganese and cobalt elements and known as NMC or $LiNi_xMn_yCo_zO_2$ ($x + y + z = 1$) [20]. NMC has attracted a lot of attention in the battery industry as the alternative

cathode material for lithium ion batteries due to its low cost, environmental benign, high energy density, improved cycle life and high specific capacity of > 250mAh/g as compared to LCO system [21]. Compared to cobalt-based cathodes like lithium cobalt oxide ($LiCoO_2$), NMC cathodes exhibit improved stability, reduced thermal runaway, and lower cost [22, 23, 24]. NMC's encompass a range of compositions with different ratios of nickel (Ni), manganese (Mn), and cobalt (Co). These variations result in different performance characteristics, making them suitable for various applications. Combination of nickel, manganese and cobalt elements in NMC crystal structure, as shown in Figure 1-3 is reported to have a good structural stability.

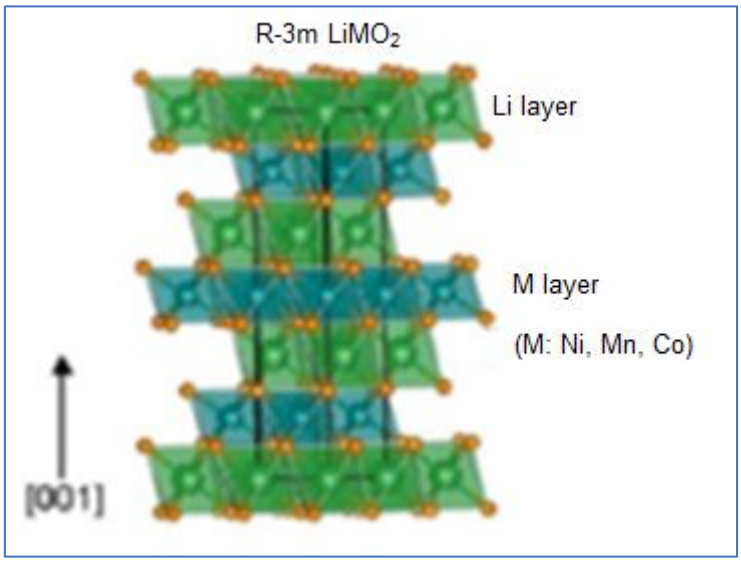

Figure 1-3. Crystal structure of R-3m $LiMO_2$ layered oxide (M: Ni, Mn and Co) [25].

NMC's are widely applied in electric vehicle (EV) systems as they deliver higher discharge capacity and greater mile-range per charge. The diversity in NMC materials is because of the different composition of nickel, cobalt, and manganese, forming Ni-rich NMC cathodes, Co-rich NMC cathodes and Mn-rich NMC cathodes with various compositions for each element [26, 27].

Nickel-rich NMC's contains a higher proportion of nickel as compared to manganese and cobalt. It offers higher energy density and specific capacity, making it particularly suitable for

applications requiring higher energy storage capacity, such as long range electric vehicles (EVs) [28, 29]. Ni-rich NMC also offers the highest energy density with reduced cobalt content, making it cost-effective and environmentally friendly [30, 31, 32]. However, Ni-rich NMC cathodes are prone to capacity fading, severe surface reactivity and structural uncertainty which eventually lead to deterioration of performances [33, 34, 35]. They are also prone to voltage fade, where the cell's operating voltage gradually decreases over repeated charge-discharge cycles. This phenomenon is attributed to structural changes, phase transitions, and side reactions at the electrode-electrolyte interface, leading to irreversible capacity loss and reduced energy storage efficiency over time. Furthermore, Ni-rich NMC cathodes may also exhibit reduced thermal stability compared to other cathode materials, particularly at high states of charge or elevated temperatures. Thermal instability can lead to accelerated degradation, increased risk of thermal runaway, and safety hazards such as cell venting, fire, or explosion, posing challenges for battery safety and reliability [36, 37].

While on the other hand, Mn-rich NMC's contains a higher proportion of manganese as compared to nickel and cobalt. Although the Ni-rich NMC cathode materials have been studied extensively, the experimental and computational investigations on Mn-rich NMC cathodes are relatively limited [38, 39, 40]. As such in this study we investigate the Mn-rich NMC's as promising cathode materials for lithium ion batteries as they offer a high discharge capacity of 230 mAh g−1 as compared to the traditional $LiCoO_2$, $LiMn_2O_4$, and $LiFePO_4$ cathodes, when operated above 4.6 V [41, 42, 43]. Mn-rich NMC cathodes can achieve high energy densities due to their composition of nickel, manganese, and cobalt. This combination allows for a balance between specific energy and power density, making them suitable for various applications ranging from consumer electronics to electric vehicles and grid storage. Moreover, Mn-rich NMC cathodes can offer improved cycle life compared to other cathode materials,

such as lithium iron phosphate (LiFePO4) or lithium manganese oxide (LMO). This increased cycle life is attributed to the stable crystal structure and minimal capacity fade observed during charge-discharge cycling, leading to longer-lasting batteries with extended operational lifetimes. Therefore, to explore the impact of Mn concentration on NMC-based cathodes and to understand the effect that composition can have on rate capability of these high energy density electrodes, for this study we prepared the following compositions: $Ni_{0.3}Mn_{0.5}Co_{0.2}CO_3$ and $Ni_{0.3}Mn_{0.5}Co_{0.2}O_2$ and calculated their stability properties using both computational and experimental methods.

Due to current advances in computer techniques, computational methods have become widely used in materials science research [44]. These methods allow the calculation of material properties without the need for actual synthesis, which allows obtaining properties that are difficult to measure experimentally in a short time and with limited resources. Computational methods can calculate various properties of cathode materials including electrochemical performance [45], thermal, chemical and structural stability [46]. These computational approaches' qualities allow them to get around the resource and time constraints of the experimental methods that are currently in use. To create a material with perfect properties, the ideal atomic arrangement can be predicted in advance, which can shorten the amount of time needed for modelling before experimentation [47, 48, 49]. Furthermore, by comparing the computational results to the experimental data, it is possible to ascertain a high level of computational accuracy. This, in turn improves the reliability of computational results. As a result, computations and experiments can complement one another, leveraging their respective strengths and deficiencies.

1.2. Cathode Materials for Lithium ion batteries

Cathode materials are critical components of lithium-ion batteries influencing their energy density, voltage, cycle life, safety, cost, and sustainability [50, 51, 52]. Advances in cathode material development and optimization are essential for driving improvements in battery performance, enabling the transition to cleaner energy solutions, and addressing the evolving needs of diverse applications ranging from consumer electronics to electric transportation and grid energy storage. [53, 54]. When compared to the electrolyte and anode electrode, the cathode electrode of LIB is the heaviest and most expensive component. Due to the ever-increasing energy and power demands from various energy-hungry sources, there has been a lot of interest in improving the performance of Lithium-ion batteries by focusing on high-performing cathode materials [55, 56]. Cathode material being a key component in lithium-ion batteries, is one of the primary way for the improvement of energy-density of lithium-ion battery [57, 58]. Currently, the widely researched and commercially used cathode materials mainly include the lithiated transition metal oxide, spinel and polyanion compounds including layered-type structure compounds such as $LiMO_2$ (M=Ni, Co, Mn), Lithium-rich materials $xLi_2MO_3 \cdot_{(1-x)} LiM'O_2$ (M=Mn, Fe, Co), spinel-type structure compounds LiM_2O_4 (M=Mn, Co, Ni), olivine-type structure compounds $LiMPO_4$ (M=Fe, Co, Mn), tavorite-type structure compounds $LiMPO_4F$ (M=Fe, V), borate-type compounds $LiMBO_3$ (M=Fe, Co, Mn) and silicate-type compounds Li_2MSiO_4 (M=Fe, Mn, Co) [59, 60]. So far, the crystal structure of the commonly used cathode material, the mechanism of Li^+ intercalation/de-intercalation and the fine-structure change on electrochemical performance of LIBs have been intensely studied. Fig.1-4 shows the crystal structure of each commonly used cathode materials.

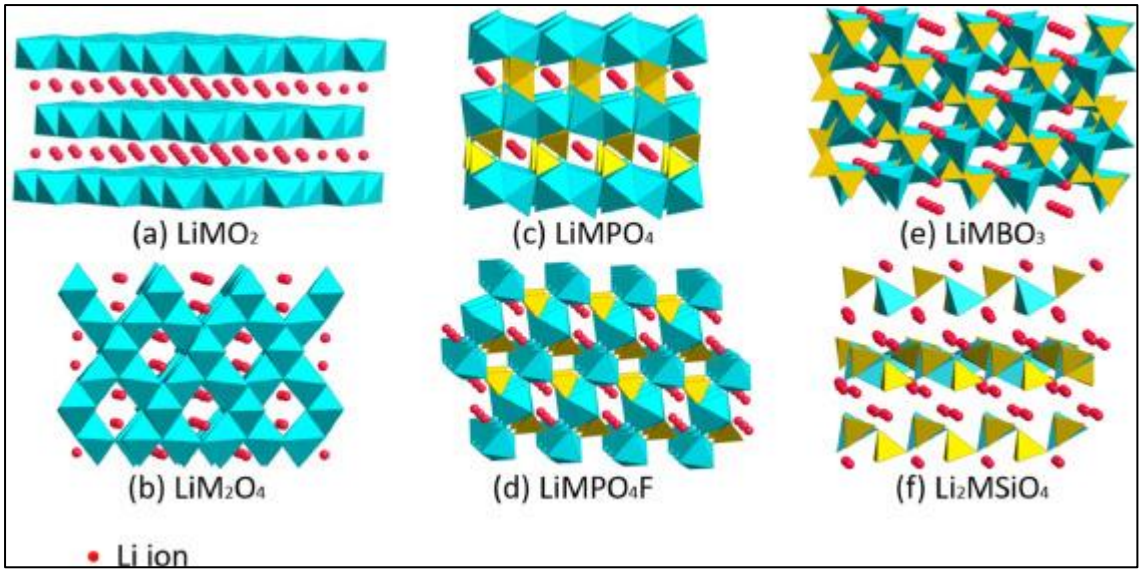

Figure 1-4. Crystal structures for (a) $LiMO_2$, (b) LiM_2O_4, (c) $LiMPO_4$, (d) $LiMPO_4F$, (e) $LiMBO_3$ and (f) Li_2MSiO_4 [61].

The crystal structure of $LiMO_2$ series cathode materials is bedded rock-salt. The tightly packed oxygen ions combined with transition metal ions located at the octahedral positions form stable MO_2 layers with lithium ions embedded between the layers as shown in Fig. 1-4 (a). Although the structure grants the transition metal elemental lithiated oxides with a relatively large mass and volumetric theoretical capacity, the actual specific capacity only reaches half of it. Furthermore, their high cost and thermal instability are unavoidable disadvantages. To overcome some of these issues, binary and ternary layered cathode materials have been developed by partially elemental substitutions. Ohzuku et al. firstly revealed the electrochemical properties of binary $LiNi_{0.5}Mn_{0.5}O_2$ [62] followed by ternary nickel cobalt manganese $LiNi_xCo_yMn_zO_2$ cathode materials with different weight proportion which have been explosively investigated [63]. Figure 1-5 (a) shows the development process on layered-structured cathode materials. In recent days, the researcher's effort has turned to the Ni-rich, Mn-rich and Co-free directions to obtain cathode material for LIBs with the balance of electrochemical performances and eco-friendly. With the advancement of research on layered-

type cathode materials, lithium and manganese-rich materials are now regarded as one of the most promising cathode materials for LIBs.

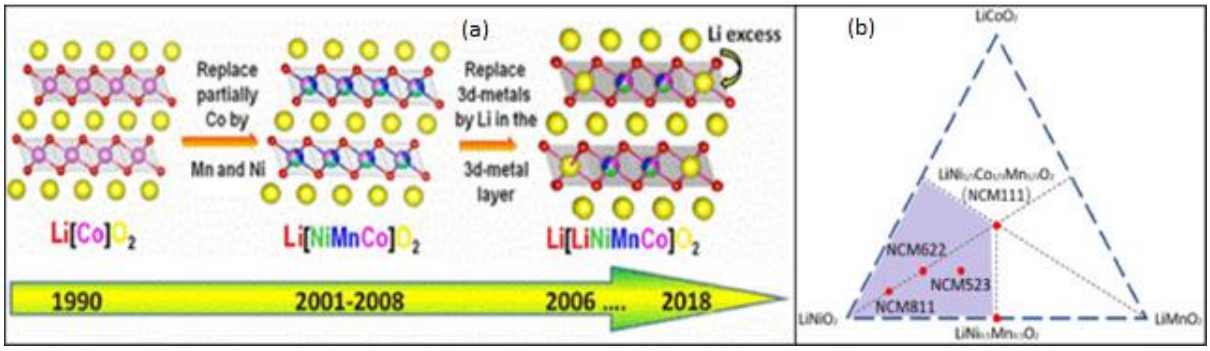

Figure 1-5. (a) The development of layered $LiMO_2$ cathode and (b) Schematic diagram of the compositional phase related to $LiMO_2$ (M: Ni, Mn, Co). The shaded part represent the nickel rich layered cathode material [64].

1.3. Rationale

Of all the different types of batteries available and currently developed, lithium-ion batteries (LIBs) have gained a significant segmentation in the market and are the most promising and the fastest growing battery technology [5, 65, 66]. They offer very high energy densities, have low self-discharge and can operate at higher voltage of 3.7V compared to other battery candidates, which offer only up to 1.2V [67]. Since Li-ion batteries are the first choice source of portable electrochemical energy storage, improving their performance and reduction of high costs can greatly expand their applications and enable new technologies which depend on energy storage. The performance of any Li-ion battery greatly depends on the physical and chemical properties of the cathode material, which serves as a host for Li ions. Lithium cobalt oxide ($LiCoO_2$) has been the most widely used and commercialised cathode material due to its good capacity and energy density [14]. However this material was reported to have disadvantages such as poor thermal stability, low cyclic stability, high cost, toxicity and safety issues [68, 69]. As a result, there has been an extensive quest for researchers to find cathode materials with high volumetric density and high specific reversible discharge capacity for the

application in Li-ion batteries. Therefore, three classes of metal oxide cathodes have been discovered such as olivine, spinel and layered. Olivine structure has a one-dimensional diffusion pathway. Metal oxide cathodes offer advantages such as low cost and high thermal stability, yet suffers from poor electronic conductivity and low energy density. Thus, cathode materials with olivine structure are not ideal for applications that require high volumetric energy density. With a three-dimensional diffusion pathway, spinel structure materials have high electrical and lithium ion conductivity to achieve good reversibility during the charge-discharge process. Layered cathode shows high capacity, high energy density and high working voltage [70]. The layered structure is undoubtedly the most practical and promising cathode material for lithium ion batteries.

Layered $LiNiMnCoO_2$ composites have recently attracted a lot of interest as alternative high energy density cathode due to their low cost and less toxicity than the most widely commercialised LCO [71, 72]. The $LiNiMnCoO_2$ material also served as an alternative cathode because it can be charged to higher cut-off potentials due to the presence of Mn^{4+}, which stabilizes the structure and delivers higher practical capacities (>160 mAh/g). NMC can exist in several different stoichiometric ratios between the Ni, Mn and Co atoms [73]. These different compositions can affect various properties such as structural stability, chemical stability and capacity. Ni, Mn and Co contributes to enhance the performance of $LiNMCO_2$ in different ways. Ni-rich compositions demonstrate high discharge capacity [74], Mn-rich compositions maintain better cycle life and thermal safety [75] while Co-rich compositions provide excellent rate capability. Composite lithium and manganese rich compounds have even become more attractive cathode materials due to their high capacity and also improved structural stability [76, 77]. However the electrochemical performance of these composites materials strongly depends upon the physical properties of the precursor materials that serve as source for lithium

[78]. Co-precipitation is a popular approach to synthesise precursors for transition metal oxide cathode materials used in lithium-ion batteries. Currently, Li-ion battery materials largely use the hydroxide co-precipitation to produce the transition metal hydroxide precursors [79]. The problem with hydroxide co-precipitation is that oxidation of the cation is possible, which means cations may oxidise to higher than the 2^+ valency, specifically manganese oxidation leading to deviation from the desired stoichiometry [80, 81]. Hence, using this method for precursor preparation is quite difficult. Meanwhile, with carbonate co-precipitation, the +2 valence of Mn and the cations are stable in an aqueous solution. Therefore, the carbonate co-precipitation method is considered to be more effective for industrial applications due to the ease of reproducibility [82, 83]. Hence, in this work we investigate the structural, energetic, electronic, elastic and vibrational properties of the Mn-rich NMC with high concentration of Mn and low concentrations of Ni and Co by mimicking their stability trends at ambient conditions. In particular, we calculate their cell parameters, heats of formation, band structures, density of states, elastic constants and phonon dispersion curves using computational techniques. We further synthesize the Mn-rich NMC using the semi-batch carbonate co-precipitation method to check their morphology, X-ray diffraction and particle size distributions. Furthermore, we also investigate the phase stability of ternary $NMCCO_3$ precursors considered for this study by generating their phase diagrams using the cluster expansion method. Hence, we hope to produce more improved, desirable and non-toxic Mn-rich NMC cathode for Li-ion batteries.

1.4. Doping NMC's

Doping Nickel Manganese Cobalt Oxide (NMC) cathodes involves introducing small amounts of additional elements into the crystal lattice of the material. Advantages of doping involve performance enhancement, voltage stability and cost reduction [84, 85]. Doping can improve the electrochemical performance of NMC cathodes by modifying their electronic and structural

properties. In this study we doped with elements like fluorine (F), chromium (Cr), titanium (Ti) and niobium (Nb) to stabilize the crystal structure and enhance lithium ion diffusion kinetics leading to improved charge/discharge rates and better cycling stability.

Fluorine doping can help enhance the structural stability of Mn-rich NMC cathodes by stabilizing the crystal lattice and minimizing structural distortions during charge and discharge cycles [86]. This can mitigate phase transitions, reduce strain on the electrode material, and improve the cycling stability of the battery, leading to longer-lasting and more reliable energy storage systems [87]. Fluorine doping can enhance the electrochemical performance of Mn-rich NMC cathodes by optimizing the lithium ion diffusion kinetics and charge transfer processes. This can result in higher specific capacities, improved rate capabilities, and lower polarization, enabling the battery to deliver higher power outputs and support faster charging and discharging. Moreover, Fluorine doping can contribute to improved voltage stability of Mn-rich NMC cathodes during cycling [88]. By minimizing voltage fade and maintaining a more stable operating voltage, fluorine-doped NMC cathodes can enhance the energy efficiency and capacity retention of lithium-ion batteries, ensuring consistent performance over the battery's lifespan.

Furthermore, doping Mn-rich NMC cathodes with chromium, titanium and niobium holds promises for optimizing the performance, stability, safety of lithium-ion batteries, contributing to the development of high-performance energy storage solutions for various applications including electric vehicles, grid energy storage, and portable electronics [89, 90, 91]. Further research and development efforts are needed to fully understand the mechanisms and optimize the synthesis methods of doped NMC cathodes to unlock their full potential and accelerate their commercialization.

1.5. Intensions of the study

Portable electronic gadgets are becoming increasingly popular for communication, data processing, entertainment and other applications. Furthermore, the idea of widespread commercial use of electric vehicles is becoming more and more realistic. These advancements have created a demand for the continuous development of more efficient batteries with a variety of critical features. Rechargeable lithium batteries have proven to be one of the most successful solutions to achieve these goals for low load applications. A crucial key towards a good battery design is concerned with the choice of cathode material. So since the cathode material has a crucial role in accelerating popularization and adaptation of the Li-ion secondary battery, developing an optimum cathode material with high energy density, long cycle life and excellent thermal stability have become a hot topic around the world. Hence in this thesis we investigate the layered transition metal carbonate precursors as cathode materials for high energy density lithium ion batteries.

In particular, we investigate the stability properties of $NiMnCoCO_3$, $NiMnCoO_2$ with high concentration of Mn and minor amounts of Ni and Co using first-principles density functional theory with Hubbard correction (DFT+U). The Hubbard U parameter is introduced to deal with the strongly correlated systems [92]. We employ plane-wave pseudopotential techniques as embodied in Vienna ab-initio simulation package (VASP) code for equilibrium ground-state properties and the PHONON code [93] for determining their vibrational frequencies. We further synthesized Mn-rich NMC carbonates under semi-batch mode using carbonate co-precipitation method to investigate their morphologies. The main purpose of this work is to attain the elementary and fundamental understanding on the stability properties of Mn-rich $NiMnCoCO_3$. Computationally, four properties will be determined to investigate the stabilities; namely structural, thermodynamic, electronic and mechanical. In the case of structural and

thermodynamic properties, the equilibrium cell parameters and heats of formation (ΔH_f) will be calculated, where the structure with stable equilibrium volume and more negative ΔH_f value will be considered the most stable phase. Further investigations on stability properties will be performed by computing the electronic density of states, in particular observing electronic states behaviour near the Fermi level with respect to the band gap. We will perform first-principles phonon dispersion calculations, which play an important role in determining vibrational properties of materials. The elastic constants, bulk modulus, shear modulus and Young's modulus and anisotropy factors to evaluate the elasticity of structures will be calculated. Finally, the thermogravimetric analysis will be calculated to check the changes in the mass of material as a function of time either at a selected temperature or over a particular temperature range. X-ray diffractions will also be calculated to study the crystalline structure of our materials. Furthermore, Scanning Electron Microscopy was used to reveal details about the particle size, shape, distribution, and surface features of these materials.

1.6. Outline of the study

Chapter 1 consists of general introduction of the study, cathode materials for lithium ion batteries, applications, the rationale and intensions of the study.

Chapter 2 discusses theoretical aspects and methodologies used throughout this work, in particular the computational techniques and the experimental techniques such as density functional theory, cluster expansion and carbonate co-precipitation.

Chapter 3 presents the calculations in details, results, discussions on structural properties lattice parameters, electronic properties and mechanical properties of pure $NMCCO_3$, $NMCO_2$, doped $NMCCO_3$ and doped $NMCO_2$ structures where ab initio methods have been invoked.

Chapter 4 consists of cluster expansion back round for ternary phase diagram. This chapter also outlines the First principles calculations for the newly generated phases found in the manganese rich side.

Chapter 5 discusses the experimental results for $NMCCO_3$ materials and compare with available experimental data.

Chapter 6 Finally, a short summary of the main results presented in this thesis, several recommendations for future research and references are listed in this chapter.

Chapter 2

Computational and Experimental Methods

2.1. Introduction

In this chapter we report on the theoretical background and computational methods used in this study. We will use computer simulation techniques, which provide an alternative method of investigating material properties (via computers), in which the simulator creates a model of a real system and investigates its behaviour. The mathematical model is physically based, and the investigation is carried out on a computer. In many ways, these simulation studies are similar to experimental investigations. However, in a simulation, there is complete control and access to detail, and if enough computer power is available, exact answers for the model can be obtained. The ab initio method is the most well-known computational technique. Ab initio is a group of methods for calculating the properties of materials, such as the values of the fundamental constants and the atomic numbers of the atoms present, using the Schrödinger equation. Density functional theory (DFT), Hartree-Fock (HF), and post-Hartree-Fock (PHF) methods are among them. We will only use density functional theory to predict the ground-state energies of many-body systems in this study. We also discuss the plane-wave pseudopotentials, VASP and PHONON codes that are embedded in the MedeA software. Furthermore, carbonate co-precipitation method will also be used to synthesize the transition metal carbonate precursors.

2.2. Density Functional Theory

Density functional theory (DFT) is a quantum mechanical theory used in physics and chemistry to study the electronic structure and ground state properties of many body systems. The theory

was based on formulae by Hohenberg and Kohn [92] Sham in the 1960's using two theorems to provide the foundation of accurate calculations. The first theorem states that for any system of interacting particles in an external potential$V(r)$, the external potential is uniquely determined by the ground state density [93]. This theorem provides essential foundation for reducing a many-body system by the use of functional of the electron density.

$$E = E[\rho] \tag{2-1}$$

Where E is the total energy and ρ is the electron density. In DFT, the total electron density is decomposed into one-electron density which is constructed from one-electron wave functions. The idea of using the electron density as the fundamental entity of a quantum mechanical theory of matter originates in the early days of quantum mechanics in the 1920's, especially from the work of Thomas and Fermi [94]. However, in the subsequent decades, it was rather the Hartree-Fock approach [95], which was developed and applied to small molecular systems. Calculations on realistic solid state systems were then out of reach. In 1951, Slater [96] used ideas from the electron gas with the intention to simplify Hartree-Fock theory to a point where electronic structure calculations on solids became feasible. Slater's work, which led to the so-called $X\alpha$ method, has contributed tremendously to the development of electronic structure calculations. In solid-state systems, the electron density is a scalar function defined at each point r in real space,

$$\rho = \rho(r) \tag{2-2}$$

The electron density and the total energy depend on the type and arrangements of the atomic nuclei. Therefore, one can write

$$E = E\left[\rho(r), \{R_\alpha\}\right] \tag{2-3}$$

where the set $\{R_\alpha\}$ denotes the positions of all atoms in the system under consideration. Equation (2-3) is the key to an atomic-scale understanding of electronic, structural and dynamic properties of matter. If one has a way of evaluating expression (2-3), one can for example, predict the equilibrium structure of solid and predict the reconstruction of surfaces and the equilibrium geometry of molecules adsorbed on surfaces. Furthermore, the derivative of the total energy (2-3) with respect to the nuclear position of an atom gives the force acting on that atom. This enables the efficient search for stable structures and more importantly for the study of dynamical processes such as diffusion or the reaction of molecules on surfaces. Most of the considerations discussed here are based on the Born-Oppenheimer approximation [97] in which it is assumed that the motions of the electrons are infinitely faster than those of the nuclei. In practice this means that the electronic structure is calculated for a fixed atomic arrangement and the atoms are then moved according to classical mechanics. This is a fairly good approximation for heavy atoms like tungsten (W), but may cause errors for light atoms such as hydrogen (H) or lithium (Li).

In density functional theory, the total energy is decomposed into three contributions namely; a kinetic energy (T_0), Coulomb energy due to classical electrostatic interactions among all charged particles in the system (U) and a term called exchange-correlation energy (E_{XC}) that captures all many-body interactions.

$$E = T_0 + U + E_{XC}. \qquad (2\text{-}4)$$

Where T_0 is the kinetic energy, U is the Coulomb energy and E_{XC} is the exchange correlation energy. It is purely classical and contains the electrostatic energy arising from the Coulomb attraction between electrons and nuclei, the repulsion between all electronic charges and the repulsion between nuclei. It can be written as follows;

$$U = U_{en} + U_{ee} + U_{nn} \quad , \tag{2-5}$$

with

$$U_{en} = -e^2 \sum_{\alpha} Z_{\alpha} \int \frac{\rho(r)}{|r - R_{\alpha}|} dr \quad , \tag{2-6}$$

$$U_{ee} = e^2 \iint \frac{\rho(r)\rho(r')}{|r - r'|} dr dr' \quad , \tag{2-7}$$

$$U_{nn} = e^2 \sum_{\alpha\alpha'} \frac{Z_{\alpha} Z_{\alpha'}}{|R_{\alpha} - R_{\alpha'}|} \quad , \tag{2-8}$$

where e is the elementary charge of a proton and $Z'_{\alpha}$is the atomic number of atom α. The summations extend over all atoms and the integrations over all space. Once the electron density, atomic numbers and positions of all atoms are known, expression (2-6) to (2-8) can be evaluated by using the techniques of classical electrostatics.

In density functional theory, the "real" electrons of a system are replaced by "effective" electrons with the same charge, mass and density distribution. However, effective electrons move as independent particles in an effective potential, whereas the motion of a "real" electron is correlated with those of all other electrons. T_0 is referred to as the sum of kinetic energies of all effective electrons moving as independent particles. Often, one does not explicitly make this distinction between real and effective electrons.

If each effective electron is described by a single particle wave function, Ψ_i then the kinetic energy of all effective electron in the system is given by the following equation.

$$T_0 = \sum n_i \int \psi_i^*(r) \left[-\frac{\hbar^2}{2m} \nabla^2 \right] \psi_i(r) dr \tag{2-9}$$

Expression (2-9) is the sum of the expectation values of one-particle kinetic energies were n_i denotes the number of electrons in state i, Ψ_i is a single particle wave-function and [$\frac{-\hbar^2}{2m}\nabla^2$] is the time dependent Schrödinger equation. By construction, the dynamical correlations between the electrons are excluded from T_0.

The third term of Eq. (2-4) which is called the exchange-correlation energy, E_{xc} includes all remaining complicated electronic contributions to the total energy. The Hohenberg-Kohn-Sham theorem [98], which is a central part of density functional theory, states that the total energy is at its minimum value for the ground state density and that the total energy is stationary with respect to first-order variations in the density as shown in equation 2-10.

$$\left.\frac{\partial E[\rho]}{\partial \rho}\right|_{\rho=\rho_0} = 0 \qquad (2\text{-}10)$$

In conjunction with the kinetic energy, we have introduced one-particle wave-function $\Psi_i(r)$, which generate the electron density.

$$\rho(r) = \sum_i n_i |\psi_i(r)|^2 \qquad (2\text{-}11)$$

where n_i denotes the occupation number of the eigenstate i, which is represented by the one-particle wave function Ψ_i. By construction, $\rho(r)$ in Eq. (2-11) is the exact many-electron density.

The goal of the next step is the derivation of equations that can be used for practical density functional calculations. The variational condition (2-10) can be used to derive the conditions for the one-particle wave-functions that lead to the ground state density. To this end, one

substitutes Eq. (2-11) in expression (2-10) and varies the total energy with respect to each wave function. This procedure leads to the following equations:

$$[\frac{\hbar^2}{2m}\triangle^2 + V_{eff}(r)]\varphi_i(r) = \varepsilon_i\varphi_i(r) \; where \; V_{eff}(r) = V_c(r) + \mu_{xc}[\rho(r)] \tag{2-12}$$

Equations (2-12) are called the Kohn-Sham [99] equations. The electron density, which corresponds to these wave-functions, is the ground state density which minimizes the total energy. As a consequence of the partitioning of the total energy (2-4), the Hamiltonian operator in the Kohn-Sham equations (2-12) contains three terms, one for the kinetic energy, the second for the Coulomb potential and the third for the exchange-correlation potential. The kinetic energy term is the standard second-order differential operator of one-particle Schrödinger equations and its construction does not require specific knowledge of a system. In contrast, the Coulomb potential operator, $V_c(r)$ and the exchange-correlation potential operator, depend on the specific electron distribution in the system under consideration. The Coulomb or electrostatic potential $V_c(r)$ at point r is generated from the electric charges of all nuclei and electrons in the system. It can be evaluated directly in a real space using equation 2-13 as follows;

$$V_C(r) = -e^2\sum_{\alpha}\frac{Z_\alpha}{|r-R_\alpha|} + e^2\int\frac{\rho(r')}{|r-r'|}dr' \tag{2-13}$$

In condensed systems it is more convenient to use Poisson's equation shown in 2-14

$$\nabla^2 V_C(r) = -4\pi e^2 q(r) \tag{2-14}$$

to calculate the electrostatic potential. Here, $q(r)$ denotes both the electronic charge distribution $\rho(r)$ and the positive point charges of the nuclei at positions R_α. The exchange-correlation potential is related to the exchange-correlation energy by equation 2-15 below.

$$\mu_{xc}(r) = \frac{\partial E_{xc}[\rho(r)]}{\partial \rho(r)} \tag{2-15}$$

Equation (2-15) is formally exact in the sense that it does not contain any approximations to the complete many-body interactions. Therefore, from the above discussions, the Kohn-Sham total energy functional can be expressed as;

$$E = \frac{1}{2}\sum_{occ} \varepsilon_i + U_{nn} - \frac{e^2}{2}\iint \frac{\rho(r)\rho(r')}{|r-r'|} dr dr' + E_{xc}[\rho(r)] - \int \rho(r)\mu_{xc} dr \tag{2-16}$$

In practice however, the exchange-correlation energy (and thus the exchange-correlation potential) is not known and one has to make approximations which will be discussed in the next section.

2.3. "Approximation Methods

2.3.1. Local density approximation

Local density approximation (LDA) is a set of approximations to the E_{xc} functional in DFT that is determined by the electronic density at each point in space. LDA demonstrates that E_{xc} is similar to that for a locally uniform electron gas with similar density in regions where there is slow variation in charge density [100]. Several different schemes have been developed for obtaining approximate forms for the functional exchange-correlation energy. The simplest accurate approximation, for non-magnetic systems is to assume that the exchange-correlation energy is dependent only on the local electron density $d(r)$ around each volume element. Local density approximation (LDA) gives the correct sum rule for the exchange correlation hole [101].In the local density approximation the exchange correlation energy is given by equation 2-17;

$$E_{xc}[\rho] \approx \int \rho(r)\varepsilon_{xc}^{0}[\rho(r)]dr \tag{2-17}$$

Where $\rho(r)$ is the electron density while ε_{xc}^{0} denotes the exchange correlation potential. The exchange-correlation energy is taken from the known results of the many-electron interactions in an electron system of constant density (homogeneous electron gas). The exchange-correlation energy of the total molecule or solid is the integral over the contributions from each volume element. LDA is based upon two basic assumptions; the first being that exchange and correlation effects are mainly from the immediate locality of point r and the second being that these exchange and correlation effects are slightly independent on the alteration of the electron density in the locality of r [102]. The fulfilment of these two conditions results in the same contribution from the volume element dr as if this volume element was surrounded by a constant electron density $\rho(r)$ of the same value within dr. For this study we have utilised the LDA+U method which has been widely implemented to correct the approximate DFT xc functional. The LDA+U method works in the same way as the standard LDA method to describe the valence electrons. However, for the strongly correlated electronic states (d and f orbitals), the Hubbard model is implemented for a more accurate modelling. Therefore, the total energy of the system (E_{LDA+U}) is typically the summation of standard LDA energy functional (E_{Hub}) for all the states and the energy of the Hubbard functional that describes the correlated states. Based on the simplified $LDA + U$ form, it has been customary to utilise the effective U parameter as shown in equation 2-18, instead of the interaction U parameter.

$$U_{eff} = U - J \tag{2-18}$$

Where the "J" parameter is known as the exchange interaction term which accounts for Hund's rule coupling.

2.3.2. Generalized gradient approximation

Gradient-corrected density functional as suggested by Perdew [103], Becke [104], Wang [105] and Perdew, Burke and Ernzerhof [106] offer a remedy to the LDA discussed above. The basic idea with these schemes is the inclusion of terms in the exchange-correlation expressions that depend on the gradient of the electron density and not only on its value at each point in space. Therefore, these corrections are also sometimes referred to as "non-local" potentials. Table 2.1 gives the form suggested by Becke (1988) for the exchange part and Perdew (1986) for the correlation. Energies are given in Hartree atomic units; the units for the electron and spin densities are number of electrons / (Bohr radius)^3. The constant b in Becke's formula is a parameter fitted to the exchange energy of inert gases. The explicit form of the functions f and g in Perdew's expression for the correlation energy is given in the original paper by Perdew [106]. While dissociation energies calculated with these corrections rival in accuracy the best post-Hartree-Fock quantum chemistry methods, gradient corrected density functional calculations are computationally much less demanding and more general. Gradient corrected density functionals have been studied extensively for molecular systems, for example by Andzelm and Wimmer [107].The results are very encouraging and this approach could turn out to be of great value in providing quantitative thermochemical data. The one-particle eigenvalues obtained from the gradient-corrected exchange-correlation potentials are not significantly different from the LDA eigenvalues. Therefore, these potentials do not (and are not intended to) remove the discrepancy between calculated and measured energy band gaps.

Table 2-1. Gradient-correction to the total energy for exchange by Becke and correlation by Perdew.

$E_{GGA} = E_{LSD} + E_x^G + E_c^G$

Becke (1988) Gradient-corrected exchange	$E_x^G = b\sum_\sigma \int \frac{\rho_\sigma x^2{}_\sigma}{1+6bx_\sigma \sinh^{-1} x_\sigma} dr$ $x_\sigma = \frac{\lvert\nabla\rho\rvert}{\rho_\sigma^{4/3}} \qquad \sigma = \uparrow or \downarrow$
Perdew (1986) Gradient-corrected correction	$E_c^G = \int f(\rho_\uparrow, \rho_\downarrow) e^{-g(\rho)\lvert\nabla\rho\rvert} \lvert\nabla\rho\rvert^2 dr$

The use of GGA has little influence on local properties and tends to overestimate the bond lengths and cell parameters, but does lead usually to a significant improvement in global changes in the total energy, such as those that result when two atoms combine to make a molecule. In this work, we used the Perdew Burke Ernzerhof [106] form of the LDA+U, which was designed to be more robust and accurate for metallic systems.

2.4. Plane-wave pseudopotential method

2.4.1. Plane-waves and pseudopotentials

Plane-waves and pseudopotentials are hallmark method of calculating the electronic and atomic structures of interfaces, and they also form a very natural alliance. They are so fundamental that their strength and weakness deserve special attention. In plane-waves pseudopotential method, the model system is constructed in 3D periodic supercell which allows Bloch's theorem to be applied to the electron wave-functions:

$$\Psi_{n,k}(r) = u_{n,k}(r)^{ikr} \qquad (2\text{-}19)$$

The function $u(r)$ has the periodicity of supercell. It can be of any suitable mathematical form and usually one chooses a series expansion in terms of a set of basis function. Plane-waves are used for this expansion, so that each single-electron wave-function Ψ_{nk} is written as follows.

$$\psi_{n,k}(r) = \sum u_{n,k}(G) e^{(i(k+G).r)} \qquad (2\text{-}20)$$

The μ_{nk} are the expansion coefficients. The wave-vectors G are such that the plane-waves are commensurate with the supercell. Both the number of G-vectors in the sum and the number of $k's$ considered should in principle be infinite. The exponential term is a plane-waves of wave-vector k which must be commensurate with the entire system (i.e. not just the periodically-replicated cell). For an infinite system there is an infinite number of k vectors, at each of which solutions for Ψ_{nk} exist. This simply reflects the fact that the number of electrons is infinite. However, a great simplification comes about when one realises that the change in Ψ_{nk} with k becomes negligible for k-points that are close together. This means that one may calculate at a finite number of k-points. We speak of this idea as k-point sampling. The set of vectors $\{G\}$, on the other hand, should in principle be infinite to obtain an exact representation of the wave-function. This is never necessary because summing over a finite number of G's will yield sufficient accuracy. Plane-waves basis set has many advantages such as; unbiased, completeness, single convergence criterion, mathematical simplicity and their derivatives are products in *k*-space and independence of atomic positions. On the other hand, they have disadvantages such that number of plane-waves needed being determined by the greatest curvature of the wave-function and empty space has the same quality of representation and cost a regions of interest. The advantages speak for themselves, for example the first three indicate that one can always ensure that the basis set is adequate for a calculation by increasing the number of plane-waves until the quantity of interest stops changing. In other words, the quality

of the basis set depends on a single parameter, usually expressed as the energy of free electron whose wave-function has the same wave-vector as the largest wave-vector in the plane-wave basis.

$$E_c = \frac{\hbar^2 (G+k)^2}{2m} \tag{2-21}$$

All plane-waves of 'energy' less than the cut-off energy E_c are used in the expansion. The mathematical simplicity of plane-waves means the method is easier to implement, crucially so for the calculation of ionic forces which adds little complexity or cost to the calculation. Equally important in this context is the origin-less nature of plane-waves. Their independence from atomic positions means that the forces do not depend on the basis set—there are no 'Pulay' or 'wave-function' forces [108]. Even more important, new developments are easiest in plane-wave codes. An idea to calculate a property is most rapidly realised in a plane-wave basis and even if other methods catch up in time, the plane-wave approach remains as the reference. From a computational viewpoint the first of the disadvantages appears to be very serious.

2.4.2. Pseudopotential approximation

The rapid oscillations of the wave-functions near to the nucleus, due to the very strong potential in the region and the orthogonality condition between different states, mean that a very large cut-off energy and hence basis set would be necessary. Fortunately, the study of physics and chemistry shows that the core electrons on different atoms are almost independent of the environment surrounding the atom and that only the valence electrons participate strongly in interactions between atoms. Thus, the core electron states may be assumed to be fixed and a pseudopotential may be constructed for each atomic species which takes into account the

effects of the nucleus and core electrons [109]. The pseudopotential approximation allows the electronic wave-functions to be expanded using a much smaller number of plane-wave basis states. It is well known that most physical properties of solids are dependent on the valence electrons to a much greater extent than on the core electrons. The pseudopotential approximation exploits this by removing the core electrons and replace them with strong ionic potential using a weaker pseudopotential that acts on a set of pseudo wave-functions rather than the true valence wave-functions. An ionic potential, valence wave function and corresponding pseudopotential and pseudo wave functions are illustrated in figure 2.1. The valence wave-functions oscillate rapidly in the region occupied by the core electrons due to the strong ionic potential in the region. These regions maintain the orthogonality between the core wave-functions and the valence wave-functions, which is required in the Pauli's exclusion principle [110].

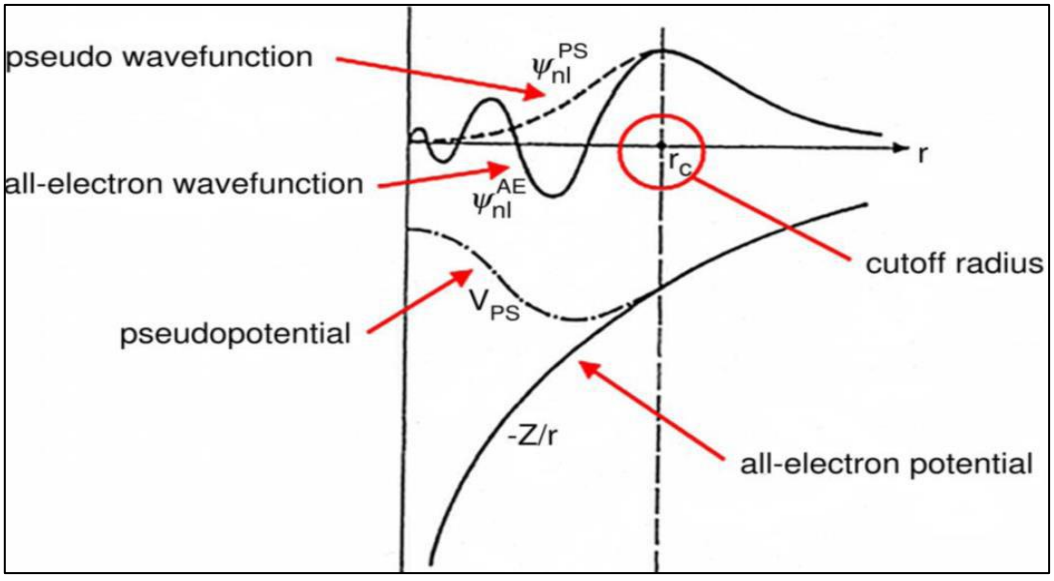

Figure 2-1. Schematic illustration of all-electron (solid) and pseudo-electron (dashed line) potentials and their corresponding wave function [111].

The pseudopotential is constructed in such a way that its scattering properties or phase shifts for the pseudo wave-functions are identical to the scattering properties of the ion and the core

electrons for the valence wave-functions, but in such a way that the pseudo wave-functions have no radial nodes in the core region. The phase shift produced by the ion core is different for each angular momentum component of the valence wave function and so the scattering from the pseudopotential must be angular momentum dependent. The most general form for pseudopotential is

$$V_{NL} = \sum_{lm} |lm\rangle V_l \langle lm| \tag{2-22}$$

Where $\langle lm|$ are the spherical harmonics and V_l is the pseudopotential for angular momentum (l). Acting on the electronic wave function with this operator decomposes the wave function into the spherical harmonics, each of which is the multiplied by the relevant pseudopotential (V_l). A pseudopotential that uses the same potential for all the angular momentum components of the wave function is called a local pseudopotential. Pseudopotential is a function only of the distance from the nucleus. It is possible to produce arbitrary, predetermined phase shifts for each angular momentum state with a local potential. However, there are limits to the amount that the phase shifts can be adjusted for the different angular momentum states while maintaining the crucial smoothness and weakness of the pseudopotential. Without a smooth, weak pseudopotential it becomes difficult to expand the wave-functions using a reasonable number of plane-waves basis states.

2.5. k-sampling

Electronic states are allowed only at a set of *k*-points determined by the boundary conditions that apply to the bulk solid. The density of allowed *k*-points is proportional to the volume of the solid. The infinite numbers of electrons in the solid are accounted for by an infinite number of *k*-points and only a finite number of electronic states are occupied at each *k*-point.

The Bloch theorem [112] changes the problem of calculating an infinite number of electronic wave-functions to one of calculating a finite number of *k*-points. The occupied states at each *k*-point contribute to the electronic potential in the bulk solid so that in principle an infinite number of calculations are needed to compute this potential. However, the electronic wave-functions at *k*-points that are very close are identical. Hence it is possible to represent the electronic wave-functions over a region of *k*-space by the wave-functions at the single k-point. In this case the electronic states at only a finite number of *k*-points are required to calculate the electronic potential and hence determine the total energy of the solid.

Methods have been devised for obtaining very accurate approximations to the electronic potential from a filled electronic band by calculating the electronic wave-functions at special sets of *k*-points. The two most common methods are those of Chadi and Cohen [113] and Monkhorst and Pack [114]. Using these methods, the electronic potential and the total energy of an insulator can be obtained by calculating the electronic states at a very small number of *k*-points. A denser set of *k*-points are required to calculate the electronic potential and the total energy of a metallic system in order to define the Fermi surface precisely.

However, the computational cost of performing a very dense sampling of *k*-space increase linearly with the number of *k*-points in the Brillouin zone (BZ). Density functional codes approximate these *k*-space integrals with a finite sampling of *k*-points. Special *k*-points schemes have been developed to use the fewest possible *k*-points for a given accuracy, thereby reducing the computational cost. The most commonly used scheme is that of Monkhorst and Pack [114].

2.6. Plane-wave pseudopotential code”

2.6.1. VASP code

Vienna *ab*-initio simulation package (VASP) is a package for performing *ab*-initio quantum-mechanical molecular dynamics (MD) using pseudopotentials and a plane-waves basis set. VASP is based on a finite-temperature local-density approximation approach (with the free energy as vibrational quantity) and an exact evaluation of the instantaneous electronic ground state at each MD-step using efficient matrix diagonalization schemes and efficient Pulay mixing [115]. These techniques avoid all problems occurring in the original Car-Parrinello method which is based on simultaneous integration of electronic and ionic equations of motion. The interaction between ions and electrons is described using ultrasoft Vanderbilt pseudopotentials (US-PP) or the projector augmented wave method (PAW) [116]. Both techniques allow a considerable reduction of the necessary number of plane-waves per atom for transition metals and first row elements. Forces and stresses can be easily calculated with VASP and used to relax atoms into their instantaneous ground state. The Projector-Augmented wave implemented in VASP reconstructs the full all-electron density and avoids the necessity of nonlinear core-corrections [117].

2.6.2. Phonon code

The computational programmes used to determine phonons are VASP, Wien2K, Phonon and etc. However, the phonon spectra can be studied within the direct method, which is implemented in the Phonon program written by Krzysztof Parlinski [118]. This method is based on the calculation of the interatomic forces in the supercell with the periodic boundary conditions. The Hellmann-Feynmann forces are obtained using one of the density functional theory codes like VASP, Wien2K or SIESTA. The direct method called Phonon code has been

used to calculate the phonon dispersion curves and phonon density of states in numerous crystals, multilayers, and surfaces. Phonon code is a software for calculating phonon dispersion curves, phonon density spectra of crystals, crystals with defects, surfaces and adsorbed atoms on surfaces from either a set of force constants or from a set of Hellmann-Feynman forces calculated within an ab initio program. Phonons play an important role in solids and determine the thermal properties of all kinds of materials. They also builds a crystal structure using one of the 230 crystallographic space groups to find the force constant from the Hellmann-Feynman forces, builds the dynamical matrix, diagonalise it and calculate the phonon dispersion relations and their intensities [119]. Phonon finds the polarization vectors and the irreducible representations (Gamma point) of phonon modes and calculates the total and partial phonon density of states. It plots the internal energy, free energy, entropy, heat capacity and tensor of mean square displacements (Debye-Waller factor). Phonon finds the dynamical structure factor for the coherent inelastic neutron scattering and the incoherent doubly differential scattering cross section.

2.7 Theoretical background of the calculated properties

2.7.1 Heats of formations

The standard enthalpy of formation or standard heat of formation of a compound is the change of enthalpy that accompanies the formation of 1 mole of a substance in its standard state from its constituent elements in their standard states (the most stable form of the element at 1 bar of pressure and the specified temperature, usually 298.15 K or 25 degrees Celsius). The heats of formation and associated entropies provide a fundamental understanding on stabilities and phase diagrams construction. The results of lattice parameters and heats of formation are

discussed in chapter 3. For this study, heats of formations were calculated using equation 2-23 as follows:

$$\Delta H_f\,(MCO_3) = [E_{tot} - (E_M + Ec + 3Eo)] \quad (2\text{-}23)$$

where E_{tot} is the calculated total energy of the compound, E_M is the calculated total energy of metal element, E_C is the calculated energy of carbon, E_O is the calculated energy of oxygen in the compound. The heats of formations for all the MCO_3 structures are calculated using VASP and will be discussed in chapter 3. The heats of formations will be used for predicting the stability trend of five structures used in this study.

2.7.2 Density of states

"The density of states (DOS) of a system describes the number of states per interval of energy at each energy level that are available to be occupied. DOS is a useful mathematical concept of allowing integration with respect to the electron energy to be used instead of the integration over the Brillouin zone. In other words, the density of states indicates how densely packed are quantum states in a particular system, unlike isolated systems like atoms or molecules in gas phase. A high DOS at a specific energy level means that there are many states available for occupation, while a DOS of zero means that no states can be occupied at that energy level. In general, a DOS is an average over the space and time domains occupied by the system. In addition, DOS is often used for quick visual analysis of the electronic structure as shown in Figure 2.2. Characteristics such as the width of the valence band, the energy gap in insulators, the number and intensity of the main features are helpful in qualitatively interpreting experimental spectroscopic data. DOS analysis can also help to understand the changes in electronic structure caused by for example, external pressure.

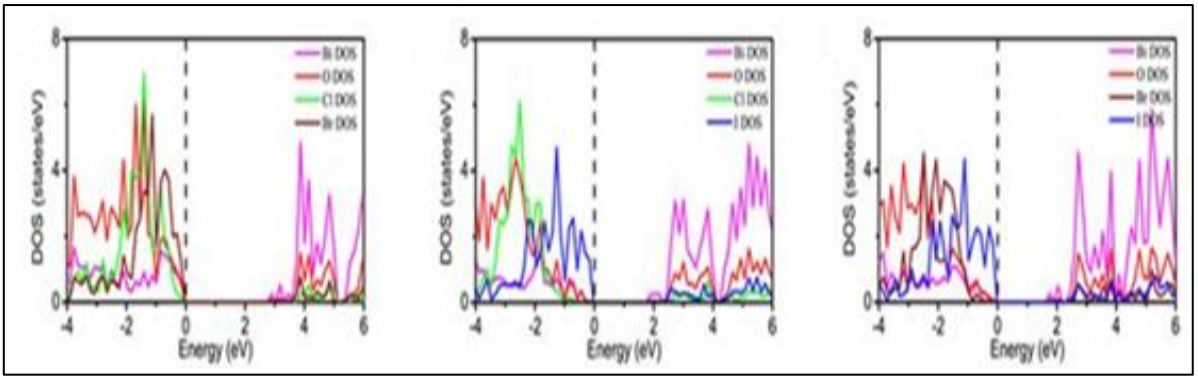

Figure 2-2. Schematic illustration of the density of states and the fermi level (dashed line) [120].

More accurate methods are based on linear or quadratic interpolations of band energies between the reference points in the Brillouin zone. The most popular and reliable technique, which is based on the tetrahedron interpolation, is unfortunately ill suited to the Monkhorst-Pack grid of special points. Therefore, VASP uses a simplified linear interpolation scheme. This method is based on the linear interpolation in parallelepipeds formed by the points of the Monkhorst-Pack set, followed by the histogram sampling of the resultant set of band energies.

The density of states behaviour at E_f (the dashed line shown in figure 2.2) is significant and can be used to correlate their stability. It is also known from literature that the DOS for structures of the same composition can be used to mimic the stability trend with respect to their behaviour at the E_f. The structure with the highest and lowest density of density at E_f is considered the least and most stable, respectively. Furthermore, we can determine whether our structures are metal, semi-conductors or insulators by measuring their band gaps respectively".

2.7.3 Phonon dispersion curves

The phonon dispersion curves are defined as the wave vector (k) dependence of the frequencies $\omega(k,j)$ of the normal modes for all branches and selected directions in the crystal. Phonon dispersion curves have an essential role in several physical properties of condensed matter physics. These include thermal conductivity, mechanical stability and electrical conductivity.

They indicate an excited state in the quantum mechanical quantization for the modes of vibrations of elastic structures of interacting particles. The behaviour of phonon dispersion branches reflects specific features of the crystal structure and the interatomic interactions and therefore gives the most comprehensive and detailed information about the dynamical properties of crystals.

In crystals were there are two or more types of atoms, two types of vibrations are displayed; acoustic and optical. Optical phonons arise from out of phase vibrations between neighbouring atoms within the unit cell, while the in phase vibrations give rise to acoustic phonons. The acoustic modes have zero frequencies at Γ (centre of the Brillouin zone) while optical modes have non-zero. The acoustic and optical split into longitudinal and transverse modes abbreviated as longitudinal acoustic (LA), transverse acoustic (TA), longitudinal optical (LO) and transverse optical (TO), also the out-of-plane acoustic (ZA) and out-of-plane optical (ZO) as shown in figure 2.1. A linear relationship between frequency and long wavelengths phonon wave-vector is displayed in acoustic mode. Negative vibrational frequencies (soft modes) indicate mechanical instability of the system, while positive vibrations show stability. Along with the Γ point (centre of the Brillouin zone) there are several points of high symmetry which are of significant interest. Table 2.2 lists and describes the critical k-points of high symmetry line in the first Brillouin zone for certain Bravais lattice of base centred cubic (BCC), face centred cubic (FCC), and hexagonal lattices [121].

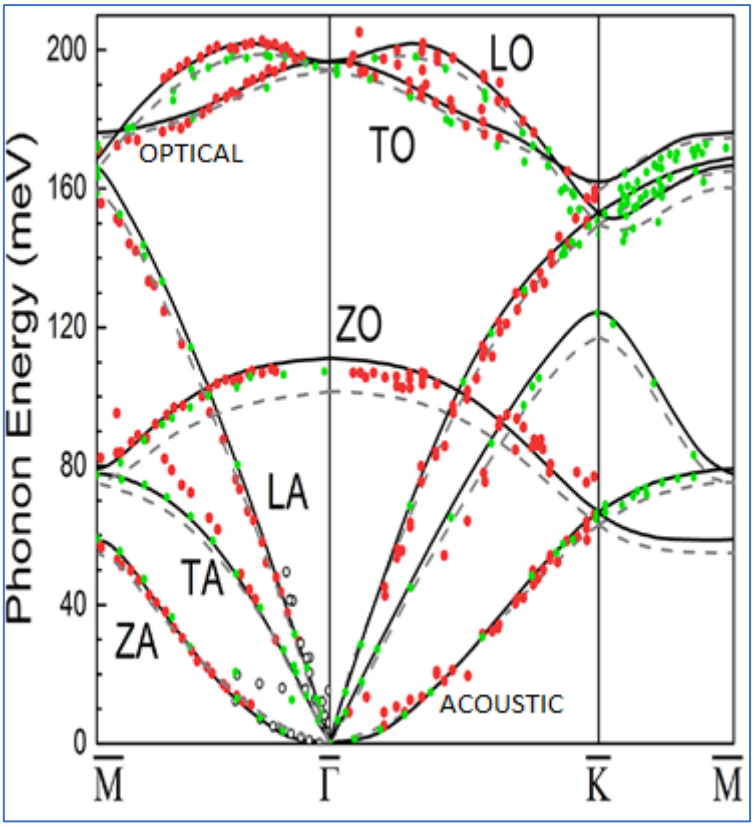

Figure 2-3. Illustration of the optic and acoustic phonon modes [122].

Table 2-2. Analysis of the critical k-points in the Brillouin zone.

Simple Cube	
Symbol	**Description**
$\Gamma(0,0,0)$	Centre of the Brillouin zone
$M(1/2,1/2,0)$	Centre of an edge
$R(1/2,1/2,1/2)$	Corner point
$X(0,1/2,0)$	Centre of a face
Body-centred cubic	
Symbol	**Description**
$H(-1/2,1/2,1/2)$	Corner point joining four edges
$P(1/4,1/4,1/4)$	Corner point joining three edges

N(0,1/2,0)	Centre of a face
Face-centred cubic	
Symbol	**Description**
K(3/8,3/4,3/8)	Middle of an edge joining two trigonal faces
L(1/2,1/2,1/2)	Centre of a trigonal face
U(1/4,5/8,5/8)	Middle of an edge joining a trigonal and a square face
W(1/4,3/4,1/2)	Corner point
X(0,1/2,1/2)	Centre of a square face
Hexagonal	
Symbol	**Description**
A(0,0,1/2)	Centre of a hexagonal face
K(2/3,1/3,1/2)	Middle of an edge joining two rectangular faces
H(1/2,0,0)	Corner point
L(1/2,0,1/2)	Middle of an edge joining a rectangular and a hexagonal face
M(1/2,0,0)	Centre of a rectangular face

2.7.4. Theory of elasticity

From the perspective of material physics, the elastic constantsC_{ij}, contains important information that can be obtained from ground-state total-energy calculations. A given crystal structure cannot exist in a stable or metastable phase unless its elastic constants obey certain relationships. The C_{ij} also determines the response of the crystal to external forces, as characterized by the bulk modulus, shear modulus, Young's modulus and Poisson's ratio and so play an important role in determining the strength of a material [123]. First-principles calculations that use periodic boundary conditions assume the existence of a single crystal, so

all elastic constants can be determined by direct computation. The calculated C_{ij} can then be used to check the experimental bulk and shear moduli, if available and to calibrate model calculations. In addition, the elastic constants can be used to check the phase stability of proposed compounds [124]. First-principles calculations can thus be used to predict the existence and properties of new materials.

2.7.5. Definition of elastic constants

To determine the elastic constants of a crystal, a deformation of the unit cell is created by changing the Bravais lattice vectors R = (a, b, c) of the undisturbed unit cell to R′ = (a', b', c') using a strain matrix e below;

$$R' = R.\begin{pmatrix} 1+e_{xx} & \frac{1}{2}e_{xy} & \frac{1}{2}e_{xz} \\ \frac{1}{2}e_{yx} & 1+e_{yy} & \frac{1}{2}e_{yz} \\ \frac{1}{2}e_{zx} & \frac{1}{2}e_{zy} & 1+e_{zz} \end{pmatrix}. \qquad (2\text{-}24)$$

The deformation leads to a change of the total energy of the crystal

$$U = \frac{E_{tot} - E_0}{V_0} = \frac{1}{2}\sum_{i=1}^{6}\sum_{j=1}^{6} C_{ij} e_i e_j \qquad (2\text{-}25)$$

where E_0 is the total energy of the unstrained lattice, V_0 is the volume of the undistorted cell and C_{ij} are the elements of the elastic constant matrix with a notation that follows standard convention. Both i and j run from 1…6 in the sequence {xx, yy, zz, yz, xz, xy}. The tensor of elasticity has 36 elements, the elastic constants, but maximally 21 of these are independent.

2.7.6. Calculation of elastic constants

The simplest case by far is the cubic system where there are only three independent constants,C_{11}, C_{12} and C_{44}. We use this case to illustrate the manner in which the stiffness matrix elements may be determined from strain fields of the form (2-22). If the applied strain is $e_{xx} = e$ with all other e_i equal to zero, the energy change is $U = \frac{C_{44}e^2}{2}$. This allows a unique determination of C_{11}. If $e_{yz} = e_{zy} = \frac{e}{2}$, with all other strain components zero, then $U = \frac{C_{44}e^2}{2}$ and we have an independent determination of C_{44}. The bulk modulus B, is the response to a uniform compression so applying the strain field $e_{xx} = e_{yy} = e_{zz} = e$ allows the computation of B via the relation $U = \frac{Be^2}{2}$. Similarly, the shear modulus can be calculated by using the strain field $e_{zz} = e_{xx} = e_{yy} = -\frac{e}{2}$, whereupon $U = \frac{3c\prime e^2}{2}$. Finally, the off-diagonal stiffness matrix element C_{12} can be calculated using one or other of the relations as shown below.

$$B = \frac{1}{2}(C_{11} + 2C_{12}) \tag{2-26}$$

$$C' = \frac{1}{2}(C_{11} - C_{12}) \tag{2-27}$$

Using both of these relations provides a useful independent check on the accuracy of the computation. A symmetry-general formulation of the calculation of elastic constants from total energy calculations is given by Le Page and Saxe [125].

2.7.7 Elastic constant stability conditions

The accurate calculation of elasticity is essential for gaining an insight into the mechanical stability and elastic properties of solids. For the cubic, tetragonal, orthorhombic and trigonal crystals, there are three (C_{11}, C_{12}, C_{44}), six (C_{11}, C_{12}, C_{13}, C_{33}, C_{44}, C_{66}) thirteen (C_{11}, C_{22}, C_{33},

C_{12}, C_{13}, C_{23}, C_{44}, C_{55}, C_{66}, C_{15}, C_{25}, C_{35}, C_{46}) and six/seven (C_{11}, C_{33}, C_{44}, C_{12}, C_{13}, C_{14}) or (C_{11}, C_{33}, C_{44}, C_{12}, C_{13}, C_{14}, C_{66}) independent elastic constants. Applying two kinds of strains (ε_1 and ε_4) can give stresses relating to these elastic coefficients, yielding an efficient method for obtaining elastic constants for the cubic system. This method has been successfully used to study the elastic properties of a range of materials including metallic systems [123]. The mechanical stability criteria of cubic systems as outlined elsewhere [126] are shown below;

$$C_{11} - C_{12} > 0;\ C_{11} + 2C_{12} > 0;\ C_{44} > 0 \tag{2-28}$$

where C_{11}, C_{12} and C_{44} are the only three independent elastic constants. Based on three independent single crystal elastic constants of a cubic crystal, C_{11}, C_{12}, C_{44}, the elastic moduli are determined using the following expressions:

$$B = \left(\frac{C_{11} + 2C_{12}}{3}\right),\ C' = \frac{C_{11} - C_{12}}{2},\ A = \frac{(2C_{44} + C_{12})}{C_{11}},\ \tag{2-29}$$

where B is the bulk modulus, C' tetragonal shear modulus and anisotropic factor A. It is acknowledged that the bulk modulus B is a measure of resistance to volume changed by applied pressure, whereas the elastic anisotropy A has an important implication in engineering science since it is highly correlated with the possibility of inducing micro-cracks in materials [126]. If the material is completely isotropic, the value of A will be 1, while values smaller or larger than 1 measure the degree of elastic anisotropy. The positive C' indicates the mechanical stability of the crystal, while the negative C' indicate the mechanical instability.

2.8. Universal Cluster Expansion

Cluster expansion (CE) is a power series expansion of the partition function which was proposed by Mayer and is often applied in models of material calculations [78]. Cluster expansion allows the extraction of atom-atom interactions from a set of first principles and

small unit cell calculations. To model real materials in CE requires accurate energy values for systems with millions of atoms and also require quick sampling of millions for such systems in ensembles to acquire good statistics. Cluster expansion method is an effective tool to connect quantum mechanics with large scale atomistic simulation [79].

Modern DFT methods are able to calculate material properties with reasonable to high precision (depending on the quality of the approximations to the exchange and correlation effects). Standard DFT applications are, however restricted to unit cells of a few hundreds of atoms. If one wants to model an alloy with varying atomic concentrations and crystal structures, a huge number of very large supercells would be needed. Such a procedure is of course, not feasible. A successful strategy to overcome this limitation is offered by the cluster expansion (CE) [80] in particular when combined with Monte Carlo simulations.

2.8.1 Basic Principles of Cluster Expansion

From an optimised cluster expansion, a set of effective cluster interactions can be extracted and used in large-scale Monte Carlo simulations to explore order-disorder phenomena and phase segregation processes as a function of temperature.

On a basic lattice various atoms, for example of type A and B, are distributed to define structure σ, a periodic configuration of A and B atoms. This configuration is described by the pseudo spin operator σq =$\pm$1, which has the value +1 if an atom A sits on site q or -1 if that atom is B.

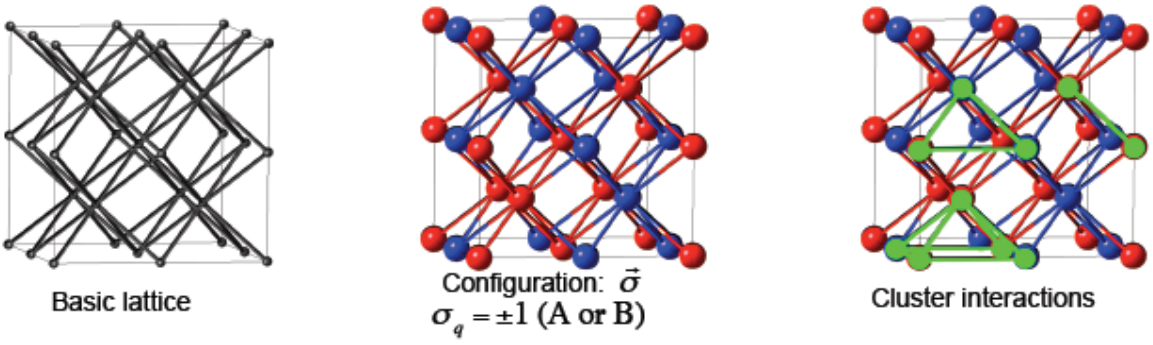

The energy (σ) associated with structure σ can be described by an expansion of cluster interactions and their respective interaction energies J by means of equation

$$E(\vec{\sigma}) = J_0 + J_1 \sum_i \sigma_i + \sum_{i>j} J_{ij}\sigma_i\sigma_j + \sum_{i>j>k} J_{ijk}\sigma_i\sigma_j\sigma_k + \cdots \tag{4-1}$$

In equation (4-1), J_0 describes a constant configuration independent contribution. The second term is concentration dependent and is the sum over all N sites of structure σ with onsite energy J_1 times the pseudo spin operator σ at each site i. Further terms describe the cluster interactions between multiple sites, for example two-body interactions J_{ij} or three-body interaction J_{ijk}. They contain spin products $\sigma_i\sigma_j \ldots$ over all f vertices of a cluster times its effective cluster interaction energy $J_{ij\ldots}$ summed up over all the possible ways that the cluster can be placed on the lattice of structure σ. In other words, the energy (σ) of structure is broken down into clusters with their associated effective interaction energies. The core issue of cluster expansion is to identify a universal set of interactions J best-suited to describe a given model. To accomplish this, it is useful to reformulate above equation into the more compact form.

$$E(\vec{\sigma}) = \sum_{C \in \vec{C}} J_C \, \Pi_C(\vec{\sigma}) \tag{4-2}$$

The cluster expansion equation sums up the product of cluster C's interaction energy J_C with its correlation function,

$$\Pi_C(\vec{\sigma}) = N^{-1}\sum_{i=1}^{N}\sum_{k\in C}\prod_{v\epsilon\vec{f}}\sigma_v \tag{4-3}$$

The sum over all the possible ways that a cluster C with $\vec{f}$ vertices can be placed on the N sites of the structure. In the correlation function the spin product σ_1 … goes over all f vertices of the cluster. Only symmetry in-equivalent clusters are now considered and clusters included in an expansion can be collected by the vector $C = \{C_1,\ldots, C_n\}$.

2.8.2. UNCLE Code

All the cluster expansion calculations for the study were performed by the program named the Universal Cluster Expansion (UNCLE) which was developed by the group of S. Muller [127]. The code is applicable to as many systems as possible, it requires little user input and it also contain efficient tools for the use of ECI's such as kinetic and thermodynamic Monte Carlo simulation. UNCLE code is also able to perform a complete cluster expansion fit using a genetic algorithm to predict the ground states of systems containing up to three and more elements. For deriving results for temperatures T=0, Monte Carlo simulations are implemented. The working scheme used by the cluster expansion for finding input structure is displayed in Figure 2-4. The crucial task of a converged CE is to guarantee that chosen interactive energy and figures are not biased by the training set. To avoid wrong interpretation of the whole system by choosing wrong input, UNCLE uses the chosen figure set to fit the energy of other structures. New structures can now be designed and if they lie energetically below the existing ground state line they are recalculated by DFT, providing a new set of input structures.

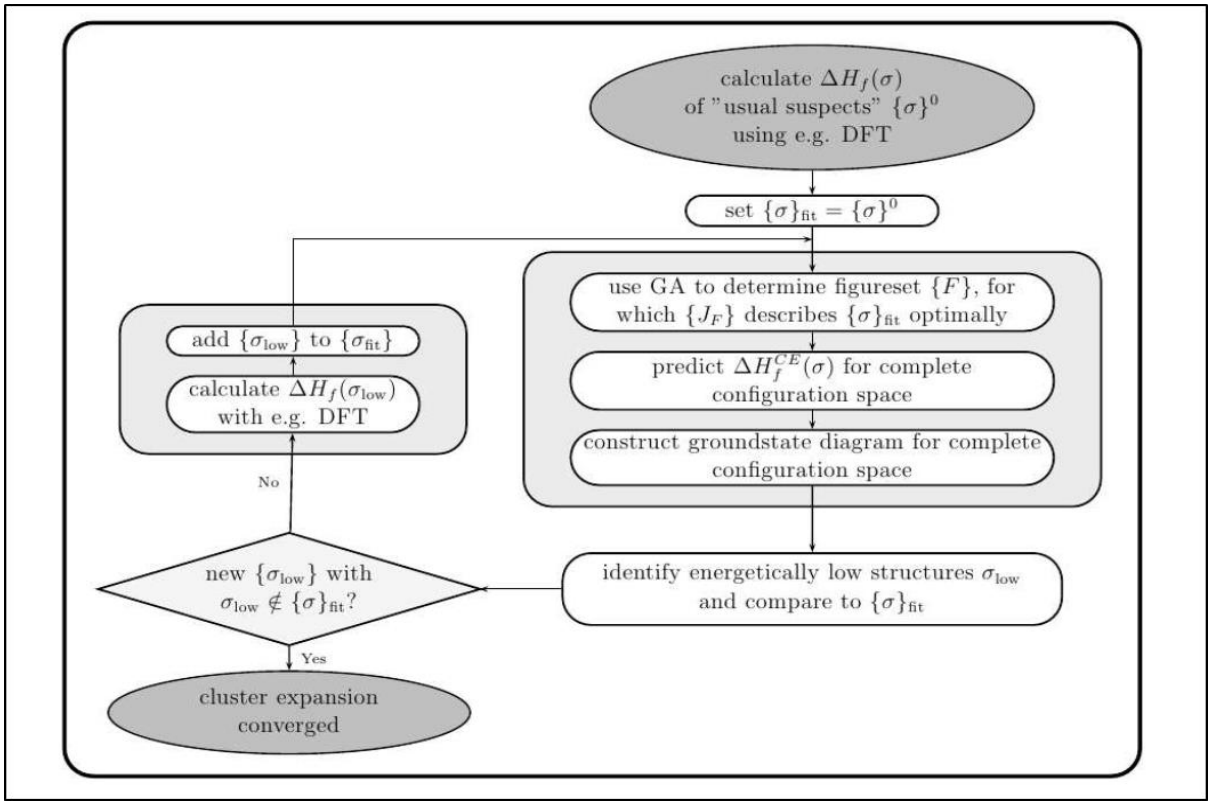

Figure 2-4. Illustration of the self-consistent working plan used by UNCLE to choose the input structures of the cluster expansion [82].

2.8.3. Genetic Algorithm

A minimization using genetic algorithm was first used for the CE by Hart et al. [83]. In this approach the figure list is represented as a binary string. A figure used is marked by the value 1, otherwise the value is 0. Furthermore, the interaction energies are also represented as a binary string. The combination of both binary strings, including figures used and their interaction energies, is now the genetic 'DNA' of a solution, who's fitness is described by the CVS. A higher CVS compared to other solutions means, that this solution has a lower fitness. Now, a 'population' of n_{pop} different solutions is created, in which the fitness of every individual solution is calculated. Of those n_{pop} individuals only the fittest n_{fit} ($0 < n_{fit} < n_{pop}$) individuals are selected to survive to the next iteration process. The other n_{pop}-n_{fit} solutions are replaced by 'descendants' of the surviving fittest 'parent' solutions. Their 'DNA' is created by two different processes as shown below:

• In crossover, the ‘DNA’ of the ‘offspring’ is created by mixing the ‘DNA’ of two randomly selected ‘parent’ solution. Thereby the ‘DNA’ of one ‘parent’ solution is used up to the crossover point. After that point the ‘DNA’ of the second ‘parent’ is used.

• In mutation, a random binary bit of the ‘DNA’ string is flipped from one state to the other, i.e. 1⇒0 or 0⇒1.

Note that one may replace all surviving ‘parent’ solutions with the ‘children’, for as long as only the fittest ‘parent’ solutions are used to create them.

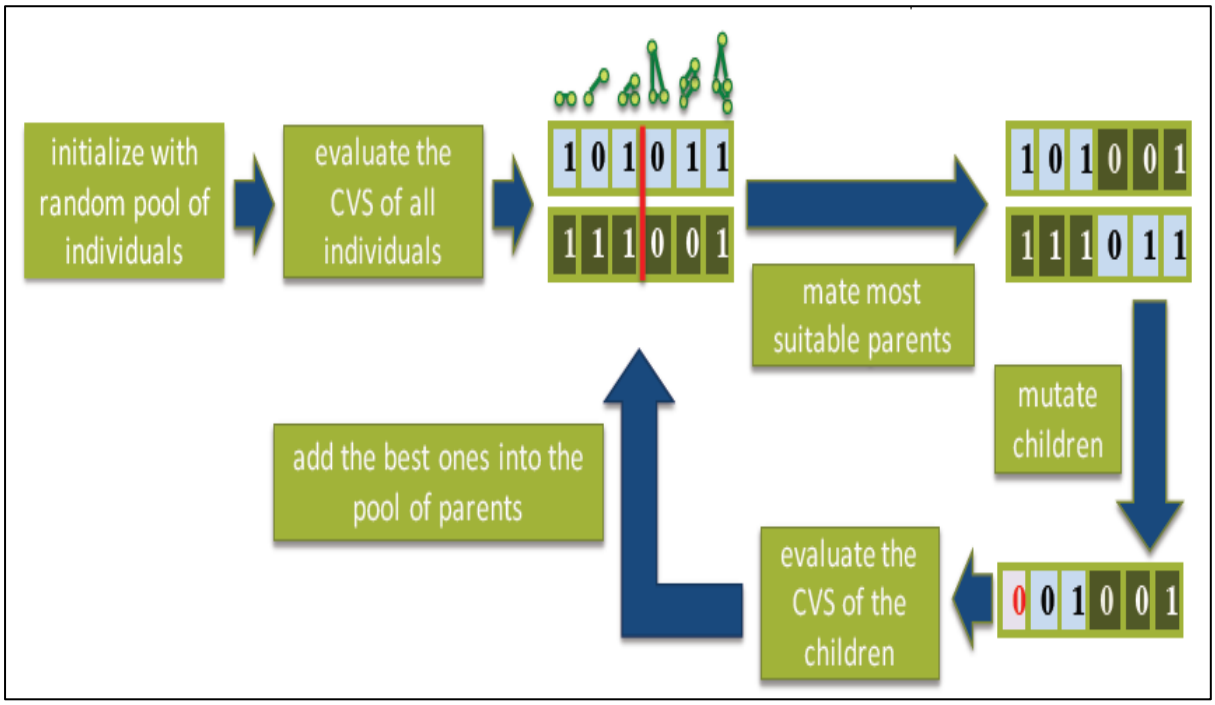

Figure 2-5. Illustration of the genetic algorithms [128].

2.9. Synthesis methods for NMC cathode material

The synthesis process of battery cathode has evolved over the past two decades and several methods such as solid state, sol gel, co-precipitation, spray pyrolysis, hydrothermal, solvothermal and combustion have been explored both at academia and industrial [131]. Off all the methods available to synthesize NMC’s, in this study we use co-precipitation method to synthesize our NMC’s. The co-precipitation method is a widely used process in different

applications such as water treatment, pharmaceutical, metal mining, and catalyst manufacturing [132]. Co-precipitation has attracted interest in synthesizing NMC's due to its simplicity, improved particle morphology control, homogeneous mixing at the atomic scale, and facile scalability [133, 134]. Co-precipitation is used to synthesize battery active materials in two steps: transition metal co-precipitation and sintering. The first stage entails mixing transition metals in the proper proportions to make an ionic solution, then co-precipitating these metals in a controlled environment by altering pH to produce uniform particles known as precursors. A chelating agent is typically utilized throughout the precipitation process to achieve single-phase co-precipitation. The obtained precursors are washed with deionized (DI) water to eliminate impurities, then dried at room temperature or higher to remove residual water and/or other solvents used to clean the co-precipitates.

The co-precipitate can be ground before being combined with a lithium source, such as lithium hydroxide (LiOH) or lithium carbonate (Li_2CO_3). One of the primary advantages of adopting the co-precipitation approach is achieving the desired phase and crystallinity at relatively mild sintering temperature and holding time due to the homogenous mixing of transition metals at the atomic level [135, 136]. Although the size of primary particles and surface roughness of secondary particles are frequently affected by sintering, the comparatively moderate sintering conditions are useful in retaining the morphology and size of secondary precursor particles [137, 138]. The morphology and composition of the co-precipitate can be significantly influenced by various controllable parameters during co-precipitation processes such as pH, precipitation temperature and atmosphere, sources of transition metals and their concentration, use of chelating agents and their concentration, rate of reactant feed, stirring rate and mixing method, drying temperature, and the use of any other additives [139, 140]. In the literature, the synthesis of battery cathode material using the co-precipitation process is frequently

accomplished in batches, however continuous reactor-based manufacturing is also reported for mass-scale production [141]. Based on the acquired co-precipitation, the co-precipitation method is further classified into three types: hydroxide co-precipitation, carbonate co-precipitation, and oxalate co-precipitation. Hence, this study use the carbonate co-precipitation method to synthesize our NMC's.

2.10. Carbonate Co-precipitation

The carbonate co-precipitation process allows for easier control of the facile morphology and is regarded more ecologically friendly. The preparation of the precursor and sintering is identical to the hydroxide approach; the only difference is the source of transitional metal in the carbonate method, which is often a metal carbonate salt. One of the key advantages of using carbonate co-precipitation is that the majority of the transition metal cations, including manganese used for $LiNi_xMn_yCo_{1-x-y}O_2$ or other cathode materials for LIBs, remains in the divalent oxidation state by the fixation of CO_3^{2-} anion groups even in the presence of air or oxygen at all operating pH ranges [142]. As a result, there is no need to complete the precipitation process under an inert atmosphere to ensure high-quality goods [143]. Furthermore, the solution conditions for carbonate co-precipitation are rather neutral in terms of pH, making it easier to work with.

2.11. Continuous stirred tank reactor (CSTR)

A CSTR is an isothermal, constant-pressure flow reactor that mixes completely at steady state to ensure that the reactor's composition is consistent throughout. Four feedthroughs on the reactor lid enable the entrance of nitrogen gas, a chelating agent, a pH-controlling agent and a transition metal. While the chelating agent and transition metal inlets are at the bottom of the fluid between the lower and higher stirring blades, the nitrogen gas and pH control agent inlets

are located above the solution. A water bath jacket is also included in the reactor to regulate the reaction's temperature. One or more fluid reagents are added to a tank reactor in a CSTR, and the tank reactor is normally agitated by an impeller to guarantee correct reagent mixing while the reactor overflow is withdrawn. The space time or the amount of time needed to process one reactor volume of fluid is calculated by dividing the tank's volume by its average volumetric flow rate. The estimated % completion of the reaction can be computed using chemical kinetics. The tank will overflow or become empty if the mass flow rate in and out are not equal in steady state (transient state). The model equation must be obtained from the differential mass and energy balances when the reactor is in a transient condition.

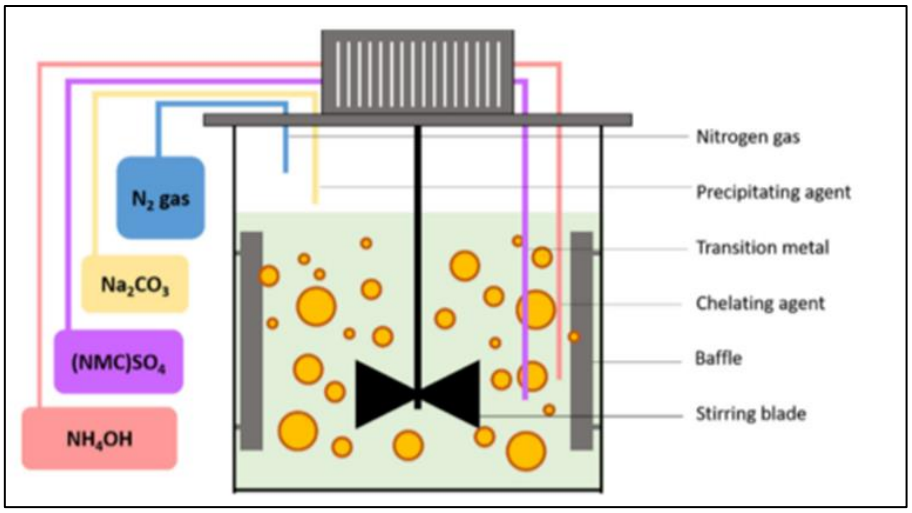

Figure 2-6. A schematic of the reactor configuration and inlet tubes [129].

2.12. Tap density measurement

Tap density tester as shown in Fig.2.7 was used to determine the tap density of our samples. Depending on the material's density, the sample is placed into a volumetric cylinder. A level surface is created by freely pouring the powder sample into the glass cylinder before inserting it into the tapping device. Once the powder has reached a steady condition, the sample is tapped. For this study, the powder sample was tapped for 1500 times, and the resulting volumes V_1 and V_2 were read to the nearest graded unit. V_2 is the tapped volume if the difference

between V_1 and V_2 is less than 2ml. Applying the formula$\frac{\Delta m}{V_2}$, where V_2 represent the final tapped volume, one can determine the tapped density (g/mL).

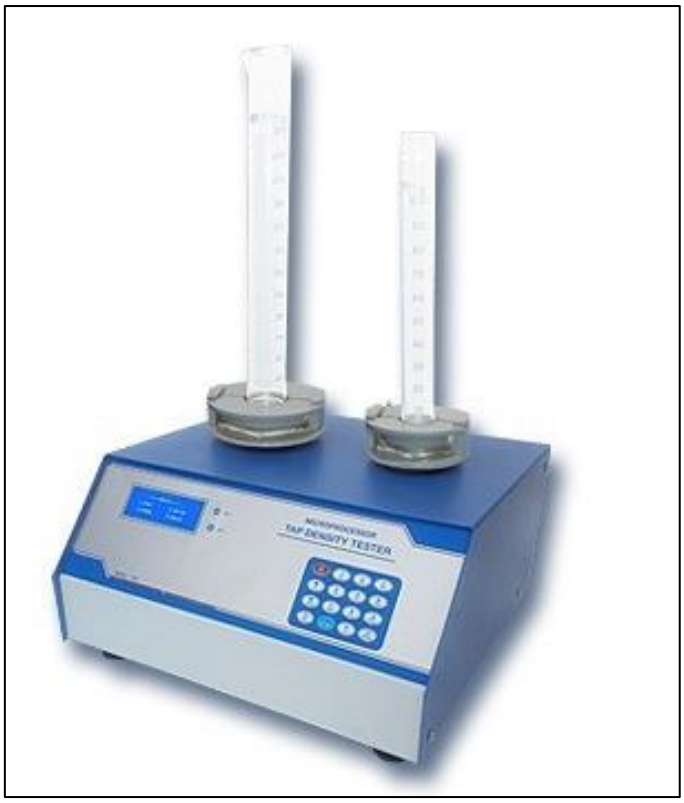

Figure 2-7. Tap density tester

2.13. Scanning Electron Microscope (SEM)

The SEM is a type of microscope that creates images using electrons as opposed to light. Since the SEM has a significantly better resolution, small specimens may be enlarged much more effectively. Special sample preparations are required due to the vacuum environment and electron-based image formation used by the SEM. The samples must be completely dry because any remaining water would vaporize in the vacuum. Since they are all electrically conductive, all metals can be employed right away.

The sample is positioned in a tiny compartment that is vacuum sealed. One electric field and argon gas remove an electron from argon, making the atoms positively charged. The SEM is a device that forms a picture using electrons rather than light, resulting in a significantly magnified image. An electron gun at the top of the microscope produces an electron beam. The microscope is maintained in a vacuum and the electron beam travels through it in a vertical path. The beam is focused downward toward the sample as it passes via electromagnetic fields and lenses. Electrons and X-rays are ejected from the sample after the beam strikes it.

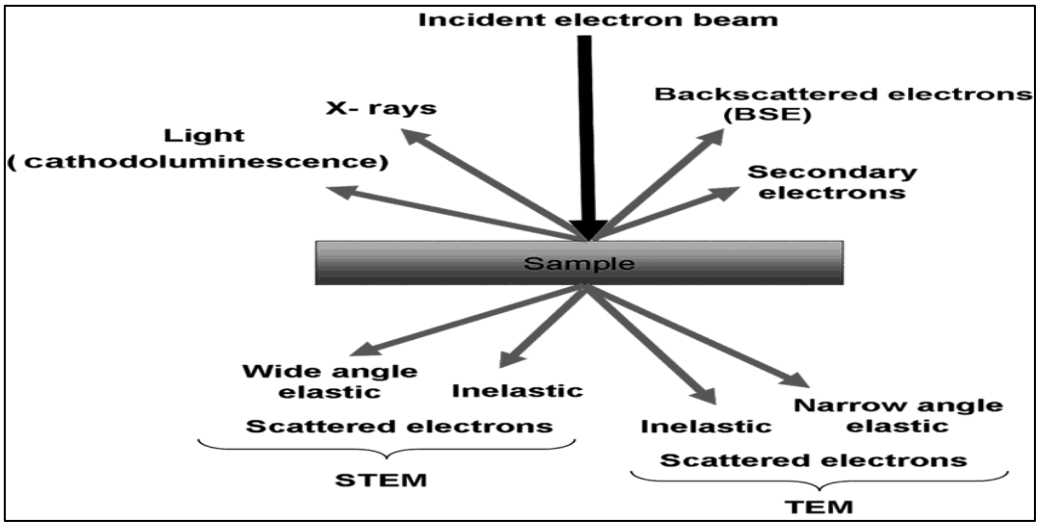

Figure 2-8. Schematic Scanning Electron Microscope (SEM).

2.14. X-Ray Diffraction (XRD)

The three fundamental components of an X-ray diffractometer are an X-ray tube, a sample holder, and an X-ray detector. In a cathode ray tube, X-rays are produced by burning a filament to produce electrons, accelerating the electrons with a voltage toward a target, and then hitting the target material with the accelerated electrons. Characteristic X-ray spectra are created when electrons have enough energy to knock off the target material's inner shell electrons.

As the sample and detector rotate through their respective angles, the amount of diffracted X-rays is continually measured. When the mineral has lattice planes with the proper d-spacing to diffract X-rays at that value of, the intensity peaks. Higher values of result in more separation. Usually, these merged peaks are regarded as a single peak. The centre of the peak at 80% peak height is often used to determine the 2 position of the diffraction peak. When the circumstances are in accordance with Bragg's Law (n = 2d sin), the interaction of the incident rays with the sample results in constructive interference (and a diffracted ray). This law establishes a connection between the lattice spacing and diffraction angle in a crystalline sample and the wavelength of electromagnetic radiation.

2.15. Raman Spectrum

Raman analysis refers to a spectroscopic technique used to study vibrational, rotational, and other low-frequency modes in a system. It involves shining a monochromatic light, often from a laser, onto a sample and analysing the scattered light. The scattering pattern provides information about the molecular vibrations and rotational energy levels within the sample. Raman spectroscopy is based on the Raman Effect, discovered by Sir C.V. Raman in 1928. When light interacts with a molecule, most of it scatters unchanged (Rayleigh scattering), but a small fraction interacts with the molecule's vibrational and rotational modes, causing a shift in energy. This energy shift, called the Raman scattering, is unique to the molecular structure of the sample, allowing for identification and characterization of substances.

2.16. Materials Synthesis

The precursor carbonate powders were synthesized using the co-precipitation method in a 4L continuous stirred tank reactor (CSTR) equipped with water-bath jacket for controlling temperature of the reaction. Co-precipitation method has gained interest in the last 10-15 years

due to its simplicity, better particle morphology control and the homogeneous mixing at the atomic scale. For the co-precipitation process, the desired transition metal sulphates (MSO_4, M= Ni, Mn, Co) were dissolved in deionized water in a stoichiometric ratio, then pumped into the reactor at a fixed rate. An aqueous solution of $NiSO_4$, $MnSO_4$ and $CoSO_4$ was prepared with a total concentration of 2M. Sodium carbonate (Na_2CO_3) solution was used as pH control or precipitant while ammonium hydroxide was used as a chelating agent. The reactor was maintained at a constant pH through the addition of ammonium hydroxide (NH_4OH). Constant concentration of ammonia was maintained within the chemical reactor which acts as a chelating agent that prevents impurity phases. Nitrogen gas was continuously bubbled into the reactor to remove the dissolved oxygen as it may cause unwanted oxidation which can form transition metal oxides or oxy-hydroxides. The reaction was maintained at 50 °C with continuous stirring of 1000 rpm under N_2 to ensure good mixing of the reactants. The resultant precursor was filtered to remove impurities and then it was dried in an oven at 80 °C for ~24 hours. Dried precursor powders and the stoichiometric amount of Li_2CO_3 were mixed exhaustively. The mixed powder was calcined at 1000 °C for 8h to obtain cathode active materials.

2.17. Synchrotron beam

The synchrotron beam of the Diamond light source (B18) was used to determine the X-ray absorption spectroscopy (XAS) which is useful in understanding the material's properties, such as oxidation states and bond distances. In our case we had pristine and fluorinated NMC samples which were weighed to the desired amount and mixed with polyvinylidene (PVD) as the binder to improve the pellet's mechanical strength then used mortar and pestle to soften the powder sample. We further placed the mixed samples into the pellet press which uses a hydraulic press to apply pressure and form the pellet. The pressure applied typically ranges from 100 to 500 MPa, depending on the material and desired density of the pellet. We then

used a foil to place pellets of various samples and sealed the foil using vacuum sealer for a more secure and airtight seal. The presentation of our samples in a sealed foil is shown in Figure 2-9. Moreover, the synchrotron beam as shown in Figure 2-10 was then used overnight whereby the beam passes through a sample, and the transmitted radiation is measured to study the material's properties. The sample interacts with the beam in several ways, such as absorbing, scattering or diffracting the light and the transmitted beam is then collected by detectors positioned on the other side of the sample. These detectors measure the intensity and other characteristics of the transmitted light, such as its wavelength, polarization or phase.

In synchrotron-based X-ray Absorption Spectroscopy (XAS) experiments, the absorption data can be collected in two main modes named the transmission mode and fluorescence mode as shown in Figure 2-11. In transmission mode, light (or another type of radiation, such as electrons) passes through a sample, and the transmitted portion is detected on the other side. This mode is used to analyze the internal structure or composition of the sample based on how much light is absorbed or how it is altered during transmission. With regard to the sample requirements for this mode, it is typically for thin samples with high concentrations. On the other hand, in fluorescence mode, light of a specific wavelength is used to excite the sample causing it to emit light (fluorescence) at a different wavelength. The emitted light is detected and used to form an image or gather data. This mode is based on the principle that certain molecules (fluorophores) absorb energy and then re-emit it as light at a longer wavelength. For our study, transmission mode was considered since our samples were in powder form (thin) with high concentrations. Furthermore, results were collected for further analysis using software's such as Athena and Artemmis [145].

Figure 2-9. Different types of samples in a sealed foil on a rack ready for the beam.

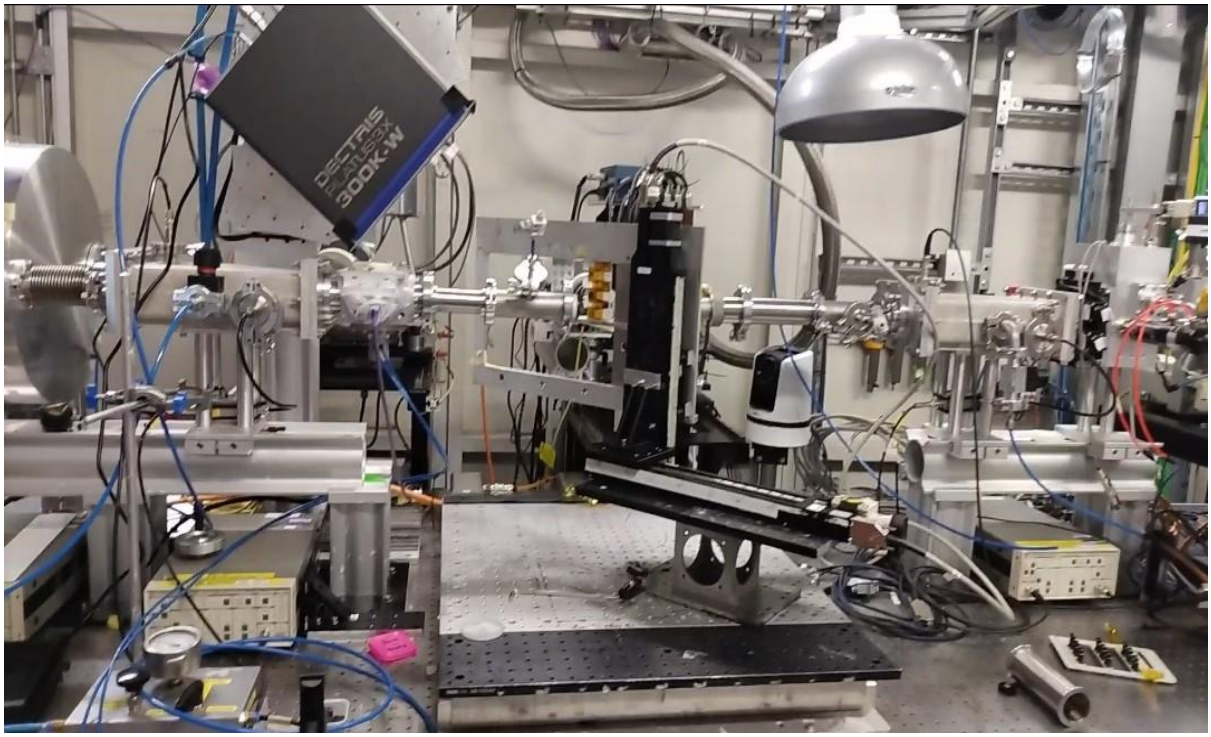

Figure 2-10. The synchrotron beam of the Diamond light source.

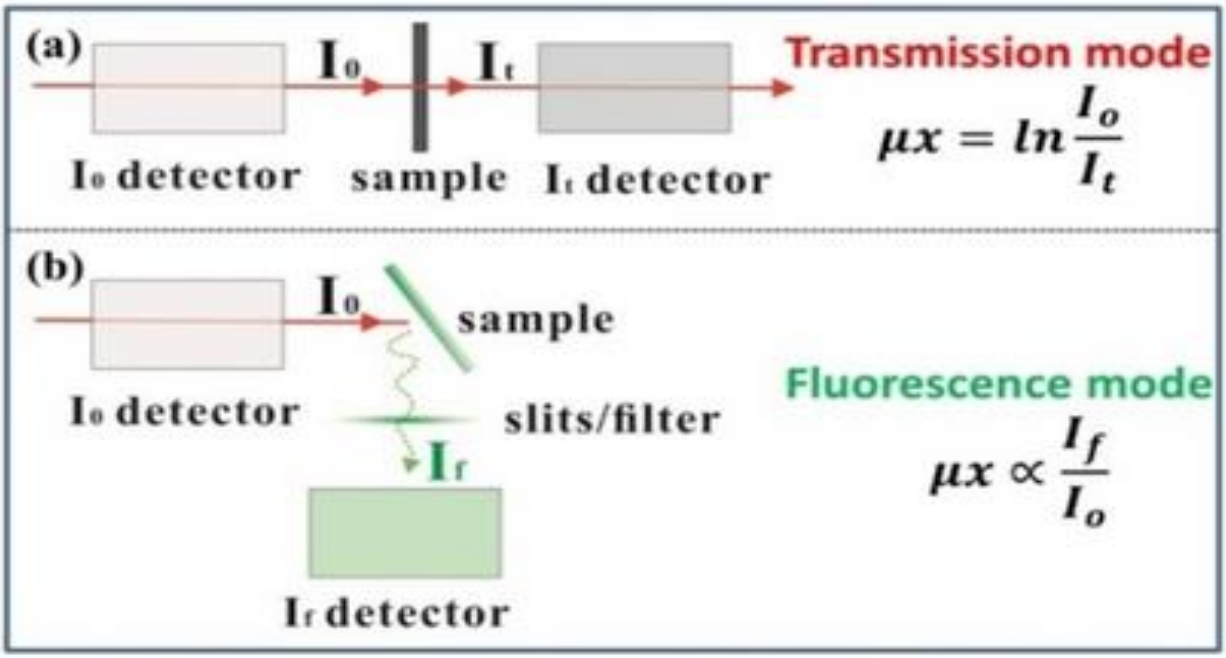

Figure 2-11. The schematic representation of the of a typical XAFS experimental setup, where in transmission mode, I_0 and I_T are measured using two ionization chambers, while in fluorescence mode, a fluorescence detector needs to be used [146].

Chapter 3
Computational Results

In this chapter we discuss the *ab initio* first principles results for manganese rich pure and doped structures named $Ni_{0.3}Mn_{0.5}Co_2CO_3$, $Ni_{0.3}Mn_{0.5}Co_2O_2$, F-doped $Ni_{0.3}Mn_{0.5}Co_2CO_3$, F-doped $Ni_{0.3}Mn_{0.5}Co_2O_2$ Ti-doped $Ni_{0.3}Mn_{0.5}Co_2CO_3$, Ti-doped $Ni_{0.3}Mn_{0.5}Co_2O_2$, Nb-doped $Ni_{0.3}Mn_{0.5}Co_2CO_3$, Nb-doped $Ni_{0.3}Mn_{0.5}Co_2O_2$, Cr-doped $Ni_{0.3}Mn_{0.5}Co_2CO_3$ and Cr-doped $Ni_{0.3}Mn_{0.5}Co_2O_2$ respectively. We particularly discuss their equilibrium lattice constants, heats of formations, band structures (BS), density of states (DOS), elastic properties and phonon dispersion curves. The calculations were performed using DFT approach as implemented in the Vienna Ab initio simulation Package (VASP) code [130]. The projector augmented wave (PAW) [131, 132] potential sets were employed with the exchange and correlation functional approximated in the spin-polarised localised density approximation.

3.1. Energetic Properties

The optimised crystal structures for $Ni_{0.3}Mn_{0.5}Co_2CO_3$ and $Ni_{0.3}Mn_{0.5}Co_2O_2$ are shown in Fig. 3.1 (a, b) and the crystallographic information is provided in Table 3.1-3.3. Table 3.1-3.3, presents the calculated lattice parameters, density and heats of formations for $Ni_{0.3}Mn_{0.5}Co_2CO_3$, $Ni_{0.3}Mn_{0.5}Co_2O_2$, F-doped $Ni_{0.3}Mn_{0.5}Co_2CO_3$, F-doped $Ni_{0.3}Mn_{0.5}Co_2O_2$, Ti-doped $Ni_{0.3}Mn_{0.5}Co_2CO_3$, Ti-doped $Ni_{0.3}Mn_{0.5}Co_2O_2$, Nb-doped $Ni_{0.3}Mn_{0.5}Co_2CO_3$, Nb-doped $Ni_{0.3}Mn_{0.5}Co_2O_2$, Cr-doped $Ni_{0.3}Mn_{0.5}Co_2CO_3$ and Cr-doped $Ni_{0.3}Mn_{0.5}Co_2O_2$. The lattice parameters were attained by fully optimising the structures whereby all the atom positions were relaxed, cell volume was allowed to change and the cell shape was also allowed to change. The Hubbard correction (U) in the rotationally invariant form by Liechtenstein and Zaanen, necessary to treat strongly correlated transition 3d metals was employed, whereby U = 4.5 eV and J = 1 eV were found to correctly predict the lattice constants for this study. From

our LDA+U lattice parameters shown in Table 3.1, we note that lattice parameters for $Ni_{0.3}Mn_{0.5}Co_2O_2$ are less than lattice parameters for $Ni_{0.3}Mn_{0.5}Co_2CO_3$ which indicate reduction of the structure. The density for $Ni_{0.3}Mn_{0.5}Co_2CO_3$ is greater than the density for $Ni_{0.3}Mn_{0.5}Co_2O_2$ which suggests that $Ni_{0.3}Mn_{0.5}Co_2CO_3$ has greater resistance compressibility as compared to $Ni_{0.3}Mn_{0.5}Co_2O_2$. We further went on and doped both the systems with fluorine, titanium, niobium and chromium to compare their behaviours. From our results we detect that doping $Ni_{0.3}Mn_{0.5}Co_2CO_3$ with fluorine, titanium and chromium reduces the density of our material which reduces our material's resistance while doping it with niobium increases its density which increases its resistance. We also noticed that doping $Ni_{0.3}Mn_{0.5}Co_2O_2$ with titanium and chromium decreases the density of our material while doping with fluorine and niobium increases its density.

In order to determine the thermodynamic stability of our materials, we have calculated their heats of formations using the formula below;

$$\Delta H_f(kJ/mol) = \frac{1}{N}[E_{tot} - (E_M + E_C + 3E_O)] \quad (3\text{-}1)$$

Where N is the number of atoms, E_{tot} is the total energy of the compound MCO_3, while E_M, E_C and E_O are the ground state energies for M, C and O, respectively. The predicted ΔH_f values are presented in table 3-1 to table 3-3 respectively. The lower the heats of formation, the more stable is the system and vice versa. We note that our calculated heats of formations are relatively low and negative, suggesting thermodynamic stability for all the systems. However, F-doped $Ni_{0.3}Mn_{0.5}Co_2CO_3$ has the heat of formation of -6765.23 kJ/mol which is more negative as compared to other structures, this implies that F-doped $Ni_{0.3}Mn_{0.5}Co_2CO_3$ is more energetically favourable or thermodynamically stable. To the best of our knowledge, these are the first recorded heats of formation, lattice parameters, cell volumes and density for MCO_3

and MO_2 (M: Ni, Mn, Co) structures, hence these results could be used for benchmarking in the near future.

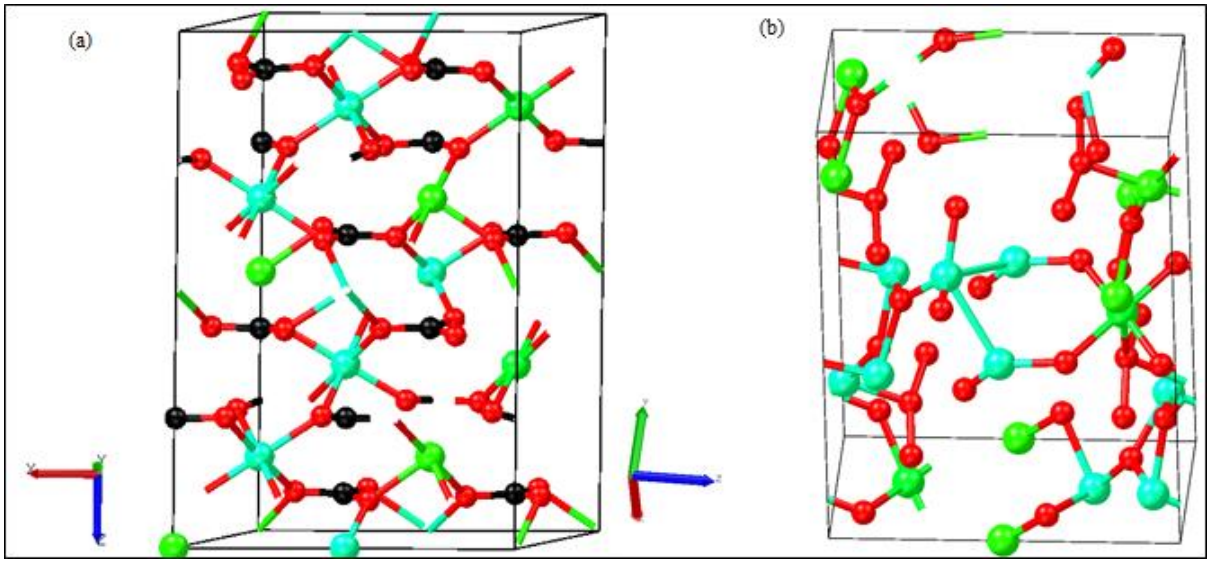

Figure 3-1. Optimised structures of (a) $Ni_{0.3}Mn_{0.5}Co_2CO_3$ and (b) $Ni_{0.3}Mn_{0.5}Co_2O_2$.

Table 3-1. Calculated lattice parameters for $Ni_{0.3}Mn_{0.5}Co_2CO_3$, F-doped $Ni_{0.3}Mn_{0.5}Co_2CO_3$, $Ni_{0.3}Mn_{0.5}Co_2O_2$ and F-doped $Ni_{0.3}Mn_{0.5}Co_2O_2$.

	$Ni_{0.3}Mn_{0.5}Co_2CO_3$	F-doped $Ni_{0.3}Mn_{0.5}Co_2CO_3$	$Ni_{0.3}Mn_{0.5}Co_2O_2$	F-doped $Ni_{0.3}Mn_{0.5}Co_2O_2$
a (Å)	9.108	9.235	8.100	16.812
b (Å)	4.584	4.709	3.000	2.925
c (Å)	13.876	14.092	8.479	8.618
V ($Å^3$)	500.600	524.659	437.271	416.961
Density (mg/m^3)	4.654	4.486	4.049	4.306
ΔH_f (kJ/mol)	-3518.43	-6765.23	-1666.14	-3661.88

Table 3-2. Calculated lattice parameters for Ti-doped $Ni_{0.3}Mn_{0.5}Co_2CO_3$, Ti-doped $Ni_{0.3}Mn_{0.5}Co_2O_2$, Nb-doped $Ni_{0.3}Mn_{0.5}Co_2CO_3$ and Nb-doped $Ni_{0.3}Mn_{0.5}Co_2O_2$

	Ti-doped $Ni_{0.3}Mn_{0.5}Co_2CO_3$	Ti-doped $Ni_{0.3}Mn_{0.5}Co_2O_2$	Nb-doped $Ni_{0.3}Mn_{0.5}Co_2CO_3$	Nb-doped $Ni_{0.3}Mn_{0.5}Co_2O_2$
a (Å)	9.107	17.789	9.107	17.789
b (Å)	4.584	3.000	4.584	3.000
c (Å)	13.871	8.479	13.869	8.479
V ($Å^3$)	500	437.271	500	437.270
Density(mg/m^3)	4.514	3.888	5.410	4.914
ΔH_f (kJ/mol)	-4180.41	-2445.26	-3122.41	-1772.69

Table 3-3. Calculated lattice parameters for Cr-doped $Ni_{0.3}Mn_{0.5}Co_2CO_3$ and Cr-doped $Ni_{0.3}Mn_{0.5}Co_2O_2$

	Cr-doped $Ni_{0.3}Mn_{0.5}Co_2CO_3$	Cr-doped $Ni_{0.3}Mn_{0.5}Co_2O_2$
a (Å)	9.107	17.789
b (Å)	4.584	3.000
c (Å)	13.869	8.479
V ($Å^3$)	500	437.271
Density (mg/m^3)	4.596	3.982
ΔH_f (kJ/mol)	-2931.83	-1612.71

3.2. Electronic Properties

The state and behavior of the electrons in the material are completely described by a collection of characteristics and representations known as the electronic properties. This section focuses on the electronic band structure, which characterizes the state of electrons in terms of their energy and electronic density of states which determines the properties of metals.

3.2.1. Band Structure

In this section we present and discuss the calculated electronic band structures (BS) for structures within this study and their doped systems. Electronic band structures are plots of energy versus wave-vectors for a number of bands. They help in determining if the material is an insulator, semiconductor or conductor/metal by defining the size of the energy band gaps around the Fermi level. An energy band gap is the distance between the valence band and the conduction band of electrons.

In Figure 3-2, we present the calculated spin polarised electronic band structures for (a) $Ni_{0.3}Mn_{0.5}Co_2CO_3$ and (b) $Ni_{0.3}Mn_{0.5}Co_2O_2$ at ambient pressure and temperature. For (a) $Ni_{0.3}Mn_{0.5}Co_2CO_3$ we note that the system is a semiconductor with a direct gap of 0.004 eV. The valence band maximum is located near (0.00 0.00 0.00), at 0.013 eV with respect to the Fermi level while the conduction band minimum is located near (0.00 0.00 0.00), at 0.016 eV with respect to the Fermi level. The centre of the gap is located at 0.015 eV with respect to the Fermi level. Figure 3-2 (b) shows that the system is a semiconductor with a direct gap of 0.036 eV. We note that valence band maximum for this structure is located near (0.00 0.00 0.00) at -0.040 eV while the conduction band minimum is located near (0.00 0.00 0.00) at -0.004 eV. The centre of the gap is located at -0.022 eV with respect to the Fermi level which is used as the zero of the energy scale.

Figure 3-3 to 3-6 show the electronic band structures for doped systems. Figure 3-3 presents the energy band structures for F-doped $Ni_{0.3}Mn_{0.5}Co_2CO_3$ and F-doped $Ni_{0.3}Mn_{0.5}Co_2O_2$. Contrary to $Ni_{0.3}Mn_{0.5}Co_2CO_3$, it is seen that there are energy bands crossing the fermi energy level in both spin directions, indicating that this system is metallic. The Fermi energy in F-doped $Ni_{0.3}Mn_{0.5}Co_2CO_3$ is located in the band interval (#203 - #203) spanning the energy interval (-0.014:-0.014) eV with respect to the Fermi level. For F-doped $Ni_{0.3}Mn_{0.5}Co_2O_2$, the system is a magnetic semiconductor with a direct gap of 0.077 eV. The valence band maximum is located near (0.00 0.00 0.00) at -0.067 eV while the conduction band minimum is located near (0.00 0.00 0.00), at 0.009 eV with respect to the Fermi level. Figure 3-4 depicts the energy band structures for Ti-doped $Ni_{0.3}Mn_{0.5}Co_2CO_3$ and Ti-doped $Ni_{0.3}Mn_{0.5}Co_2O_2$. The band structure for Ti-doped $Ni_{0.3}Mn_{0.5}Co_2CO_3$ shows a magnetic semiconductor behaviour with a direct gap of 0.043 eV. Furthermore, the valence band maximum is located near (0.00 0.00 0.00) at -0.019 eV with the conduction band minimum located near (0.00 0.00 0.00), at 0.025 eV with respect to the Fermi level. Similarly to Ti-doped $Ni_{0.3}Mn_{0.5}Co_2CO_3$, the energy band structure for Ti-doped $Ni_{0.3}Mn_{0.5}Co_2O_2$ depicts a magnetic semiconductor with a direct gap of 0.013 eV. We also note the valence band maximum located near (0.00 0.00 0.00), at -0.007 eV while the conduction band minimum is located near (0.00 0.00 0.00), at 0.005 eV with respect to the Fermi level.

In Fig. 3-5, we note the energy band structures for (a) Nb-doped $Ni_{0.3}Mn_{0.5}Co_2CO_3$ and (b) Nb-doped $Ni_{0.3}Mn_{0.5}Co_2O_2$. For Nb-doped $Ni_{0.3}Mn_{0.5}Co_2CO_3$, the system is a magnetic semiconductor with a direct gap of 0.023 eV. The valence band maximum of this structure is located near (0.00 0.00 0.00), at -0.003 eV with respect to the Fermi level while the conduction band minimum is located near (0.00 0.00 0.00), at 0.020 eV with respect to the Fermi level. Moreover, Fig. 3-6 shows the energy band structures for (a) Cr-doped $Ni_{0.3}Mn_{0.5}Co_2CO_3$ and

(b) Cr-doped $Ni_{0.3}Mn_{0.5}Co_2O_2$. For Cr-doped $Ni_{0.3}Mn_{0.5}Co_2CO_3$, the system is a semiconductor with a direct gap of 0.007 eV. The valence band maximum is located near (0.00 0.00 0.00), at -0.005 eV with respect to the Fermi level while the conduction band minimum is located near (0.00 0.00 0.00), at 0.003 eV with respect to the Fermi level. Also for Cr-doped $Ni_{0.3}Mn_{0.5}Co_2O_2$, the system is a magnetic semiconductor with a direct gap of 0.052 eV with the valence band maximum located near (0.00 0.00 0.00) at -0.013 eV while the conduction band minimum is located near (0.00 0.00 0.00), at 0.039 eV with respect to the Fermi level.

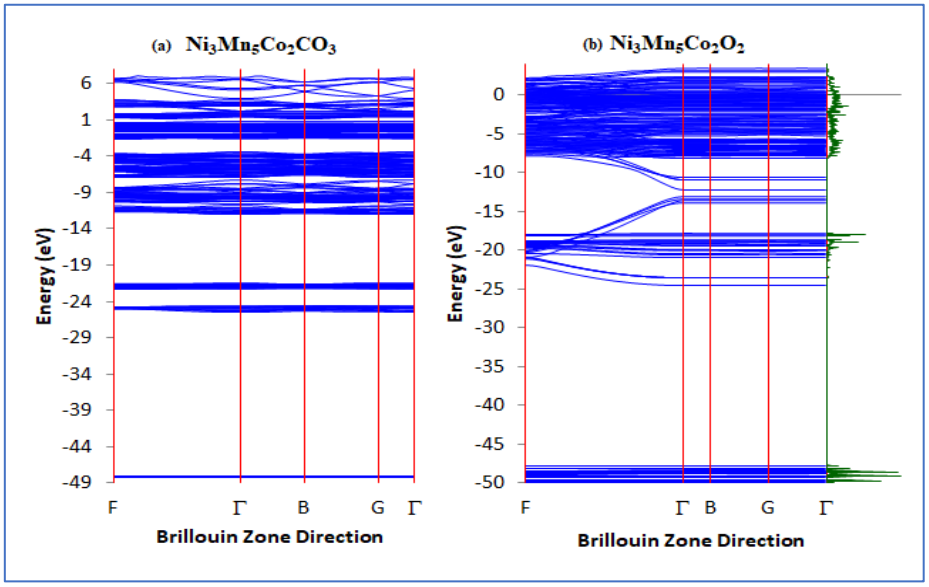

Figure 3-2. Energy band structures for (a) $Ni_{0.3}Mn_{0.5}Co_2CO_3$ and (b) $Ni_{0.3}Mn_{0.5}Co_2O_2$.

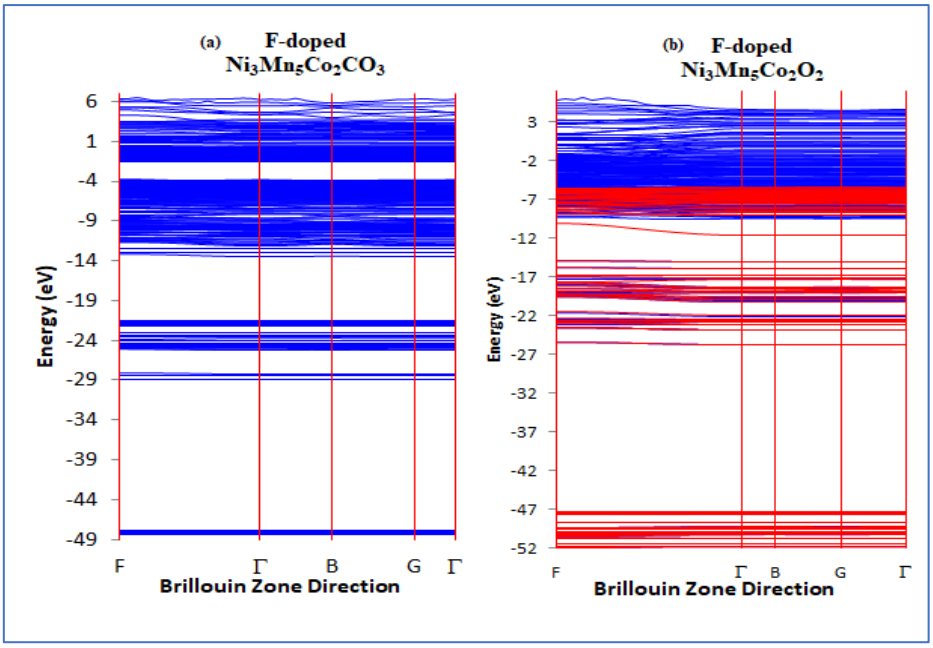

Figure 3-3. Energy band structures for (a) F-doped $Ni_{0.3}Mn_{0.5}Co_2CO_3$ and (b) F-doped $Ni_{0.3}Mn_{0.5}Co_2O_2$.

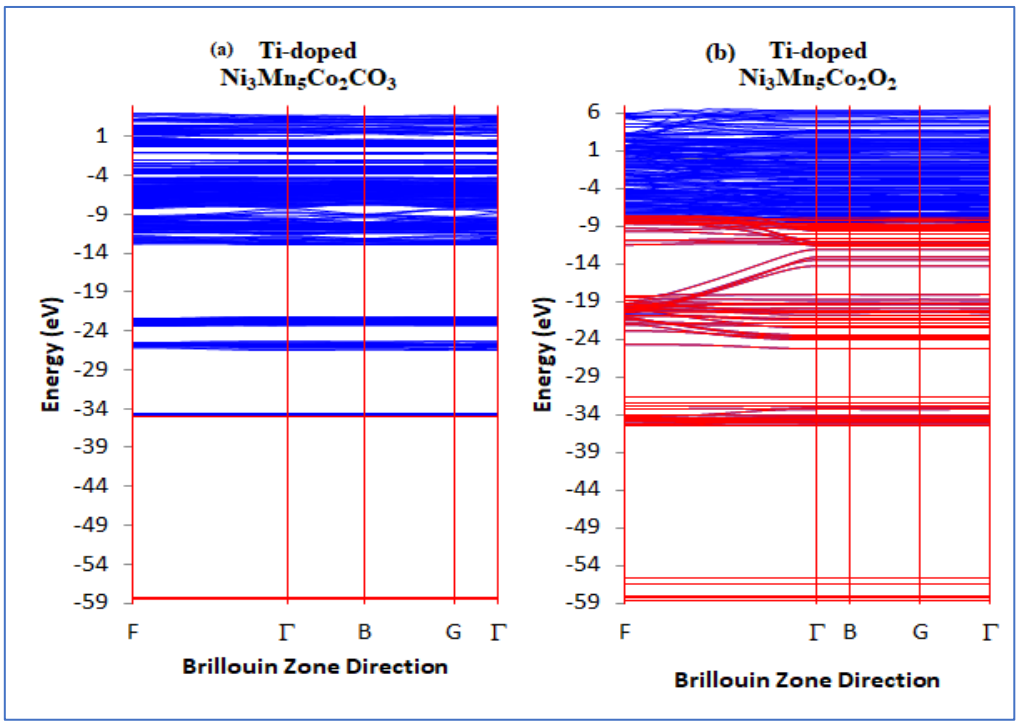

Figure 3-4. Energy band structures for (a) Ti-doped $Ni_{0.3}Mn_{0.5}Co_2CO_3$ and (b) Ti-doped $Ni_{0.3}Mn_{0.5}Co_2O_2$.

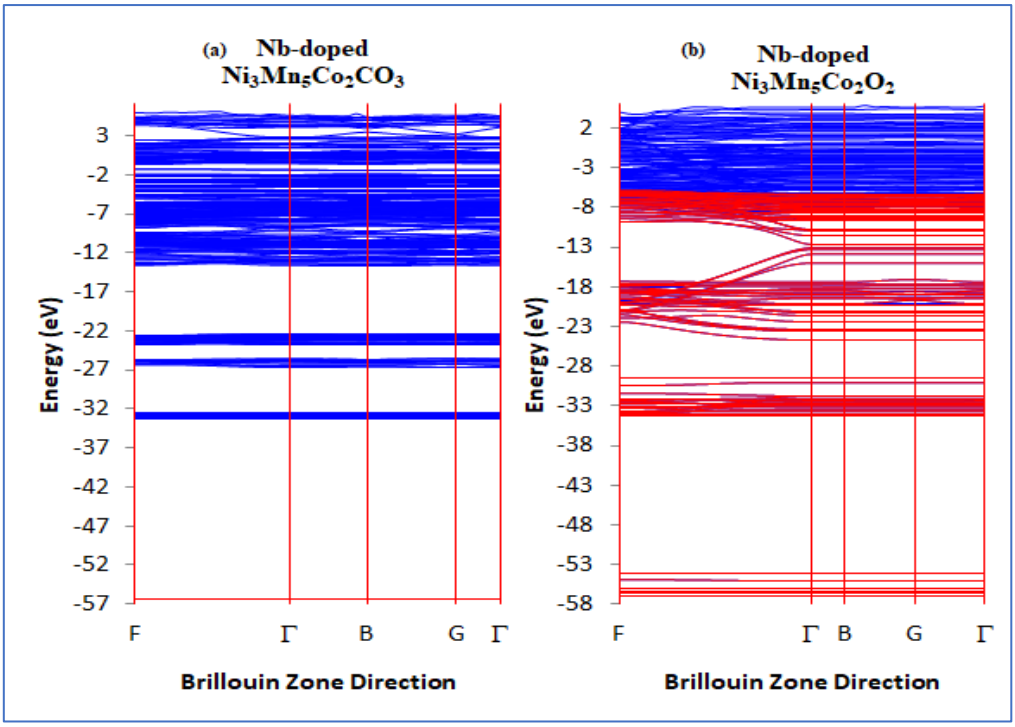

Figure 3-5. Energy band structures for (a) Nb-doped $Ni_{0.3}Mn_{0.5}Co_2CO_3$ and (b) Nb-doped $Ni_{0.3}Mn_{0.5}Co_2O_2$.

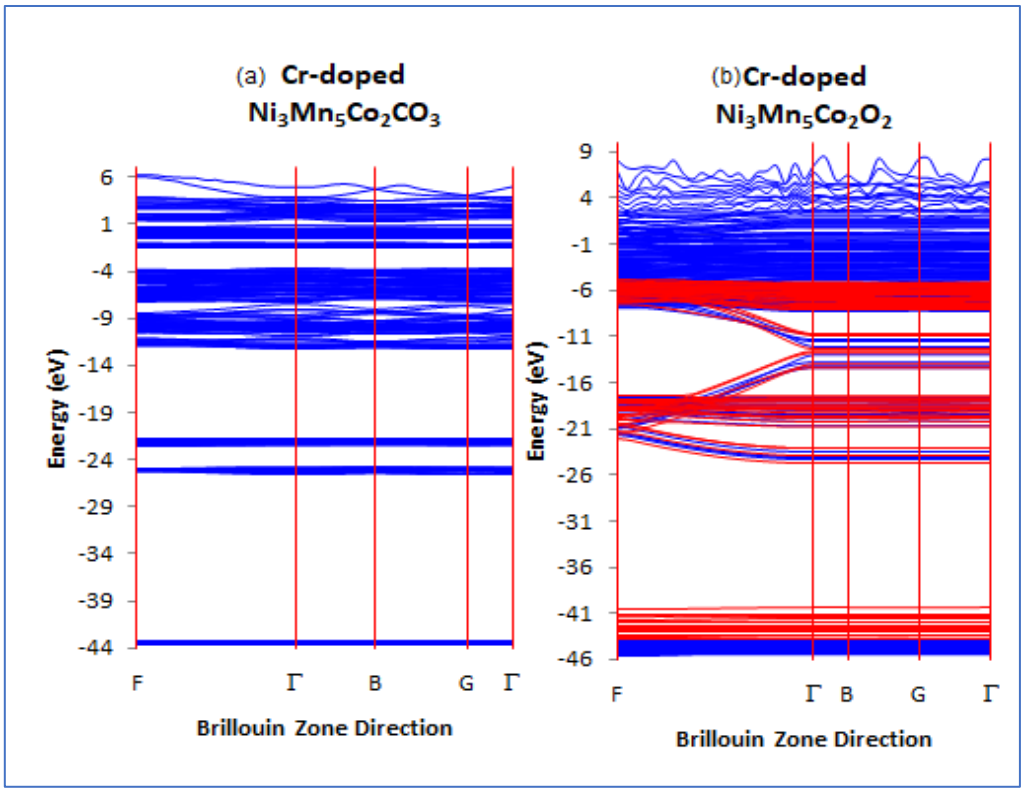

Figure 3-6. Energy band structures for (a) Cr-doped $Ni_{0.3}Mn_{0.5}Co_2CO_3$ and (b) Cr-doped $Ni_{0.3}Mn_{0.5}Co_2O_2$.

3.2.2. Density of states

Density of states (DOS) is referred to as the energy levels that can be occupied by electrons of different number of states. The density of states for structures of the same composition can be used to check the stability trend with respect to their behaviour at the Fermi level (E_f). The number of electron states per unit energy interval is measured by the electron density of states, a physical quantity, while the distribution of energy levels is continuous. Understanding and assessing the bonding characteristics of materials from a microscopic perspective depends on the electronic density of states. Figure 3-7 to 3-11 display the total and partial density of states for pure and doped structures within the study. The total and partial density of state calculations were computed using the spin polarised local density approximation with Hubbard correction (U) at ambient pressure and temperature conditions. The top most plots in all the figures display total DOS while the subsequent lower plots display partial DOS. The spin up states are shown on the positive scale of TDOS while the spin down states are shown on the negative scale of TDOS. The total electronic contribution of whole system is indicated by the total DOS while the contributions of each individual atom is indicated by the partial DOS. Moreover, the Fermi energy is taken as the energy zero ($E-E_F=0$) in all the plots. The energy bands can be analysed from the DOS, which is in correspondence to the number of states available to electrons per unit cell at a specified energy.

Figure 3-7 presents the total (TDOS) and partial density of states (PDOS) for $Ni_{0.3}Mn_{0.5}Co_2CO_3$ and $Ni_{0.3}Mn_{0.5}Co_2O_2$. For $Ni_{0.3}Mn_{0.5}Co_2CO_3$, we note that peaks that appears on the valence band side of the total DOS are mainly contributed by manganese d-states and carbon p-states with minor amounts of nickel d-states and cobalt d-states. We also note the presence of pseudogap and that the Fermi level lies on the right of it, thus permissible for valence band states to overlap to the conduction band. The existence of pseudogap suggests

that $Ni_{0.3}Mn_{0.5}Co_2CO_3$ has a metallic behaviour characteristics and good electronic conduction since no energy band gap is observed, which correspond well with the band structure prediction. Furthermore, for $Ni_{0.3}Mn_{0.5}Co_2O_2$ structure, we note that peaks in the total DOS are dominated by nickel and cobalt d-states and oxygen p-states. We also note a small pseudogap with the Fermi line lying on the left of the pseudogap. This also indicate a metallic behaviour because no energy band gap is observed in this case.

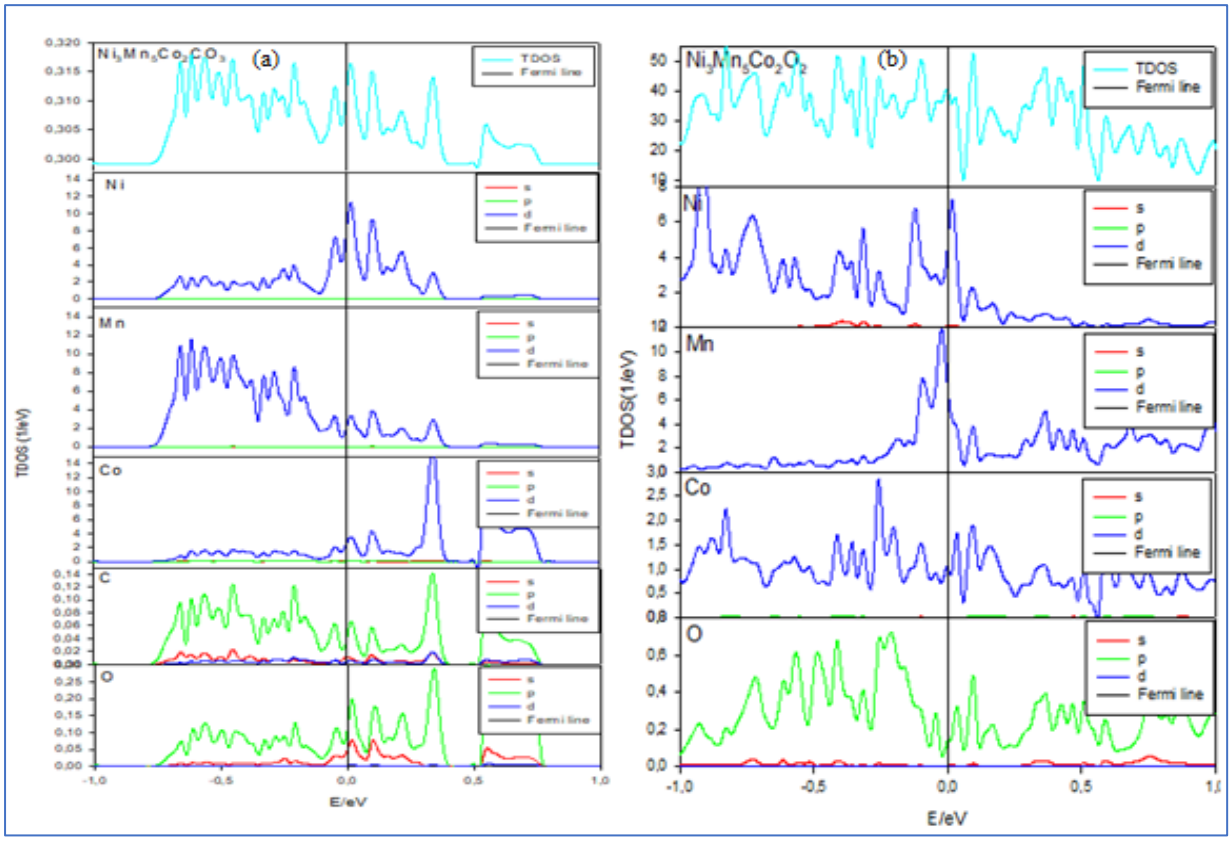

Figure 3-7. Total and Partial density of states for (a) $Ni_{0.3}Mn_{0.5}Co_2CO_3$ and (b) $Ni_{0.3}Mn_{0.5}Co_2O_2$.

In this section we discuss the calculated spin polarized total and partial density of states (DOS) for fluorine doped $Ni_{0.3}Mn_{0.5}Co_2CO_3$ and fluorine doped $Ni_{0.3}Mn_{0.5}Co_2O_2$ systems at Oxygen sites. Similarly to pure systems ($Ni_{0.3}Mn_{0.5}Co_2CO_3$), Figure 3-8 (a) shows a pseudogap at the Fermi line indicating metallic behaviour. In this energy range (-1.0 to 1.0 eV), the partial

density of states associated with the Ni, Mn and Co states are primarily of 3*d* character while the density of states associated with the F, C and O sites are primarily of 2*p* character respectively. Moreover, Figure 3-8 (b) shows a half-metallic ferromagnet which indicate that this material can either act as a semiconductor or metal. We further note that the upper spins in the valence band of the total DOS are dominated by Ni 3d states and F 2p states while the lower spins are dominated by Ni and Mn 3d states and O 2p states. We also observe no energy band gap around the Fermi level, but a continuous flow of electrons from the valence to the conduction band at ambient pressure. Hence, doping with fluorine plays an essential role on the enhancement of the electronic conductivity.

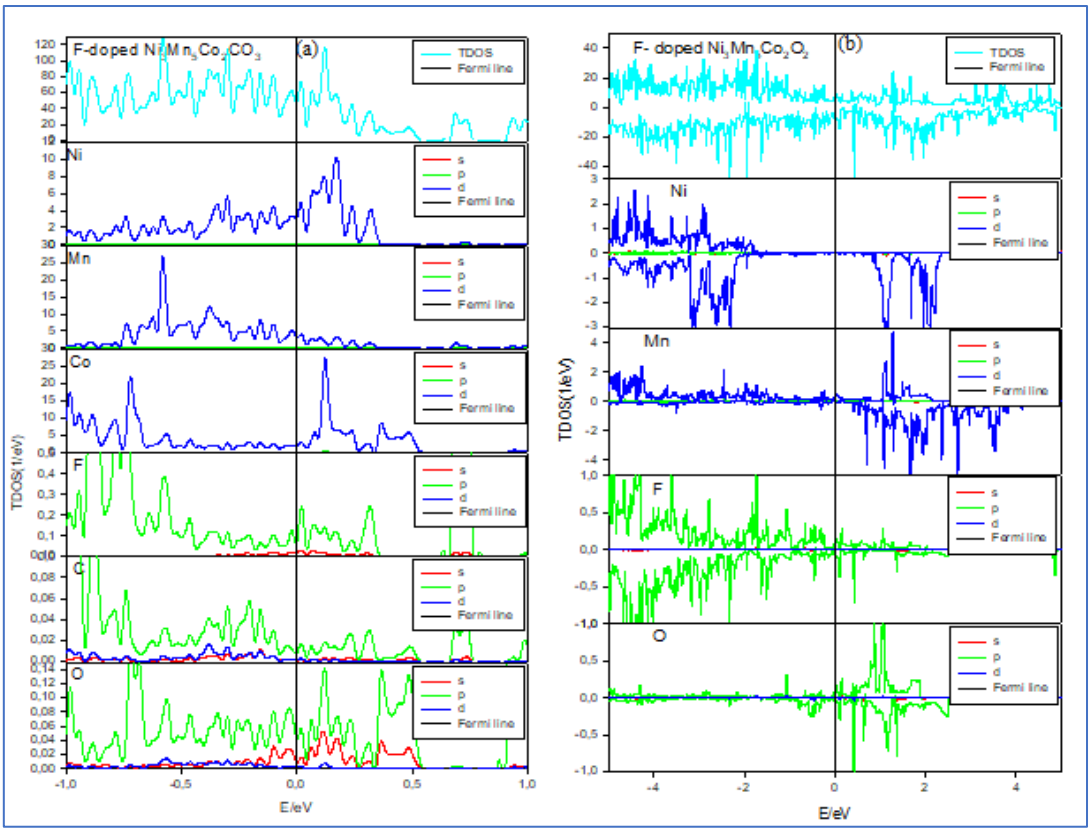

Figure 3-8. Total and Partial density of states for (a) F-doped $Ni_{0.3}Mn_{0.5}Co_2CO_3$ and (b) F-doped $Ni_{0.3}Mn_{0.5}Co_2O_2$.

Figure 3-9 depicts the total and partial density of states for titanium doped $Ni_{0.3}Mn_{0.5}Co_2CO_3$ and titanium doped $Ni_{0.3}Mn_{0.5}Co_2O_2$ at Mn sites. For Ti-doped $Ni_{0.3}Mn_{0.5}Co_2CO_3$, the system

shows a half metallic ferromagnet which indicate that bands for spin 2 are metallic while bands for spin 1 are semiconducting. The spin up and spin down at the Fermi level are dominated by Ti 3p states with minor amounts of carbon and oxygen 2p states. The spin up and spin down peaks at the valence site are dominated by nickel and cobalt 3d states and oxygen 2p states. For Ti-doped $Ni_{0.3}Mn_{0.5}Co_2O_2$, the system is a magnetic metal. We note that the contribution of peaks at the Fermi line are mainly from nickel 3d states while the contribution of valence bands is mainly from Ni and Co 3d states.

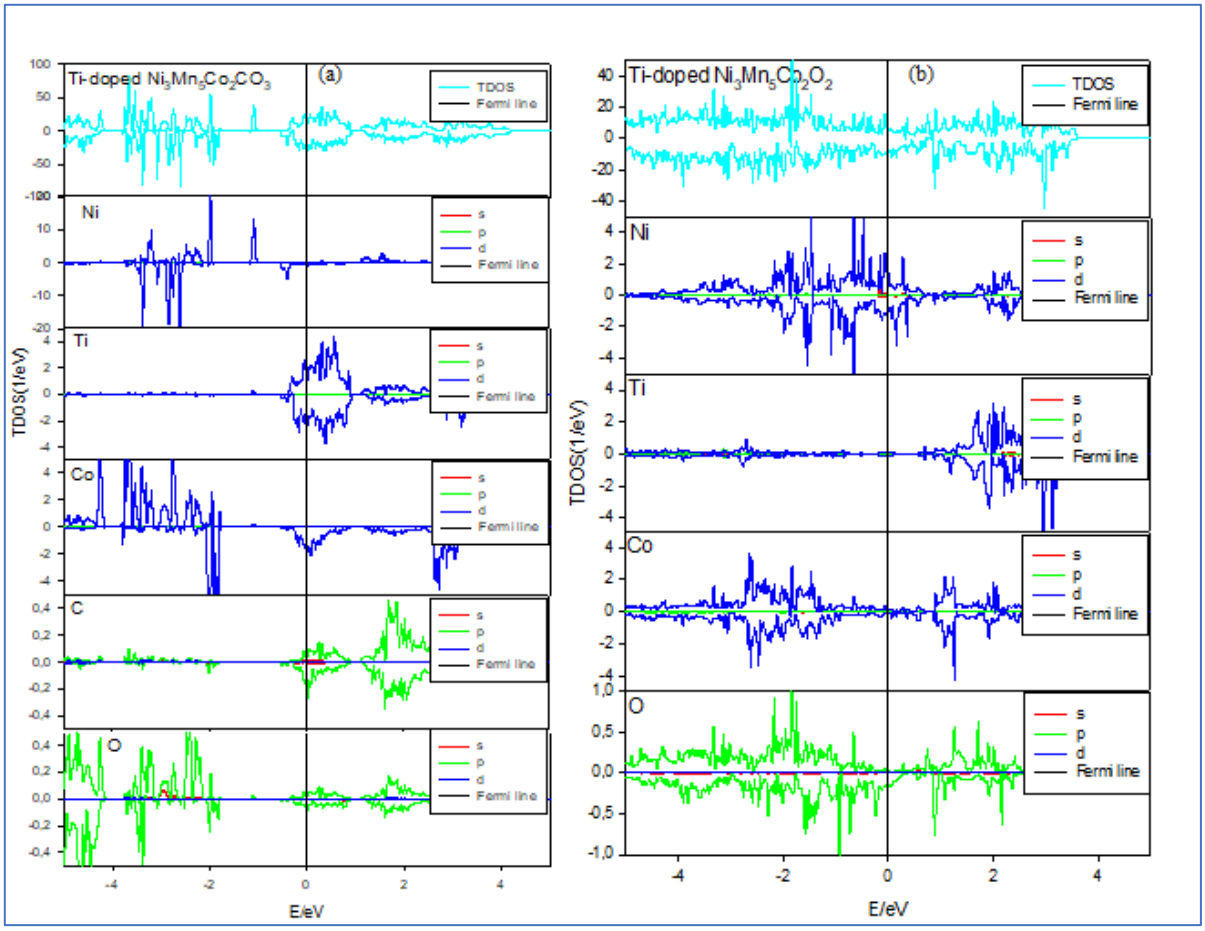

Figure 3-9. Total and Partial density of states for (a) Ti-doped $Ni_{0.3}Mn_{0.5}Co_2CO_3$ and (b) Ti-doped $Ni_{0.3}Mn_{0.5}Co_3O_2$.

Figure 3-10 presents the total and partial density of states for Nb-doped $Ni_{0.3}Mn_{0.5}Co_2CO_3$ and Nb-doped $Ni_{0.3}Mn_{0.5}Co_2O_2$. From Fig. 3-10 (a), we note flow of electrons from the valence

bands to the conduction bands with indicate that no energy band gap is recorded for this system. This system is a half metallic ferromagnetic with bands for spin 1 being metallic and bands for spin 2 semiconducting. The contribution of the behaviour at the Fermi line of the total DOS is mainly contributed by niobium 3d states and carbon 2p states. On the other hand, the total and partial DOS for Nb-doped $Ni_{0.3}Mn_{0.5}Co_2O_2$ shows a half-metallic ferromagnet behaviour with bands for spin 2 being metallic and spin 1 bands semiconducting. The valence band maximum for this structure is located near (0.00 0.44 0.00), at -0.092 eV while the conduction band minimum is located near (0.50 0.22 0.00), at -0.518 eV with respect to the Fermi level.

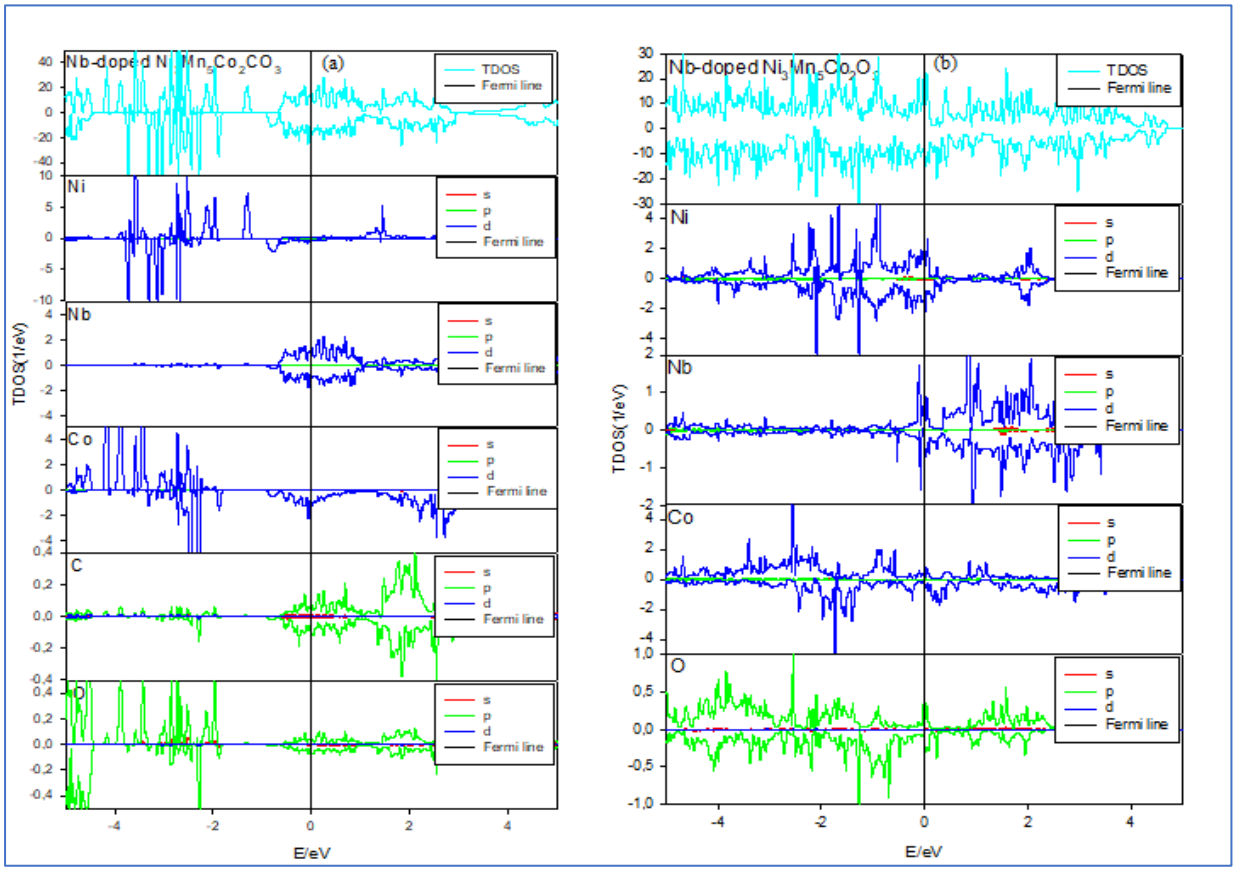

Figure 3-10. Total and Partial density of states for (a) Nb-doped $Ni_{0.3}Mn_{0.5}Co_2CO_3$ and (b) $Ni_{0.3}Mn_{0.5}Co_2O_2$.

Figure 3-11 shows partial and density of states for (a) Cr-doped $Ni_{0.3}Mn_{0.5}Co_2CO_3$ and (b) Cr-doped $Ni_{0.3}Mn_{0.5}Co_2O_2$. For Cr-doped $Ni_{0.3}Mn_{0.5}Co_2CO_3$, we note that the system is half metallic ferromagnet, indicating that bands for spin 1 are metallic while bands for spin 2 are semiconducting. The valence band maximum for this structure is located near (0.50 0.44 0.00), at -0.402 eV with respect to the Fermi level while the conduction band minimum is located near (0.00 0.33 0.00), at -0.647 eV. The spins in the total DOS are mainly dominated by nickel, chromium and cobalt 3d bands and oxygen 2p bands. Furthermore, for Cr-doped $Ni_{0.3}Mn_{0.5}Co_2O_2$ we note a similar behaviour as compared to Cr-doped $Ni_{0.3}Mn_{0.5}Co_2CO_3$. We note that the system is a half metallic ferromagnet whereby spin 1 bands are metallic while spin 2 bands are semiconducting. The bands dominating the total DOS are mainly dominated by oxygen 2p bands and also nickel, chromium and cobalt 3d bands.

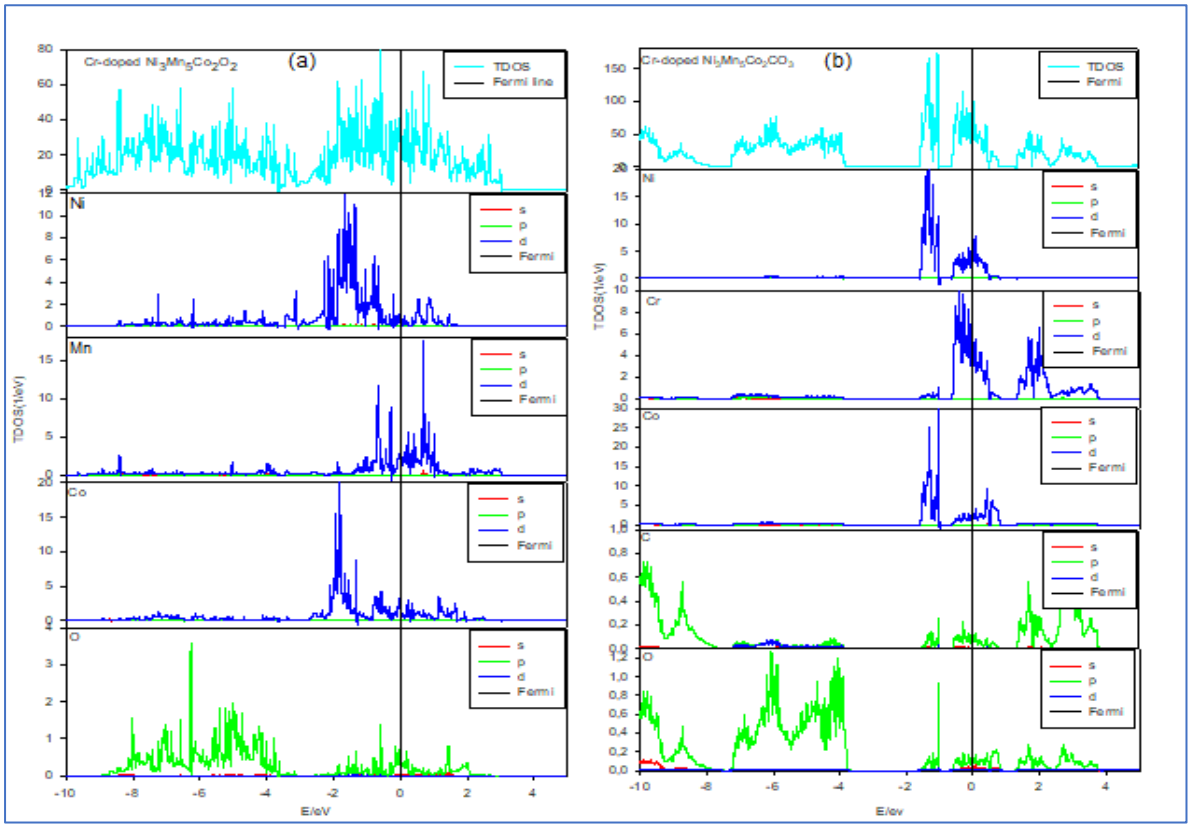

Figure 3-11. Total and Partial density of states for (a) Cr-doped $Ni_{0.3}Mn_{0.5}Co_2O_2$ and (b) Cr-doped $Ni_{0.3}Mn_{0.5}Co_2CO_3$.

3.3. Elastic properties

Elastic constants are determined to estimate the mechanical properties of materials. The ability of materials to resist against exterior forces within the elastic limit (i.e., reflect the stiffness of the material) can be determined by elastic constants. Understanding of elastic constants, moduli and anisotropy is crucial as they determine the response of materials to the applied stress. Elastic constants also provide essential information on mechanical stability, stiffness, hardness, brittleness/ductility nature, susceptibility to cracks induced due to thermal expansion coefficient and nature of the forces acting in solid materials. These mechanical properties can be measured by bulk modulus B, shear modulus G, Young modulus E and Pugh ratio ($\frac{B}{G}$). Elastic constants (C_{ij}) for this study were calculated by Taylor expansion of the total energy as shown below [133];

$$U(V,\varepsilon) = U(V_0,0) + V_0\left[\sum_i \tau_i\varepsilon_i\delta_i + \frac{1}{2}\sum_{ij} C_{ij}\,\varepsilon_i\delta_i\varepsilon_j\delta_i\right] \quad (3\text{-}2)$$

Where $U(V_{0,}0)$ is the energy of the unstrained system with equilibrium volume were V_0, τ_i is element in the stress tensor and ξ_i is a factor to take care of Voigt index. From our calculations, we observe 21 independent elastic constants which falls within the triclinic lattice systems. For triclinic systems to be considered mechanically stable, the following necessary and sufficient Born stability conditions must be satisfied [134, 135].

$$C_{11} > 0, C_{22} > 0, C_{33} > 0, C_{44} > 0, C_{55} > 0, C_{66} > 0,$$

$$[C11 + C22 + C33 + 2\,X\,(C12 + C13 + C23)] > 0, \quad (3\text{-}3)$$

$$(C33XC55 - C_{35}^2) > 0, (C44XC66 - \ C_{46}^2) > 0,$$

$$C22 + C33 - 2XC23) > 0$$

The calculated elastic constants for structures of this study are presented in Table 3-2 and 3-4. We note that the stability conditions for $Ni_{0.3}Mn_{0.5}Co_2CO_3$ and F-doped $Ni_{0.3}Mn_{0.5}Co_2CO_3$ are satisfied, indicating mechanical stability. On the other hand, $Ni_{0.3}Mn_{0.5}Co_2O_2$ shows a negative value of C_{55}, hence the stability condition $C_{55} > 0$ is not satisfied suggesting mechanical instability. We also note that Ti- doped $Ni_{0.3}Mn_{0.5}Co_2CO_3$ and Nb-doped $Ni_{0.3}Mn_{0.5}Co_2CO_3$ satisfy the stability criterion for triclinic systems which indicate mechanical stability, while the Ti-doped $Ni_{0.3}Mn_{0.5}Co_2O_2$ and Nb-doped $Ni_{0.3}Mn_{0.5}Co_2O_2$ does not satisfy the stability conditions since they show negative values of C_{55} and C_{66}, which implies mechanical instability. From the calculated elastic constants, the macroscopic bulk (B), shear (G) and Young's (E) moduli were estimated using the Voigt-Ruess-Hill approximation method [136, 137, 138]. The Voigt and Ruess theory correspond to the upper and lower limits respectively, while the Hill theory is the average of the Voigt and Reuss respectively. The bulk (B) modulus determines the material's hardness and resistance to compression under pressure.

From our calculations as presented in Table 3-3 and 3-5, it can be observed that Ti-doped $Ni_{0.3}Mn_{0.5}Co_2CO_3$ system possesses highest hardness over other systems for the study respectively, due to its largest value of bulk modulus (182.86 GPa). The shear (G) modulus describes the response of materials to deformation against external forces. We note that Nb-doped $Ni_{0.3}Mn_{0.5}Co_2CO_3$ has the highest shear modulus value (1134.05 GPa), indicating highest resistance over $Ni_{0.3}Mn_{0.5}Co_2O_2$, $Ni_{0.3}Mn_{0.5}Co_2CO_3$, F-doped $Ni_{0.3}Mn_{0.5}Co_2CO_3$ and F-doped $Ni_{0.3}Mn_{0.5}Co_2O_2$, Ti-doped $Ni_3Mn_5Co_2O_2$, Ti-doped $Ni_{0.3}Mn_{0.5}Co_2CO_3$ and Nb-doped $Ni_{0.3}Mn_{0.5}Co_2O_2$, respectively. It is interesting to note that shear modulus is greater than bulk modulus in $Ni_{0.3}Mn_{0.5}Co_2O_2$, Ti-doped $Ni_{0.3}Mn_{0.5}Co_2O_2$ and Nb-doped $Ni_{0.3}Mn_{0.5}Co_2CO_3$. This means that $Ni_{0.3}Mn_{0.5}Co_2O_2$, Ti-doped $Ni_{0.3}Mn_{0.5}Co_2O_2$ and Nb-doped $Ni_{0.3}Mn_{0.5}Co_2CO_3$ has greater stiffness than hardness and resistance to deformation, thus greater susceptibility

cracks when subjected under pressure. In the other systems, the bulk is greater than the shear implying that shear modulus is the parameter limiting stability.

The Young modulus (E) which determines stiffness of materials showed that Nb-doped $Ni_{0.3}Mn_{0.5}Co_2CO_3$ possesses greater stiffness over other structures respectively. In order to determine the brittleness and ductility nature of our structures, we have calculated the B/G ratio as proposed by Pugh [139]. Materials are considered ductile if the Pugh ratio value is greater than 1.75 and brittle if less than 1.75. From our calculated Pugh ratio as shown in Table 3-3 and 3-5, we note that $\frac{B}{G}$ is greater than 1.75 for $Ni_{0.3}Mn_{0.5}Co_2CO_3$, F-doped $Ni_{0.3}Mn_{0.5}Co_2CO_3$, F-doped $Ni_{0.3}Mn_{0.5}Co_2O_2$ and Ti-doped $Ni_{0.3}Mn_{0.5}Co_2CO_3$ suggesting ductility (i.e. the ability to bend without deformation). On the other hand, the Pugh ratio values for $Ni_{0.3}Mn_{0.5}Co_2O_2$, Ti-doped $Ni_{0.3}Mn_{0.5}Co_2O_2$, Nb-doped $Ni_{0.3}Mn_{0.5}Co_2O_2$ and Nb-doped $Ni_{0.3}Mn_{0.5}Co_2CO_3$ are less than 1.75, suggesting brittleness (i.e. structural deformation after bending).

The materials anisotropies were calculated by making use of the universal elastic anisotropy (A^U) which quantifies single crystal elastic anisotropy. Anisotropy factors are essential to determine the susceptibility of materials to cracks and in reducing micro-cracks and dislocation [140]. The universal elastic anisotropy index is defined by equation 3-4 below:

$$A^U = 5\frac{G^V}{G^R} + \frac{B^V}{B^R} - 6 \qquad (3\text{-}4)$$

Where G is the shear modulus, B is the bulk modulus and the superscripts V and R denote the Voigt and Reuss bounds respectively for the ensemble averaged quantities over the crystal. For isotropic crystals, A^U = 0 while larger values of A^U indicate stronger anisotropy. As shown in Table 3-4, We note that $Ni_{0.3}Mn_{0.5}Co_2CO_3$, $Ni_{0.3}Mn_{0.5}Co_2O_2$, F-doped $Ni_{0.3}Mn_{0.5}Co_2CO_3$ and

F-doped $Ni_{0.3}Mn_{0.5}Co_2O_2$ show larger values of A^U which indicate that these systems possesses highest anisotropy, hence greatest susceptibility to cracks.

Table 3-4. Calculated elastic constants for $Ni_{0.3}Mn_{0.5}Co_2CO_3$, $Ni_{0.3}Mn_{0.5}Co_2O_2$, F-doped $Ni_{0.3}Mn_{0.5}Co_2CO_3$ and F-doped $Ni_{0.3}Mn_{0.5}Co_2O_2$.

C_{ij}	$Ni_{0.3}Mn_{0.5}Co_2CO_3$	$Ni_{0.3}Mn_{0.5}Co_2O_2$	F-doped $Ni_{0.3}Mn_{0.5}Co_2CO_3$	F-doped $Ni_{0.3}Mn_{0.5}Co_2O_2$
C_{11}	394.57	102.54	257.98	76.71
C_{12}	136.67	62.64	101.84	19.23
C_{13}	92.25	60.04	81.71	34.00
C_{14}	35.50	0.92	21.06	-23.16
C_{15}	-0.67	8.94	11.87	-13.05
C_{16}	0.58	-2.05	15.77	9.69
C_{22}	360.51	479.13	237.94	333.44
C_{23}	99.10	65.84	79.55	20.14
C_{24}	-37.90	0.51	-7.24	-6.35
C_{25}	-0.20	-6.28	6.66	-6.35
C_{26}	24.63	-0.71	25.01	4.71
C_{33}	183.83	124.71	113.68	82.12
C_{34}	-5.25	-1.44	8.11	-41.94
C_{35}	-11.34	-40.49	21.03	2.59
C_{36}	-4.04	-2.91	-9.56	4.91
C_{44}	59.21	30.45	50.73	124.69
C_{45}	0.51	0.05	2.80	6.43
C_{46}	-2.08	29.11	1.01	40.40

C_{55}	53.71	-1.63	49.28	17.41
C_{56}	28.04	-0.61	20.65	-7.50
C_{66}	107.81	125.77	74.98	-252.42

Table 3-5. Calculate Moduli, Pugh ratio and Anisotropy for $Ni_{0.3}Mn_{0.5}Co_2CO_3$, $Ni_{0.3}Mn_{0.5}Co_2o_2$, F-doped $Ni_{0.3}Mn_{0.5}Co_2CO_3$ and F-doped $Ni_{0.3}Mn_{0.5}Co_2O_2$.

(GPa)	$Ni_{0.3}Mn_{0.5}Co_2CO_3$	$Ni_{0.3}Mn_{0.5}Co_2O_2$	F-doped $Ni_{0.3}Mn_{0.5}Co_2CO_3$	F-doped $Ni_{0.3}Mn_{0.5}Co_2O_2$
B	164.07	104.65	110.82	58.24
G	74.33	116.44	50.28	20.13
E	263.19	237.42	131.03	49.76
$\frac{B}{G}$	2.21	0.89	2.204	2.89
A^U	6.52	2.72	7.45	2.65

Table 3-6. Elastic constants for Ti-doped $Ni_{0.3}Mn_{0.5}Co_2CO_3$, Ti-doped $Ni_{0.3}Mn_{0.5}Co_2O_2$, Nb-doped $Ni_{0.3}Mn_{0.5}Co_2CO_2$ and Nb-doped $Ni_{0.3}Mn_{0.5}Co_2O_2$

C_{ij}	Ti-doped $Ni_{0.3}Mn_{0.5}Co_2CO_3$	Ti-doped $Ni_{0.3}Mn_{0.5}Co_2O_2$	Nb-doped $Ni_{0.3}Mn_{0.5}Co_2CO_3$	Nb-doped $Ni_{0.3}Mn_{0.5}Co_2O_2$
C_{11}	347.62	43.94	463.25	149.58
C_{12}	227.63	97.57	168.02	181.89
C_{13}	135.02	36.27	189.04	68.17
C_{14}	52.47	11.12	29.34	6.62

C_{15}	-18.35	25.39	27.11	-5.54
C_{16}	66.07	1.30	34.76	2.92
C_{22}	304.42	529.01	329.55	472.20
C_{23}	135.66	53.33	227.92	-19.97
C_{24}	-31.75	-1.28	-15.90	92.89
C_{25}	-41.79	-46.72	-3.44	-617.42
C_{26}	-16.56	-41.44	88.21	-14.93
C_{33}	176.11	55.43	227.06	120.93
C_{34}	4.15	5.22	-1.24	-66.38
C_{35}	-23.61	-15.45	-2.44	31.75
C_{36}	-4.40	-0.07	-32.05	41.92
C_{44}	72.36	26.99	66.76	59.36
C_{45}	6.80	-5.37	6.27	-5.76
C_{46}	-5.06	14.05	8.52	59.79
C_{55}	87.98	-14.36	78.81	-172.18
C_{56}	60.13	-9.68	38.34	-7.74
C_{66}	21.19	-21.86	78.89	262.01

Table 3-7. Moduli, Pugh ratio and Anisotropy for Ti-doped $Ni_{0.3}Mn_{0.5}Co_2CO_3$, Ti-doped $Ni_{0.3}Mn_{0.5}Co_2O_2$, Nb-doped $Ni_{0.3}Mn_{0.5}Co_2CO_3$ and Nb-doped $Ni_{0.3}Mn_{0.5}Co_2O_2$

(GPa)	Ti-doped $Ni_{0.3}Mn_{0.5}Co_2CO_3$	Ti-doped $Ni_{0.3}Mn_{0.5}Co_2O_2$	Nb-doped $Ni_{0.3}Mn_{0.5}Co_2CO_3$	Nb-doped $Ni_{0.3}Mn_{0.5}Co_2O_2$
B	182.86	76.91	235.16	312.51
G	82.56	91.97	1134.05	-1.36

E	211.31	143.42	880.22	-22.04
$\frac{B}{G}$	2.21	0.84	0.2	-230.17
A^U	2.99	8.02	-0.47	-9.44

Table 3-8. Elastic constants for Cr-doped $Ni_{0.3}Mn_{0.5}Co_2CO_3$ and Cr-doped $Ni_{0.3}Mn_{0.5}Co_2O_2$.

Cij	Cr-doped $Ni_{0.3}Mn_{0.5}Co_2CO_3$	Cr-doped $Ni_{0.3}Mn_{0.5}Co_2O_2$
C_{11}	390.30	-35.70
C_{12}	146.53	-256.21
C_{13}	101.71	287.72
C_{14}	30.94	-74.33
C_{15}	8.93	-195.92
C_{16}	-4.40	-168.97
C_{22}	365.81	266.37
C_{23}	115.93	437.99
C_{24}	-24.07	-223.61
C_{25}	-0.81	66.56
C_{26}	27.12	-138.55
C_{33}	171.48	-33.84
C_{34}	-2.21	-197.86
C_{35}	-4.55	-399.76
C_{36}	-12.91	63.44

C_{44}	62.72	-7.60
C_{45}	-2.31	-65.53
C_{46}	-0.60	-10.84
C_{55}	63.75	225.26
C_{56}	31.33	-287.39
C_{66}	95.17	-130.35

Table 3-9. Moduli, Pugh ratio and Anisotropy for Cr-doped $Ni_{0.3}Mn_{0.5}Co_2CO_3$ and Cr-doped $Ni_{0.3}Mn_{0.5}Co_2$.

(GPa)	Cr-doped $Ni_{0.3}Mn_{0.5}Co_2CO_3$	Cr-doped $Ni_{0.3}Mn_{0.5}Co_2O_2$
B	168.38	386.33
G	72.88	-725.08
E	191.06	-8607.81
$\frac{B}{G}$	2.31	-580.45

3.4. Phonon dispersion curves

In this section we present first-principles DFT mechanical properties results of $Ni_{0.3}Mn_{0.5}Co_2CO_3$ and $Ni_{0.3}Mn_{0.5}Co_2O_2$ together with their doped systems. In the same way that a photon represents a quantum of electromagnetic radiation, phonons are regarded as lattice vibrations that compare quanta of lattice vibration energy [141]. Most solid-state phenomena, including stability, specific heat, melting, thermal conductivity, and electrical conductivity, are explained by the theory of phonons and cannot be explained by static lattice theory [142]. Since phonons play a significant influence in many physical properties of solids, the study of phonons

is an essential component of solid state physics. There are two different sorts of phonons seen in the propagation wave's dispersion relations: an upper branch (optical branch) and a lower branch (acoustical branch). The two atoms in the unit cell move in opposition to one another for the optical branch (in the long-wavelength limit), and the light mass amplitude is higher. The displacement of both atoms for the acoustical branch has the same amplitude, direction, and phase (in the long-wavelength limit). In order to investigate the mechanical stability of the transition metal carbonates, we have calculated their phonon dispersion curves along symmetry direction within their respective first Brillouin zones. When analysing the phonon dispersion curves, structures are said to be stable if there are no negative frequencies (referred to as soft modes) along high symmetry directions.

The phonon dispersion curves were calculated using the PHONON code by Parlinski [143] as implemented in MedeA software, which allows phonon dispersion curves and thermodynamic properties such as vibrational heat capacity at constant volume, vibrational internal energy, entropy and free energy to be calculated. The supercell was constructed from the hexagonal cell with the interaction range of 10.0Å and the displacement of +/-0.06Å during the phonon dispersion curve calculations. The PHONON code allows for calculation of lattice dynamics, dispersion curves and phonon density spectra of crystals from either a set of force constants or from a set of Hellmann-Feyman forces computed within an ab initio program which optimises the structure of the crystalline supercell within constraints imposed by a crystallographic space group [144].

Figure 3-12 presents the phonon dispersion curves for $Ni_{0.3}Mn_{0.5}Co_2CO_3$ and $Ni_{0.3}Mn_{0.5}Co_2O_2$ at ambient pressure. We note that the $Ni_{0.3}Mn_{0.5}Co_2CO_3$ system display vibrations within the positive frequency and this entails that $Ni_{0.3}Mn_{0.5}Co_2CO_3$ is vibrationally stable. On the other

hand, the phonon dispersion curve for $Ni_{0.3}Mn_{0.5}Co_2O_2$ display negative frequency phonon branches (here referred to as soft modes) down to -29 THz at ambient pressure. These soft modes are observed along high symmetry directions in the Brillouin zone. The presence of soft modes suggests that $Ni_{0.3}Mn_{0.5}Co_2O_2$ system is vibrationally unstable.

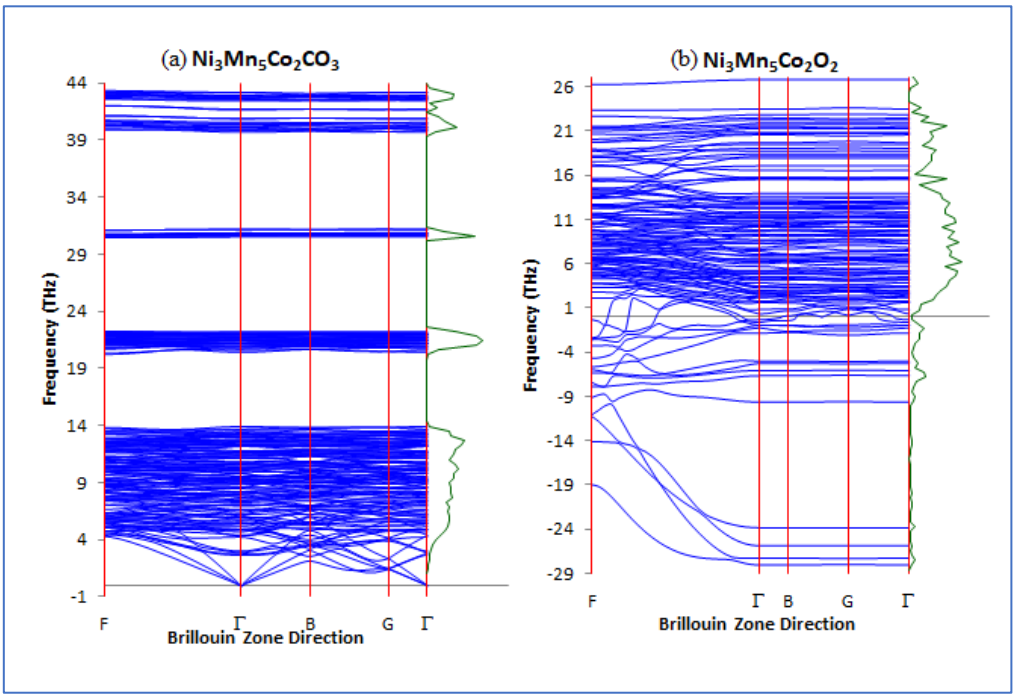

Figure 3-12. Phonon dispersion curves for (a) $Ni_{0.3}Mn_{0.5}Co_2CO_3$ and (b) $Ni_{0.3}Mn_{0.5}Co_2O_2$.

Figure 3-13 shows the phonon dispersions curves for fluorine doped $Ni_{0.3}Mn_{0.5}Co_2CO_3$ and $Ni_{0.3}Mn_{0.5}Co_2O_2$ systems. Similarly to pure $Ni_{0.3}Mn_{0.5}Co_2CO_3$ system, the phonon dispersion curve for fluorine doped $Ni_{0.3}Mn_{0.5}Co_2CO_3$ display no soft modes along the Brillouin zone indicating vibrational stability. We also note that doping $Ni_{0.3}Mn_{0.5}Co_2CO_3$ system with fluorine at the oxygen position does not change the behaviour of vibrations along the Brillouin zone direction as the system remains vibrationally stable. Contrary to fluorine doped $Ni_{0.3}Mn_{0.5}Co_2CO_3$, the phonon dispersion curve for fluorine doped $Ni_{0.3}Mn_{0.5}Co_2O_2$ shows

negative vibrations (soft modes) in the Brillouin zone direction which implies vibrational instability. However, we note that the negative vibrations for pure $Ni_{0.3}Mn_{0.5}Co_2O_2$ are from -29 THz while the negative vibrations for fluorine doped $Ni_{0.3}Mn_{0.5}Co_2O_2$ are from -6 THz which indicate that doping with fluorine enhances the vibrations behaviour for $Ni_{0.3}Mn_{0.5}Co_2O_2$ system.

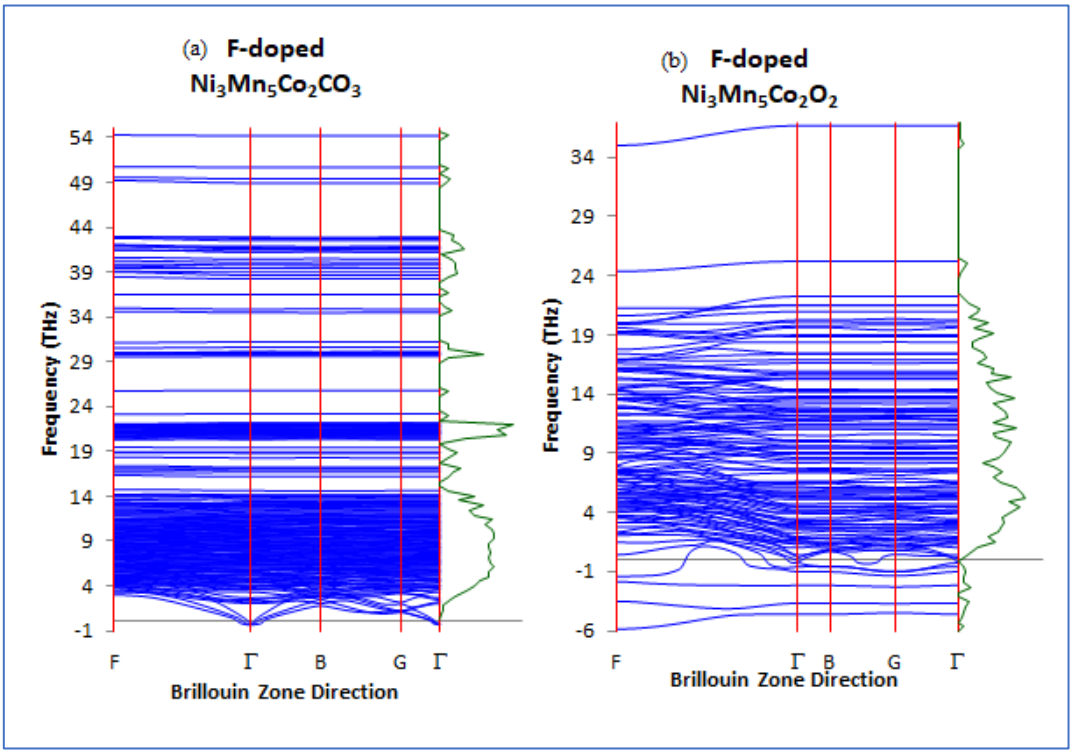

Figure 3-13. Phonon dispersion curves for doped systems (a) F-doped $Ni_{0.3}Mn_{0.5}Co_2CO_3$ and (b) F-doped $Ni_{0.3}Mn_{0.5}Co_3CO_3$.

Figure 3-14 display the phonon dispersion curve for Ti-doped $Ni_{0.3}Mn_{0.5}Co_2CO_3$ and Ti-doped $Ni_{0.3}Mn_{0.5}Co_2O_2$. We observe that the phonon dispersion curve for Ti-doped $Ni_{0.3}Mn_{0.5}Co_2CO_3$ shows no negative vibrations in the Brillouin zone direction which implies that the system is vibrationally stable. On the other hand, we observe that the phonon dispersion curve for Ti-doped $Ni_{0.3}Mn_{0.5}Co_2O_2$ is characterized by the soft modes or negative vibrations (-30 THz) at ambient pressure. These negative vibrations are along the Brillouin zone direction indicating

the vibrational instability. We also note that doping $Ni_{0.3}Mn_{0.5}Co_2O_2$ system with titanium in the manganese position slightly deteriorate its behaviour as the vibrations increases to (-30 THz) as compared to (-29 THz) of pure $Ni_{0.3}Mn_{0.5}Co_2O_2$ system.

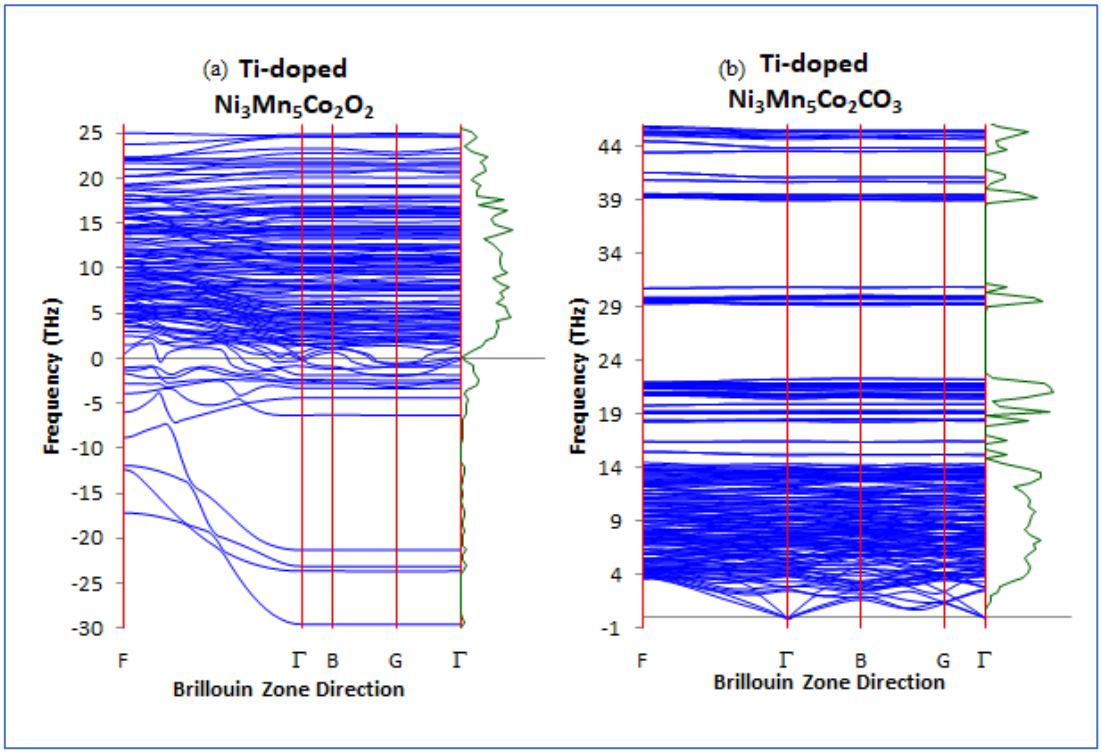

Figure 3-14. Phonon dispersion curves for (a) Ti-doped $Ni_{0.3}Mn_{0.5}Co_2CO_3$ and (b) Ti-doped $Ni_{0.3}Mn_{0.5}Co_2O_2$.

Figure 3-15 presents the phonon dispersion curves for Nb-doped $Ni_{0.3}Mn_{0.5}Co_2CO_3$ and Nb-doped $Ni_{0.3}Mn_{0.5}Co_2O_2$ at ambient pressure. Contrary to fluorine and titanium doped $Ni_{0.3}Mn_{0.5}Co_2CO_3$, the phonon dispersion curve for $Ni_{0.3}Mn_{0.5}Co_2CO_3$ doped with niobium at manganese positions is characterized by the negative vibrations or soft modes (-5 THz). These soft modes in the Brillouin zone direction indicate the vibrational instability of the material. This indicate that doping with niobium deteriorate the behaviour of $Ni_{0.3}Mn_{0.5}Co_2CO_3$ system. Similarly to fluorine and titanium doped $Ni_{0.3}Mn_{0.5}Co_2O_2$, the phonon dispersion curve for Nb-

doped $Ni_{0.3}Mn_{0.5}Co_2O_2$ at manganese position display the negative vibrations in the Brillouin zone direction (-28 THz) indicating vibrational instability of the material.

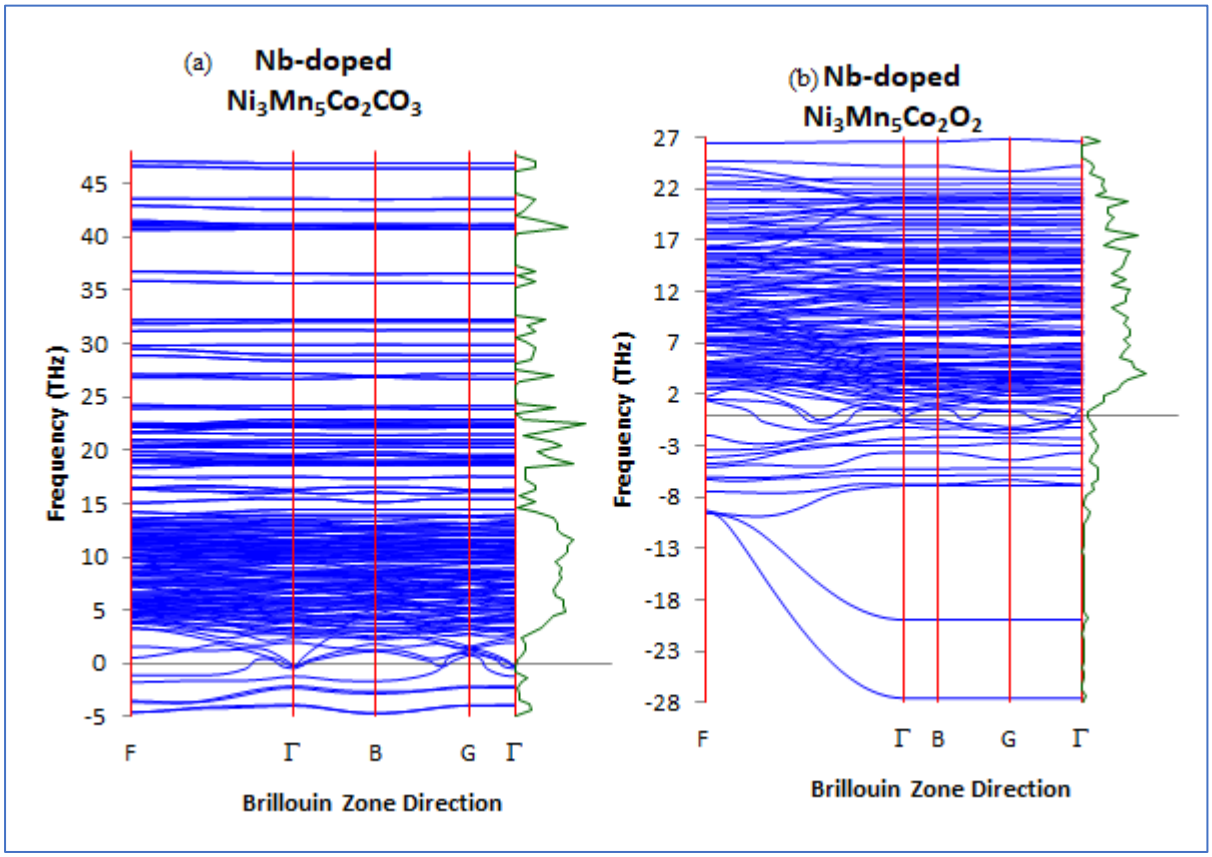

Figure 3-15. Phonon dispersion curves for (a) Nb-doped $Ni_{0.3}Mn_{0.5}Co_2CO_3$ and Nb-doped $Ni_{0.3}Mn_{0.5}Co_2O_2$.

Chapter 4
Cluster Expansion Technique

4.1. Introduction

A cluster expansion (CE) method is a popular and effective way for describing the thermodynamics and cooperative phenomena such as the order-disorder transitions of complex and multicomponent systems. Cluster expansion as a suitable computing technique, is a power series expansion of the partition function that Mayer introduced in 1941. Cluster expansion is frequently used as a bridge between first-principle calculations and Monte Carlo simulation, both of which try to estimate the material's properties. Since first-principle calculations can only be implemented with a small number of atoms per unit cell, DFT computations are particularly time-consuming and computationally intensive since they do not scale well with system size. The cluster expansion (CE) approach is the best appropriate energy model for the following reasons: a big system with hundreds or more atoms can have its energy estimated extremely quickly; By fitting to the energies of DFT calculations for a particular collection of tiny structures, it is possible to produce precise and transferable CE coefficients. This is especially useful for generating multi-component structures inside a random mixing.

4.2. Phase diagram for new generated systems

In this section, we discuss in detail the phase diagram obtained using the Universal cluster expansion technique. We initially searched for $MnCO_3$ structure in MediA software then added cobalt and nickel to the structure to form $NiMnCoCO_3$ structure which is commonly known as NMC's. The structures were generated following the genetic algorithm procedure and the effective cluster interactions were fitted by means of a genetic algorithm. Starting with an initial training set of 162 structures, the fitting scheme calculated a maximum of 20 iterations, adding

a maximum of 10 new structures per iteration. The iterations persisted until the CE could anticipate no more new structures.

Various structures with varied concentrations and symmetries were produced by the ground-state phase diagram. The iterations continue until all of the anticipated structure's energies which are higher than the estimated energies for the structures of the ground state line at each sampled concentration are determined by the cluster expansion. The information in Table 5-1, includes the number of iterations required to condense the ground state search, the number of existing ground state structures, the number of new structures that have been added to the ground state, the cross validation score used to determine how accurate DFT energy calculations will be and the list of new structures that have been generated per iteration. From the second iteration 0, 13 new structures generated are the initial structures in the training set randomly identified by the UNCLE code using genetic algorithm. The energies of the structures in the training set, or the structures created from iteration 1 through iteration 19, are used to identify the optimal set of new structures together with their accompanying interaction parameters. Whether the cluster expansion ground-state search has converged, it is determined using the most recent iteration whereby the final iteration (20) needs to produce no new structures (0). From our results shown in Table 4-1, it is revealed that at iteration 20, no new structures were generated, which indicate that our cluster expansion ground state search has converged. A statistical technique used to evaluate the dependability of the structure is cross-validation score. It is most frequently used for forecasting and determining how accurate a predicted structure will be in usage. From our results, the accuracy of the development of new structures during cluster expansion fitting is indicated by the cross validation score (CVs) for all of the generated new structures being less than 5meV per active atom position. Since all of

the developed structures have CVs below 5meV, this indicate that our calculations were valid and the new generated structures will work realistically.

Table 4-1. List of generated new structures from $NiCoMnCO_3$ system.

Iteration	Number Of structures	Number Of new structures	Cross validation score	% structure with SD below 5 meV	New structures
0	0	3	-	-	ce1 ce4 ce6
0	0	13	-	-	ce4361 ce162….
1	13	10	0.24	-	ce1216 ce2193…
2	22	10	0.22	-	ce332 ce5
3	32	10	1.1	-	ce36 ce5825
4	42	10	1.6	-	ce1018 ce4251
5	52	10	2	-	ce4801 ce4
6	61	10	2.4	-	ce487 ce119
7	67	10	2.8	-	ce1 ce3806
8	75	10	2.8	-	ce297 ce1430
9	84	10	2.7	-	ce6 ce2432
10	91	10	3	-	ce3 ce3410
11	99	10	3.1	-	ce2120 ce576
12	105	10	3.5	-	ce6 ce29
13	114	10	3.1	-	ce4603 ce5842
14	122	10	3.1	-	ce2405 ce107
15	129	10	3	-	ce140 ce594

16	137	10	4.6	-	ce193 ce2066
17	144	10	4.8	-	ce157 ce5
18	150	10	4.7	-	ce351 ce301
19	158	10	4.7	-	ce1470 ce393
20	162	0	4.5	-	ce1470 ce393

In computational material science, cluster expansion technique is used to predict the ordered or disordered superstructures. Figure 4-1 presents the phase diagram for $NiCoMnCO_3$ system which reveals critical information about the newly generated and predicted structures considered by the cluster expansion. The ground state search included all the possible stable configurations within a 42-atom system and managed to generate 162 new structures with various concentration and symmetries. We note that the grey crosses within the diagram indicate the cluster expansion predictions while the red line indicate DFT ground state line. All the structures found to be on the DFT ground state line are considered most stable as compared to other generated structures. We further note that all the predicted phases within the diagram are in the negative energy of formations side (miscible constituent) which indicate thermodynamic stability. The miscible constituent's behaviour indicate that structures are ordered and thermodynamically stable.

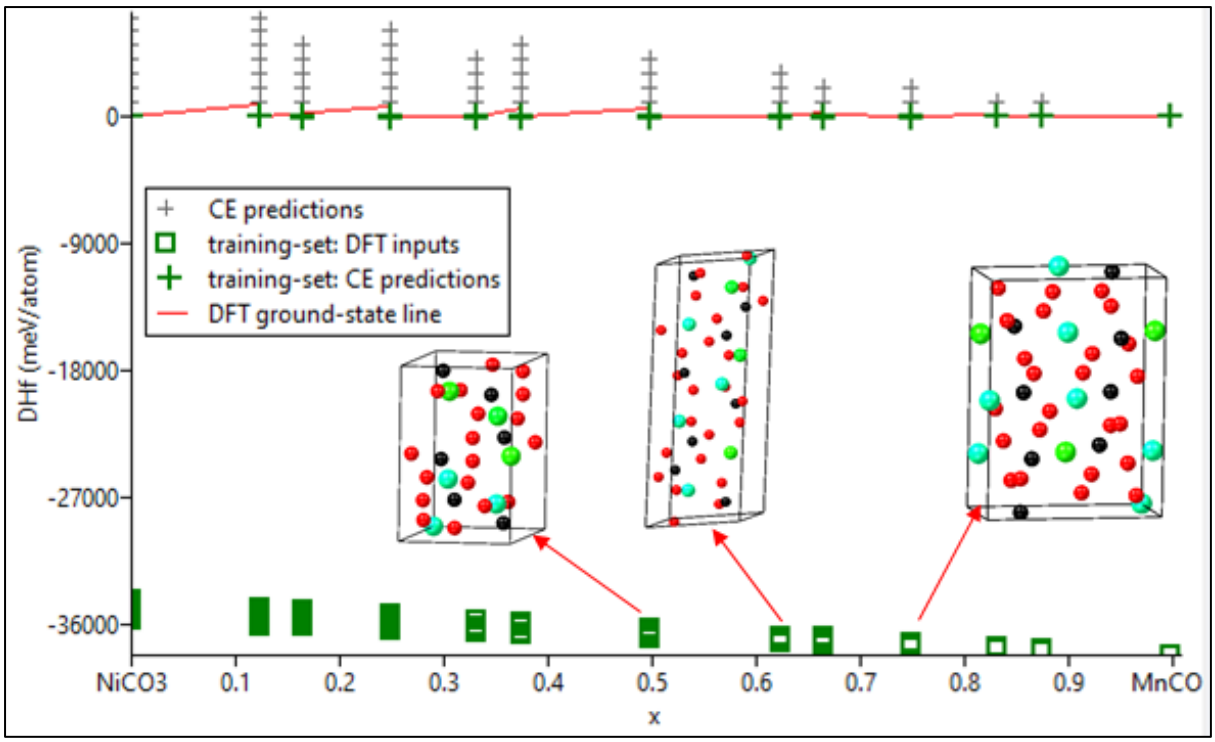

Figure 4-1. Phase diagram for $NiCoMnCO_3$ structure.

4.3. Manganese rich stable structures

In this section we further evaluate the most stable phases generated in Figure 4-1. In particular, we calculate their structural properties, electronic properties, mechanical properties and vibrational properties.

4.3.1. Structural properties

The role of various components in the overall structure is reflected in the structural properties of the material. In this section we analyse the structural properties in terms of lattice parameters, energy of formation, volume and density for the ternary phases generated from cluster expansion. Lattice parameters are one of the physical dimensions and angles that determines the geometry of the unit cells in a crystal lattice, and is proportional to the distance between atoms in the crystal. Table 4-2 depicts our calculated lattice parameters, volume, energy of

formation and density for $Ni_{0.3}Mn_{0.5}Co_{0.17}CO_3$, $Ni_{0.17}Mn_{0.67}Co_{0.17}CO_3$, $Ni_{0.13}Mn_{0.75}Co_{0.13}CO_3$, $Ni_{0.17}Mn_{0.84}Co_{0.17}CO_3$ and $Ni_{0.13}Mn_{0.87}Co_{0.13}CO_3$.

From our lattice parameters, we note that $a \neq b \neq c$ which indicate that all the generated phases are triclinic systems. The energy of formation was calculated to determine the thermodynamic stability of our phases. As shown in Table 4-2, it is clear that all the energy of formation values are negative, which indicate that these new generated phases are thermodynamically stable. The thermodynamic stability trend is as follows:

$$Ni_{0.13}Mn_{0.87}Co_{0.13}CO_3 > Ni_{0.13}Mn_{0.75}Co_{0.13}CO_3 > Ni_{0.17}Mn_{0.84}Co_{0.17}CO_3 >$$

$$Ni_{0.17}Mn_{0.67}Co_{0.17}CO_3 > Ni_{0.3}Mn_{0.5}Co_{0.17}CO_3.$$

Table 4-2. Lattice parameters, volume, density and energy of formation for $Ni_{0.3}Mn_{0.5}Co_{0.17}CO_3$, $Ni_{0.17}Mn_{0.67}Co_{0.17}CO_3$, $Ni_{0.13}Mn_{0.75}Co_{0.13}CO_3$, $Ni_{0.17}Mn_{0.84}Co_{0.17}CO_3$ and $Ni_{0.13}Mn_{0.87}Co_{0.13}CO_3$.

	$Ni_{0.3}Mn_{0.5}Co_{0.17}CO_3$	$Ni_{0.17}Mn_{0.67}Co_{0.17}CO_3$	$Ni_{0.13}Mn_{0.75}Co_{0.13}CO_3$	$Ni_{0.17}Mn_{0.84}Co_{0.17}CO_3$	$Ni_{0.13}Mn_{0.87}Co_{0.13}CO_3$
a (Å)	4,573	4,559	5,461	4,565	7,104
b (Å)	7,182	5,476	8,459	7,117	7,910
c (Å)	8,499	10,649	8,439	8,463	7,103
V ($Å^3$)	263,704	259,66	344,693	258,992	344,048
Density(mg/m^3)	4,415	4,460	4,467	4,446	4,456
ΔH_f (kJ/mol)	-4975.43	-5042.98	-6882.80	-5107.39	-7032.83

4.3.2. Electronic Band structures

Band structure is responsible for the explanation of the electrical properties of a material. The most important information that can be extracted from the electron band structure is the value of the energy gap. The electronic band structure is a representation of the allowed energies for

the electrons in the material. It shows how the energy levels of electrons in a solid material are arranged into bands, and how those bands are separated by gaps known as energy band gaps. In a solid material, electrons exist in one of two types of bands namely the valence and conduction bands. The valence band is the band that is occupied by electrons that are bound to the atoms in the material while the conduction band is the band that is empty or partially occupied by electrons that are free to move. The energy difference between the valence and conduction bands is known as the band gap. Figure 4-2 and 4-3 shows the energy band structures for all new generated phases in the Mn-rich side which were plotted in the first Brillouin zone with respect to the energy (eV). The bands below the zero line is the valence bands while bands above the zero line are conduction bands. These two bands are separated by the Fermi line which acts as the zero line. The distance between the states at the valence band maxima (VBM) and the conduction band minima (CBM) is determined by the electronic energy band gap.

Figure 4-2 shows the energy band structures for $Ni_{0.3}Mn_{0.5}Co_{0.17}CO_3$, $Ni_{0.17}Mn_{0.67}Co_{0.17}CO_3$, $Ni_{0.13}Mn_{0.75}Co_{0.13}CO_3$ at ambient temperature and pressure. The band structure for $Ni_{0.3}Mn_{0.5}Co_{0.17}CO_3$ shows the metallic characteristic since the conduction bands overlap to the valence bands at the Fermi line, this behaviour suggests that $Ni_{0.3}Mn_{0.5}Co_{0.17}CO_3$ have good electronic conductivity. On the other hand, band structure for $Ni_{0.17}Mn_{0.67}Co_{0.17}CO_3$, $Ni_{0.13}Mn_{0.75}Co_{0.13}CO_3$ behave in the same manner whereby both systems have half metallic ferromagnetic characteristic. The half metallic ferromagnetic behaviour simply means that bands for one spin are metallic while bands for other pin are semiconducting. Similarly to $Ni_{0.17}Mn_{0.67}Co_{0.17}CO_3$ and $Ni_{0.13}Mn_{0.75}Co_{0.13}CO_3$, band structures for $Ni_{0.17}Mn_{0.84}Co_{0.17}CO_3$ and $Ni_{0.13}Mn_{0.87}Co_{0.13}CO_3$ shown in Fig 4-3 also have the half metallic ferromagnetic behaviour. This indicate that $Ni_{0.17}Mn_{0.67}Co_{0.17}CO_3$, $Ni_{0.13}Mn_{0.75}Co_{0.13}CO_3$,

$Ni_{0.17}Mn_{0.84}Co_{0.17}CO_3$ and $Ni_{0.13}Mn_{0.87}Co_{0.13}CO_3$ systems can act either as a semiconductor or as a metallic.

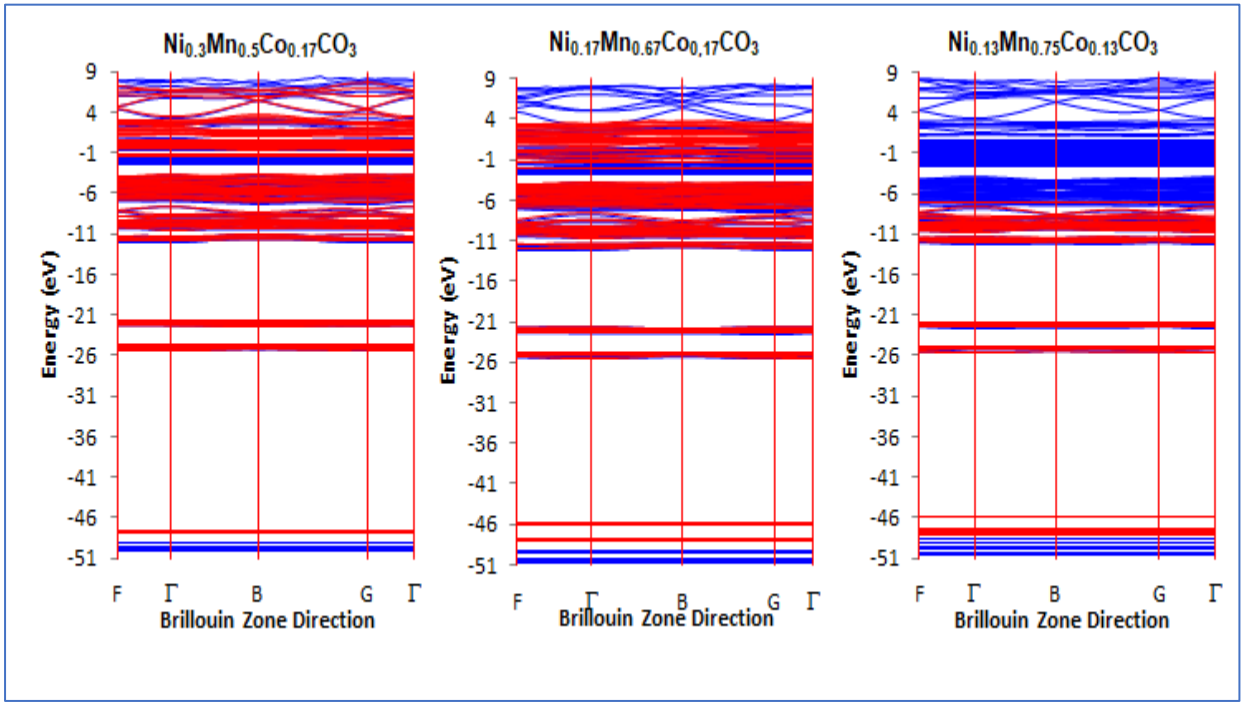

Figure 4-2. Electronic band structures for $Ni_{0.3}Mn_{0.5}Co_{0.17}CO_3$, $Ni_{0.17}Mn_{0.67}Co_{0.17}CO_3$ and $Ni_{0.13}Mn_{0.75}Co_{0.13}CO_3$.

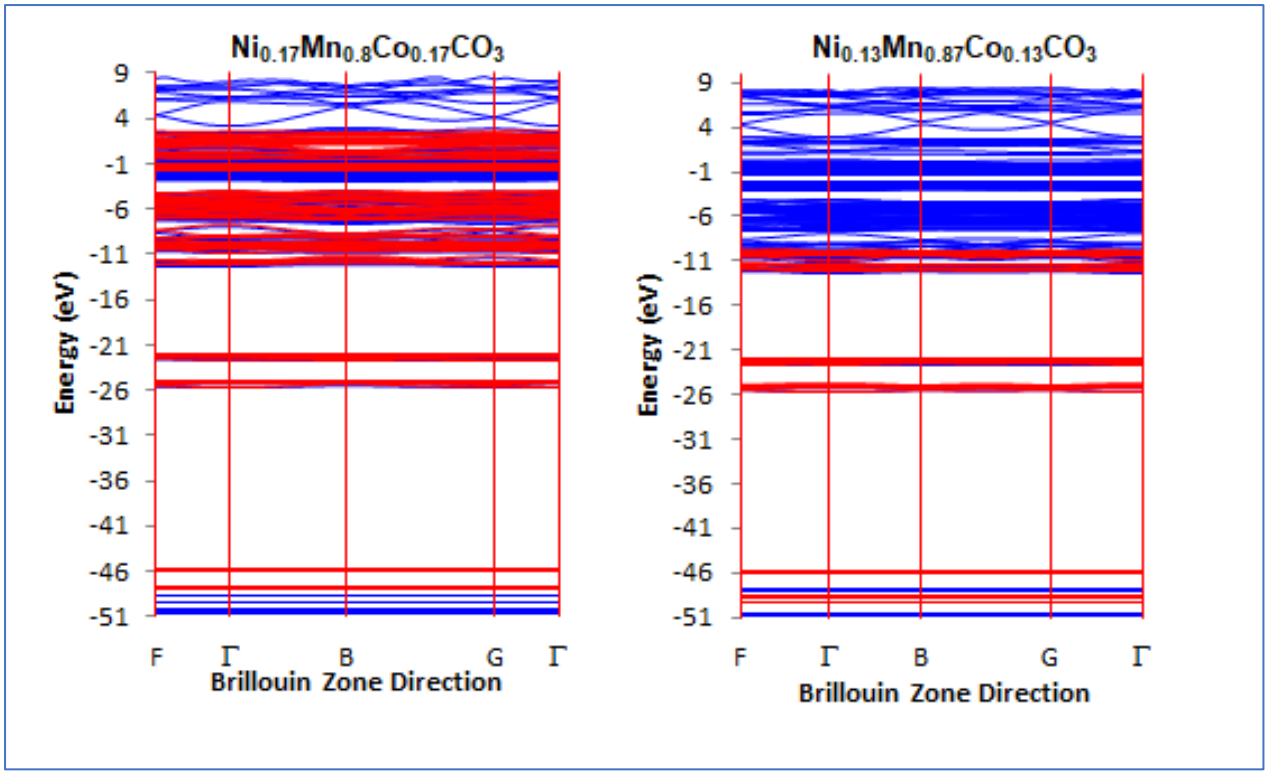

Figure 4-3. Electronic band structures for $Ni_{0.17}Mn_{0.84}Co_{0.17}CO_3$ and $Ni_{0.13}Mn_{0.87}Co_{0.13}CO_3$.

4.3.3. Density of states

Figure 4-4 and 4-5 show the total density of states (DOS) of $Ni_{0.3}Mn_{0.5}Co_{0.17}CO_3$ $Ni_{0.17}Mn_{0.67}Co_{0.17}CO_3$,$Ni_{0.13}Mn_{0.75}Co_{0.13}CO_3$,$Ni_{0.17}Mn_{0.84}Co_{0.17}CO_3$ and $Ni_{0.13}Mn_{0.87}Co_{0.13}CO_3$ phases. The DOS calculations were computed using the spin polarised local density approximation with Hubbard corrections (LDA+U). The high spin states are displayed on the positive scale while the lower spin states are seen on the negative scale. Figure 4-4 shows the density of states for $Ni_{0.3}Mn_{0.5}Co_{0.17}CO_3$ and $Ni_{0.17}Mn_{0.67}Co_{0.17}CO_3$ respectively. For $Ni_{0.3}Mn_{0.5}Co_{0.17}CO_3$, we note the pressence of pseudogap and that the Fermi level lies on the right of the pseudogap. The existence of pseudogap suggests that $Ni_{0.3}Mn_{0.5}Co_{0.17}CO_3$ has a metallic behaviour characteristics. Pseudogap also shows the relative overlap of electrons from the valence to the conduction band. This corresponds well with the heats of formation which

suggested thermodynamic stability of $Ni_{0.3}Mn_{0.5}Co_{0.17}CO_3$. On the other hand, the total density of states for $Ni_{0.17}Mn_{0.67}Co_{0.17}CO_3$ shows that the electronic states at the spin-up chanel of nickel, managnese, cobalt, carbon and oxygen atoms are seen overlapping at the fermi line depicting metallic behavior. While the spin down channel shows semiconductor behavior due to an observed energy band gap between the electronic states atoms. These conditions indicate that $Ni_{0.17}Mn_{0.67}Co_{0.17}CO_3$ is a half metallic ferromagnet, since it can acts as a semiconductor or metallic.

Figure 4-5 shows the total density of states for $Ni_{0.13}Mn_{0.75}Co_{0.13}CO_3$, $Ni_{0.17}Mn_{0.84}Co_{0.17}CO_3$ and $Ni_{0.13}Mn_{0.87}Co_{0.13}CO_3$ systems. Similarly to $Ni_{0.17}Mn_{0.67}Co_{0.17}CO_3$, we note that all the have the half metallic ferromagnetic behaviour. For $Ni_{0.13}Mn_{0.75}Co_{0.13}CO_3$, we note that the spin-up bands are semiconducting while the spin-down bands are metallic. We also observe the same behaviour for $Ni_{0.17}Mn_{0.84}Co_{0.17}CO_3$, as bands for spin-up channels are semiconducting while bands for spin down are metallic. Contrary to $Ni_{0.13}Mn_{0.87}Co_{0.13}CO_3$, bands for spin up are metallic while bands for spin down are semiconducting.

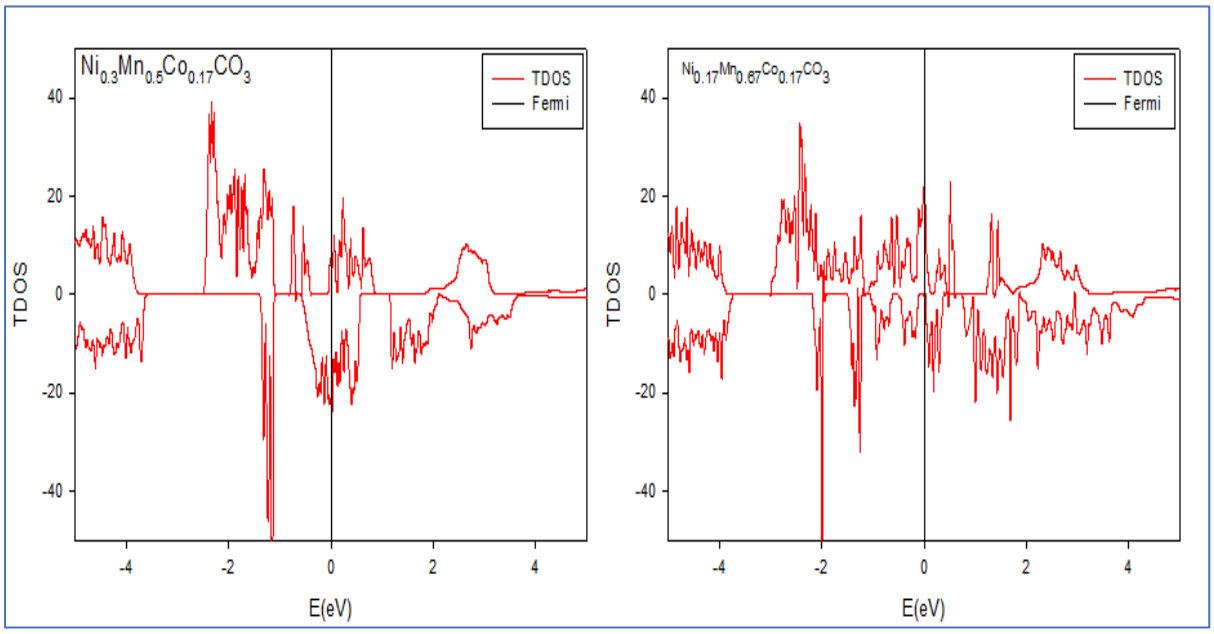

Figure 4-4. . Total density of states for $Ni_{0.3}Mn_{0.5}Co_{0.17}CO_3$ and $Ni_{0.17}Mn_{0.67}Co_{0.17}CO_3$.

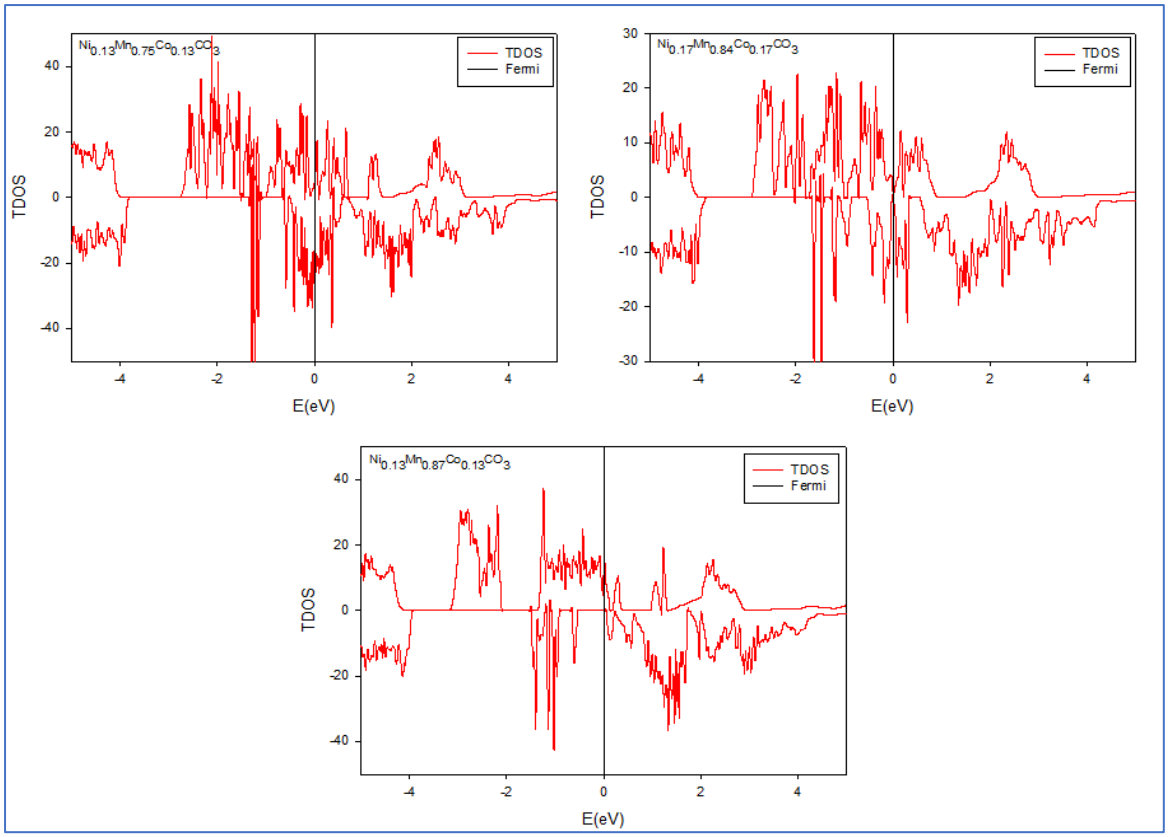

Figure 4-5. Total density of states for $Ni_{0.13}Mn_{0.75}Co_{0.13}CO_3$, $Ni_{0.17}Mn_{0.84}Co_{0.17}CO_3$ and $Ni_{0.13}Mn_{0.87}Co_{0.13}CO_3$.

4.3.4. Elastic Properties

This section is aimed at providing a better understanding of the mechanical compatibility for all the phases in the Mn-rich side. Elastic constants play an important role in understanding various mechanical and physical properties of materials. For example, the ratio of the bulk and shear modulus can depict the degree of ductility or brittleness of a material while the difference in the elastic stiffness coefficients can explain the nature of bonding in the system and the mechanical stability of the material. On the other hand, elastic anisotropy of a material can be related to the dielectric breakdown and anisotropy of the material, the Young‘s modulus of the material correlates to the degree of stiffness in the material while the shear and bulk modulus of a material can be correlated to its hardness and fracture stress.

Table 4-3 to 4-4 lists the DFT results on elastic constants (C_{ij}) of $Ni_{0.3}Mn_{0.5}Co_{0.17}CO_3$, $Ni_{0.17}Mn_{0.67}Co_{0.17}CO_3$, $Ni_{0.13}Mn_{0.75}Co_{0.13}CO_3$, $Ni_{0.17}Mn_{0.8}Co_{0.17}CO_3$ and $Ni_{0.13}Mn_{0.87}Co_{0.13}CO_3$ phases respectively. Since all the phases generated fall within the triclinic crystal system, 21 independent elastic constants were obtained. For triclinic crystal systems to be considered mechanically stable, the following necessary and sufficient Born stability conditions must be satisfied [134, 135].

$$C_{11} > 0, C_{22} > 0, C_{33} > 0, C_{44} > 0, C_{55} > 0, C_{66} > 0.$$

We note that $Ni_{0.3}Mn_{0.5}Co_{0.17}CO_3$ does not satisfy the $C_{33} > 0$ condition while $Ni_{0.13}Mn_{0.75}Co_{0.13}CO_3$ does not satisfy the $C_{11} > 0\ and\ C_{22} > 0$ conditions, implying that both these systems are mechanically unstable. On the other hand, $Ni_{0.17}Mn_{0.67}Co_{0.17}CO_3$, $Ni_{0.17}Mn_{0.8}Co_{0.17}CO_3$ and $Ni_{0.13}Mn_{0.87}Co_{0.13}CO_3$ phases were found to satisfy the triclinic stability conditions which indicate mechanical stability. We further calculated the Moduli, Pugh ratio and anisotropy for all the generated phases in the Mn-rich side and their results are presented in Table 3-5 and 3-6. From our results we note that $Ni_{0.13}Mn_{0.75}Co_{0.13}CO_3$ system possesses highest hardness over $Ni_{0.13}Mn_{0.87}Co_{0.13}CO_3$, $Ni_{0.17}Mn_{0.8}Co_{0.17}CO_3$, $Ni_{0.17}Mn_{0.67}Co_{0.17}CO_3$ and $Ni_{0.3}Mn_{0.5}Co_{0.17}CO_3$ respectively due to its largest value of the bulk modulus. We note that $Ni_{0.3}Mn_{0.5}Co_{0.17}CO_3$ system has highest shear modulus value (71.45 GPa), indicating highest resistance over other phases. It is noteworthy that the shear modulus of $Ni_{0.3}Mn_{0.5}Co_{0.17}CO_3$ is higher than the bulk modulus. This indicates that $Ni_{0.3}Mn_{0.5}Co_{0.17}CO_3$ is more brittle than hard and resistant to deformation, making it more susceptible to cracking when put under strain. In the other systems, the bulk is larger than the shear, indicating that the stability-limiting parameter is the shear modulus. Furthermore, Pugh's ratio suggests brittleness if (B/G<1.75) and ductility if (B/G>1.75). Hence, $Ni_{0.3}Mn_{0.5}Co_{0.17}CO_3$ and

$Ni_{0.13}Mn_{0.75}Co_{0.13}CO_3$ shows the Pugh ratio being < 1.75 which depicts brittleness while $Ni_{0.17}Mn_{0.67}Co_{0.17}CO_3$, $Ni_{0.17}Mn_{0.8}Co_{0.17}CO_3$ and $Ni_{0.13}Mn_{0.87}Co_{0.13}CO_3$ depicts ductility.

Table 4-3. Calculated elastic Constants for $Ni_{0.3}Mn_{0.5}Co_{0.17}CO_3$, $Ni_{0.17}Mn_{0.67}Co_{0.17}CO_3$ and $Ni_{0.13}Mn_{0.75}Co_{0.13}CO_3$.

C_{ij}	$Ni_{0.3}Mn_{0.5}Co_{0.17}CO_3$	$Ni_{0.17}Mn_{0.67}Co_{0.17}CO_3$	$Ni_{0.13}Mn_{0.75}Co_{0.13}CO_3$
C_{11}	343.88	327.47	-394.67
C_{12}	153.80	150.25	-623.20
C_{13}	-330.05	137.82	44.70
C_{14}	-174.55	33.39	479.37
C_{15}	0.65	-4.72	-496.08
C_{16}	219.42	-2.14	99.41
C_{22}	311.94	332.67	-454.11
C_{23}	-336.81	139.98	-10.09
C_{24}	-240.52	-38.97	325.75
C_{25}	0.87	-5.27	-401.10
C_{26}	217.21	1.01	135.30
C_{33}	-562.79	189.30	504.18
C_{34}	-173.54	-0.71	325.56
C_{35}	-10.13	-4.24	-341.60
C_{36}	157.63	-1.19	105.90
C_{44}	39.77	70.50	99.36
C_{45}	-1.00	-1.20	-32.46
C_{46}	12.07	-1.28	27.79
C_{55}	66.99	73.00	104.69
C_{56}	30.67	39.90	64.26
C_{66}	78.94	92.98	49.25

Table 4-4. Calculated elastic constants for $Ni_{0.17}Mn_{0.8}Co_{0.17}CO_3$ and $Ni_{0.13}Mn_{0.87}Co_{0.13}CO_3$.

C_{ij}	$Ni_{0.17}Mn_{0.8}Co_{0.17}CO_3$	$Ni_{0.13}Mn_{0.87}Co_{0.13}CO_3$
C_{11}	356.25	366.28
C_{12}	204.19	198.05
C_{13}	162.66	180.09
C_{14}	32.89	44.75
C_{15}	9.47	-4.85
C_{16}	8.41	-2.93
C_{22}	375.83	360.17
C_{23}	171.43	175.53
C_{24}	-39.59	-40.57
C_{25}	15.21	-0.47
C_{26}	7.48	-2.13
C_{33}	209.44	216.18
C_{34}	-5.97	0.27
C_{35}	11.30	-0.95
C_{36}	6.77	-0.19
C_{44}	70.33	70.65
C_{45}	-1.16	-0.50
C_{46}	-1.66	1.28
C_{55}	70.74	69.59
C_{56}	38.58	41.86
C_{66}	92.81	79.98

Table 4-5. Moduli, Pugh ratio and Anisotropy for $Ni_{0.3}Mn_{0.5}Co_{0.17}CO_3$, $Ni_{0.17}Mn_{0.67}Co_{0.17}CO_3$ and $Ni_{0.13}Mn_{0.75}Co_{0.13}CO_3$.

(GPa)	$Ni_{0.3}Mn_{0.5}Co_{0.17}CO_3$	$Ni_{0.17}Mn_{0.67}Co_{0.17}CO_3$	$Ni_{0.13}Mn_{0.75}Co_{0.13}CO_3$
B	-1571.88	180.86	1552.71
G	71.45	66.88	-23.98
E	253.68	178.52	-58.72
$\frac{B}{G}$	-22.00	2.7	-64.75

Table 4-6. Moduli, Pugh ratio and Anisotropy for $Ni_{0.17}Mn_{0.8}Co_{0.17}CO_3$ and $Ni_{0.13}Mn_{0.87}Co_{0.13}CO_3$.

(GPa)	$Ni_{0.17}Mn_{0.8}Co_{0.17}CO_3$	$Ni_{0.13}Mn_{0.87}Co_{0.13}CO_3$
B	210.08	216.72
G	65.16	59.73
E	177.09	163.94
$\frac{B}{G}$	3.22	3.63

4.3.5. Phonon dispersion curves

The study of lattice vibration is crucial to understand how the energy is absorbed in the solids. In this section we discuss the phonon dispersion curves of new generated phases in the manganese rich side. In particular we determine the phonon dispersion curves for $Ni_{0.3}Mn_{0.5}Co_{0.17}CO_3$, $Ni_{0.17}Mn_{0.67}Co_{0.17}CO_3$, $Ni_{0.13}Mn_{0.75}Co_{0.13}CO_3$, $Ni_{0.17}Mn_{0.8}Co_{0.17}CO_3$ and $Ni_{0.13}Mn_{0.87}Co_{0.13}CO_3$. There are two different types of phonons within the propagation wave namely the upper branch (optical branch) and the lower branch (acoustical branch). For the optical branch, the two atoms in the unit cell move opposite to each other and the light mass

amplitude is greater whereas for acoustical branch, the displacement of both atoms has the same amplitude, direction and phase. Phonon dispersion curves were calculated using the PHONON code as discussed in detail in section 2.5. To the best of our knowledge, phonon dispersion curves on $Ni_{0.3}Mn_{0.5}Co_{0.17}CO_3$, $Ni_{0.17}Mn_{0.67}Co_{0.17}CO_3$, $Ni_{0.13}Mn_{0.75}Co_{0.13}CO_3$, $Ni_{0.17}Mn_{0.8}Co_{0.17}CO_3$ and $Ni_{0.13}Mn_{0.87}Co_{0.13}CO_3$ structures have never been investigated elsewhere, hence these results will be used for benchmarking in the future.

Figure 4-6 presents the phonon dispersion curves for (a) $Ni_{0.3}Mn_{0.5}Co_{0.17}CO_3$, (b) $Ni_{0.17}Mn_{0.67}Co_{0.17}CO_3$ and (c) $Ni_{0.13}Mn_{0.75}Co_{0.13}CO_3$.We note that the phonon dispersion curve for $Ni_{0.3}Mn_{0.5}Co_{0.17}CO_3$ and $Ni_{0.17}Mn_{0.67}Co_{0.17}CO_3$ shows positive frequencies in the high Brillouin zone which implies vibrational stability. Moreover, contrary to $Ni_{0.3}Mn_{0.5}Co_{0.17}CO_3$ and $Ni_{0.17}Mn_{0.67}Co_{0.17}CO_3$, the phonon dispersion curve for $Ni_{0.13}Mn_{0.75}Co_{0.13}CO_3$ display negative frequency phonon branches (here referred to as soft modes) down to -4 THz. These soft modes are observed along high symmetry directions in the Brillouin zone. The presence of soft modes suggests that the $Ni_{0.13}Mn_{0.75}Co_{0.13}CO_3$ structure is vibrationally unstable. Furthermore, Figure 4-7 present the phonon dispersion curves for $Ni_{0.17}Mn_{0.84}Co_{0.17}CO_3$ and $Ni_{0.13}Mn_{0.87}Co_{0.13}CO_3$. It is clearly seen that there exists no soft modes (only imaginary modes, induced by not imposing the invariant conditions in the PHONON Code) along high symmetry lines at ambient pressure for $Ni_{0.17}Mn_{0.84}Co_{0.17}CO_3$ structure. This particularly indicates that $Ni_{0.17}Mn_{0.84}Co_{0.17}CO_3$ is vibrationally stable. Furthermore, the phonon dispersion curve for $Ni_{0.13}Mn_{0.87}Co_{0.13}CO_3$ shows bands to appear in both the negative and positive frequencies. This implies that $Ni_{0.13}Mn_{0.87}Co_{0.13}CO_3$ structure is vibrationally unstable due to the availability of soft modes in the high Brillouin zone direction.

In addition to the phonon dispersion curves, we have calculated the phonon density of states for the completeness of lattice dynamics. Figure 4-8 presents the total and partial phonon density of states for $Ni_{0.13}Mn_{0.75}Co_{0.13}CO_3$ and $Ni_{0.13}Mn_{0.87}Co_{0.13}CO_3$ respectively. We observe relatively high density of states for Mn, Ni and Co atoms below 10 THz, whereas for C and O atoms high densities of states are dominant above 20 THz. This suggests that Mn, Ni and Co atoms vibrate in modes of the same low frequencies, while C and O atoms vibrate in modes of high frequencies. Moreover, we also note that Mn, Ni and Co atoms show density of states below 0 THz, suggesting that these atoms are responsible for the negative acoustic modes in the phonon dispersion curves for both $Ni_{0.13}Mn_{0.75}Co_{0.13}CO_3$ and $Ni_{0.13}Mn_{0.87}Co_{0.13}CO_3$ respectively.

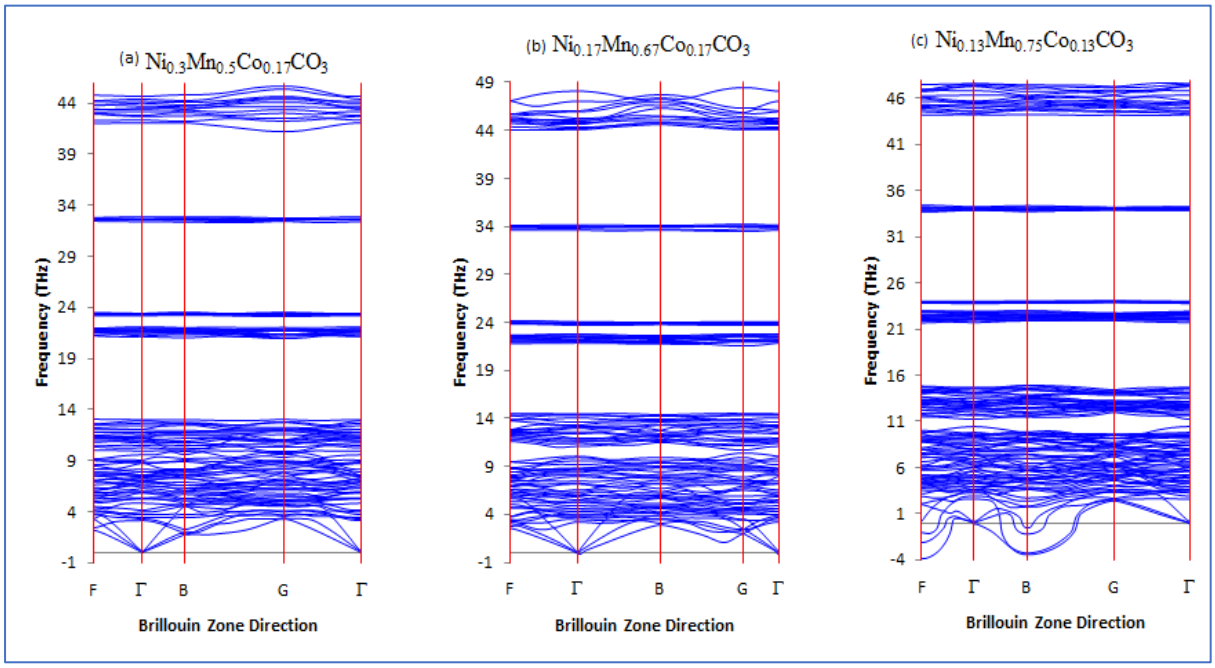

Figure 4-6. Phonon dispersion curves for (a) $Ni_{0.3}Mn_{0.5}Co_{0.17}CO_3$, (b) $Ni_{0.17}Mn_{0.67}Co_{0.17}CO_3$ and (c) $Ni_{0.13}Mn_{0.75}Co_{0.13}CO_3$.

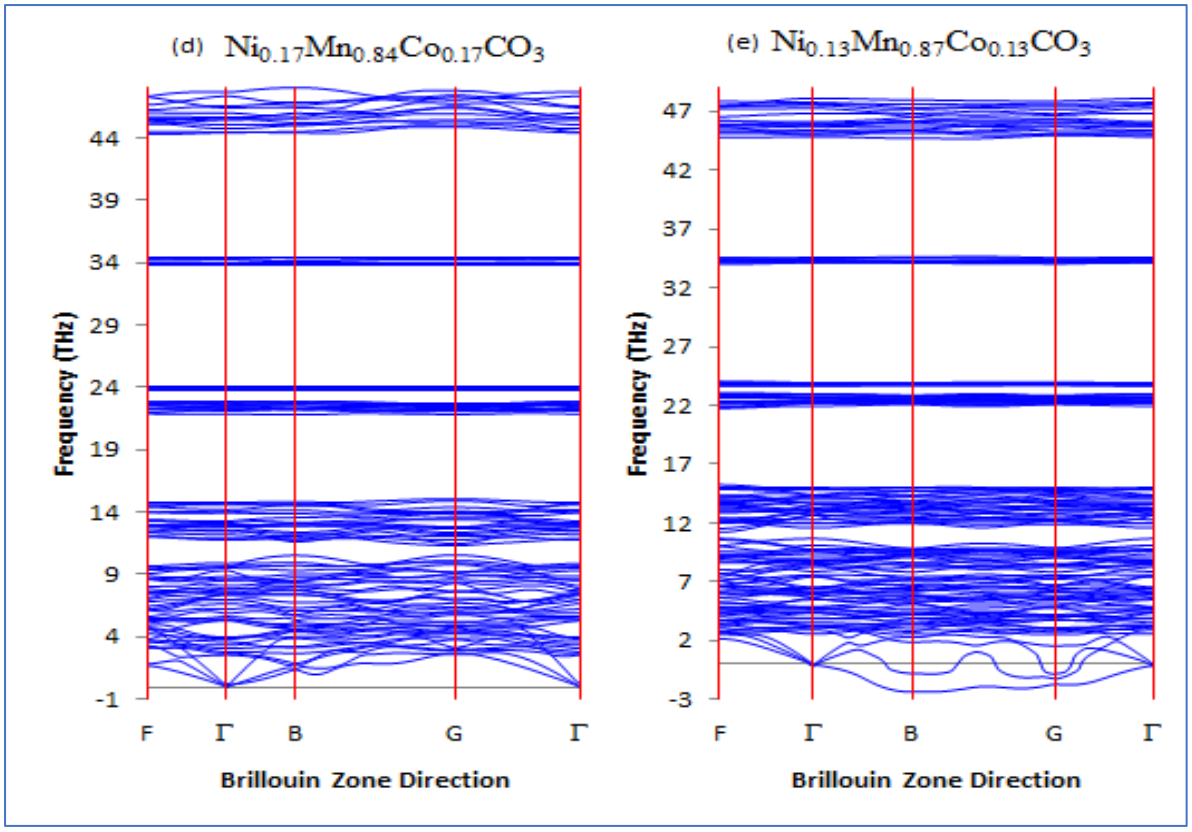

Figure 4-7. Phonon dispersion curves for (d) $Ni_{0.17}Mn_{0.84}Co_{0.17}CO_3$ and (e) $Ni_{0.13}Mn_{0.87}Co_{0.13}CO_3$.

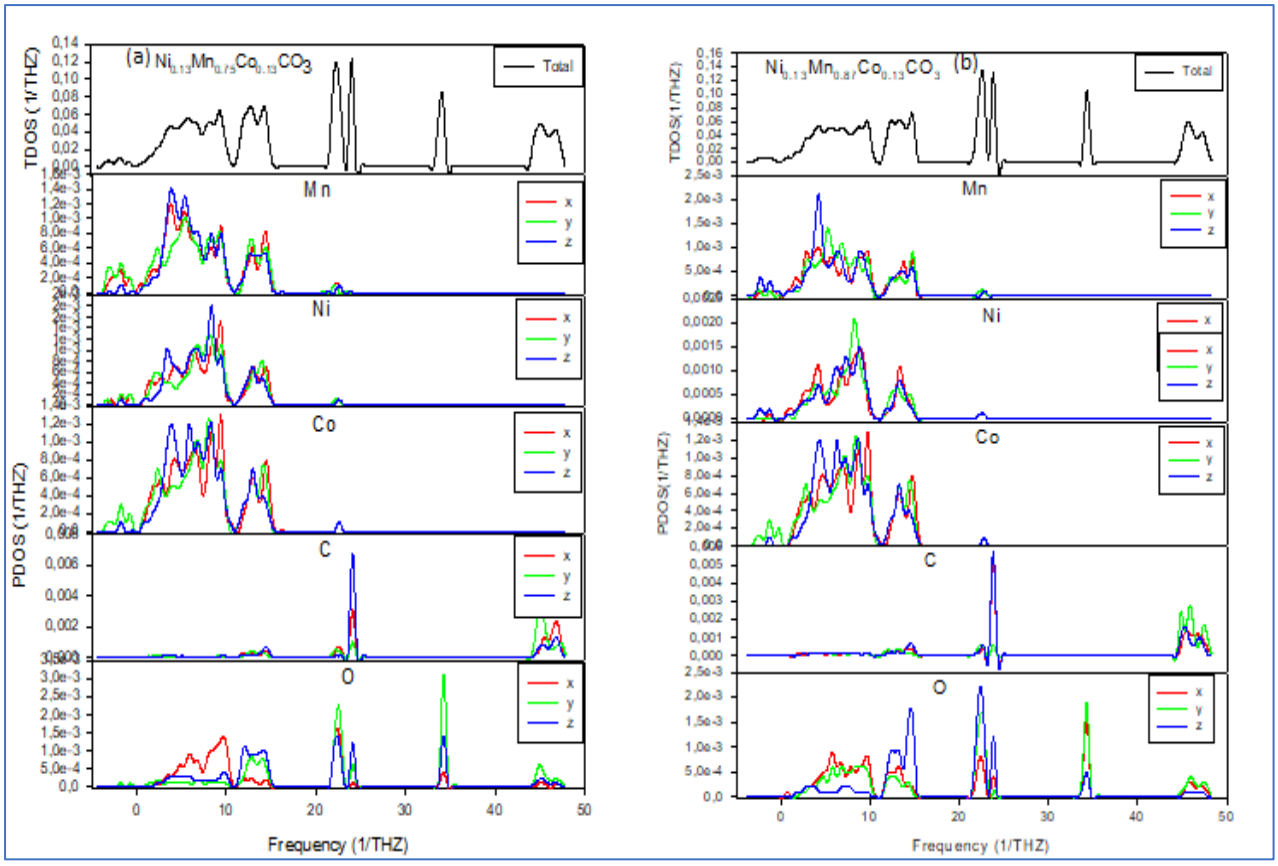

Figure 4-8. Phonon density of states for (a) $Ni_{0.13}Mn_{0.75}Co_{0.13}CO_3$ and (b) $Ni_{0.13}Mn_{0.87}Co_{0.13}CO_3$.

4.4. Ternary phase diagram for $NiMnCoCO_3$

A ternary phase diagram is a graphical representation of the phases that exist in a three-component system at various combinations of temperature, pressure, and composition. This type of diagram is commonly used to understand the behaviour of systems with three components. Ternary phase diagrams are valuable tools for predicting the behaviour of complex systems, helping researchers understand how different compositions and environmental conditions affect the phases present in the system. In our case we doped $MnCO_3$ structure with $NiCO_3$ and $CoCO_3$ to produce $NiMnCoCO_3$ commonly known as NMC's. In a ternary phase diagram, the three components are typically represented at the vertices of an equilateral triangle. Each corner of the triangle corresponds to one of the pure components ($NiCO_3$, $MnCO_3$, and $CoCO_3$). The composition of a point within the triangle is expressed as a

percentage of each component, and the entire triangle represents all possible phases generated from the three parent structures. Lines connecting the corners of the triangle represent binary compositions (mixtures of two components).

Figure 4-6, shows the ternary phase diagram for $NiCO_3$, $MnCO_3$, and $CoCO_3$. From the figure we note that the blue crosses represents the cluster expansion grid while the green dots represents the phases on the DFT ground states. We also note that binary compositions appears from $MnCO_3$ to $NiCO_3$, $NiCO_3$ to $CoCO_3$ and $CoCO_3$ to $MnCO_3$, while the ternary compositions appears in the middle of the phase diagram. Our cluster expansion managed to generate seven ternary phases which are all thermodynamically stable. The thermodynamic stability notion is clearly elaborated in Fig 4-7 which shows that all the phases generated (both binary and ternary) are in the negative energy of formation implying thermodynamic stability with various colours to specify which phases are more thermodynamically stable than others. Furthermore, Table 4-7 to 4-10 indicate the formula and space groups for all the newly generated phases. However, the most crucial phases for this study are the ternary phases and their compositions are as follows:

$Ni_{0.5}Mn_{0.2}Co_{0.3}CO_3$, $Ni_{0.5}Mn_{0.3}Co_{0.3}CO_3$, $Ni_{0.5}Mn_{0.3}Co_{0.2}CO_3$, $Ni_{0.3}Mn_{0.2}Co_{0.5}CO_3$, $Ni_{0.3}Mn_{0.3}Co_{0.5}CO_3$, $Ni_{0.2}Mn_{0.2}Co_{0.7}CO_3$ and $Ni_{0.2}Mn_{0.3}Co_{0.5}CO_3$. From compositions shown above we note that no manganese rich composition was generated as per our expectations, instead the nickel rich and cobalt rich phases were generated. The layered nickel rich oxides as cathodes for lithium ion batteries have been studied extensively by researchers due to their high discharge capacity of (200–220 mAh g −1) [145], which represents a large increase in energy density as compared to other materials.

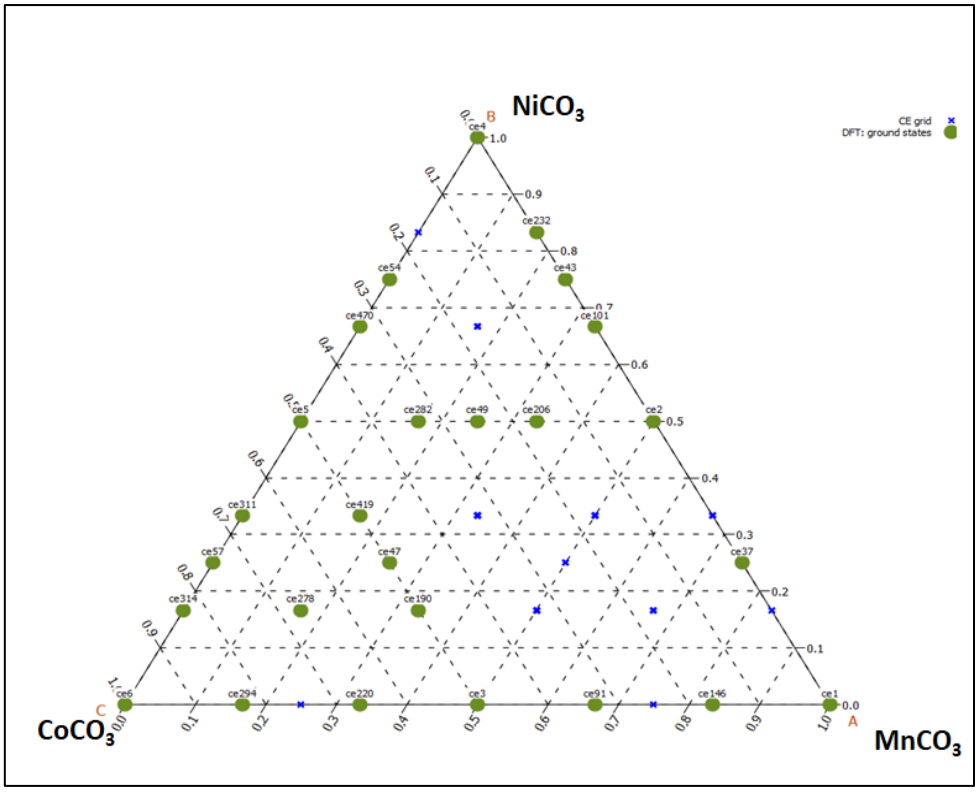

Figure 4-9. Ternary phase diagram for $NiCO_3$, $MnCO_3$ and $CoCO_3$.

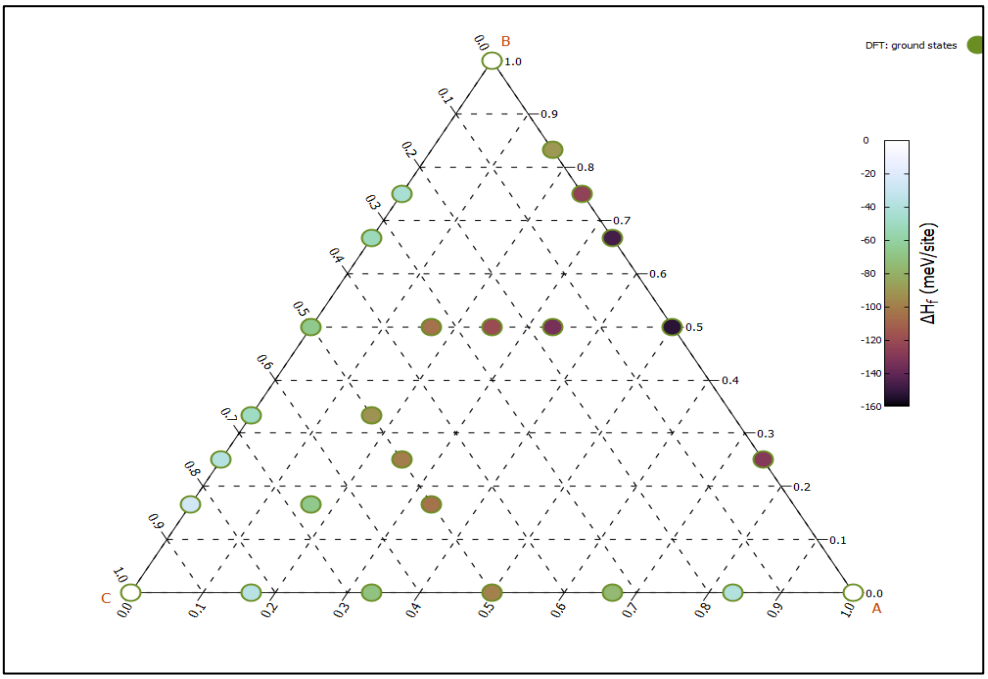

Figure 4-10. Energy of formation diagram for all the generated phases.

Table 4-7. Generated phases from $MnCO_3$ to $NiCO_3$.

Phases from $MnCO_3$ to $NiCO_3$	Space group
$MnNi_5C_6O_{18}$	P-1
$MnNi_3C_4O_{12}$	P-1
$Mn_2Ni_4C_6O_{18}$	C2/c
$MnNiC_2O_6$	-R3
$Mn_3NiC_4O1_2$	P-1

Table 4-8. Generated phases from $NiCO_3$ to $CoCO_3$.

Phases from $NiCO_3$ to $CoCO_3$	Space group
$CoNi_3C_4O_{12}$	P-1
$Co_2Ni_4C_6O_{18}$	P-1
$CoNiC_2O_6$	-R3
$Co_4Ni_2C_6O_{18}$	P-3c1
$Co_3NiC_4O_{12}$	P-1
$Co_5NiC_6O_{18}$	P-1

Table 4-9. Generated phases from $CoCO_3$ to $MnCO_3$.

Phases from $CoCO_3$ to $MnCO_3$	Space group
$MnCo_5C_6O_{18}$	P-1
$Mn_2Co_4C_6O_{18}$	P-1
$MnCoC_2O_6$	-R3

$Mn_4Co_2C_6O_{18}$	C2/c
$Mn_5CoC_6O_{18}$	P-1

Table 4-10. Ternary phases generated from mixing $MnCO_3$, $NiCO_3$ and $CoCO_3$.

Phases from $NiCO_3$, $CoCO_3$ and $MnCO_3$	Space group
$MnCo_2Ni_3C_6O_{18}$	P-1
$MnCoNi_2C_4O_{12}$	P-1
$Mn_2CoNi_3C_6O_{18}$	P-1
$MnCo_3Ni_2C_6O_{18}$	P-1
$MnCo_2NiC_4O_{12}$	P-1
$MnCo_4NiC_6O_{18}$	P-1
$Mn_2Co_3NiC_6O_{18}$	P-1

Chapter 5
Experimental Results

The synthesis process of battery cathodes such as NMC's has evolved over the past years. These NMC's are synthesized using the co-precipitation methods which are widely used in various applications. Co-precipitation has gained interest in the last 10-15 years especially for $LiNi_xMn_yCo_{1-x-y}O_2$ cathode materials due to its simplicity, better particle morphology control and the homogeneous mixing at the atomic scale. In this chapter we discuss in detail the experimental results for lithiated layered structures with various compositions.

5.1. Thermogravimetric analyses (TGA)

Thermal analysis is an important analytical tool used to study the properties of materials as the temperature is changed. TGA can be used to measure changes in the mass of material as a function of time either at a selected temperature (i.e. isothermal mode) or over a particular temperature range using a predetermined heating rate under a controlled atmosphere. This technique is widely used to monitor thermal stability and the loss of volatile components for materials where a loss of mass occurs because of thermal degradation or desolvation. In this study, TGA was utilized to investigate the thermal stability and decomposition behaviours of materials used in the battery electrodes, such as nickel manganese cobalt oxide (NMC) cathodes.

The thermal decomposition profiles for $LiNi_{0.33}Mn_{0.53}Co_{0.14}O_2$ and $Li_{1.2}Ni_{0.13}Mn_{0.54}Co_{0.13}O_2$ are presented as TGA curve in Figure 5-1. The thermal stability of NMC batteries strongly depends on the content of nickel, manganese and cobalt. However, it is well known that a high nickel content contributes to higher capacity, high manganese content improves the cycling and safety characteristics while high content of cobalt enhances power performance. Therefore,

compositional optimization of the NMC chemistry is quite crucial for improving the electrochemical performance and safety characteristics of lithium ion batteries. The systematic investigation of thermal stability on a series of NMC cathode materials with different compositions will undoubtedly provide important information on formulating high-capacity materials with respectable safety characteristics. Unfortunately, not many systematic studies on a full series of NMC cathode chemistries have been reported so far. Hence, our TGA investigations will expand the knowledge base of NMC thermal stability and the effect of varying stoichiometry. It is observed from Figure 5-1 that $LiNi_{0.33}Mn_{0.53}Co_{0.14}O_2$ (a) and $Li_{1.2}Ni_{0.13}Mn_{0.54}Co_{0.13}O_2$ (b) are thermally stable with the significant mass loss recorded above 600 ^oC with the inflection points observed at 641℃ for $LiNi_{0.33}Mn_{0.53}Co_{0.14}O_2$ sample and 645℃ for $Li_{1.2}Ni_{0.13}Mn_{0.54}Co_{0.13}O_2$ sample respectively.

The sudden weight or temperature loss in TGA curves (commonly known as inflection point) signifies a change in the behaviour of the samples being analysed, which could be due to various factors such as evaporation of volatile components, chemical reactions, phase transitions, or experimental artifacts. Many materials contain volatile components that evaporates when exposed to increased temperature, leading to a decrease in the rate of weight. Moreover, some materials undergo chemical reactions at specific temperature ranges leading to the formation of new compounds or decomposition of existing ones, altering the weight loss behaviour while other materials can undergo phase transitions, such as melting or crystallization, which can affect their weight. The inflection point may correspond to the temperature range where such transitions occur, leading to changes in the rate of weight loss. However, since the mass loss recorded for both samples was above 600 ^oC, this is good news from an experimental point of view, as it is significantly above the elevated temperatures required during the fluorination procedures.

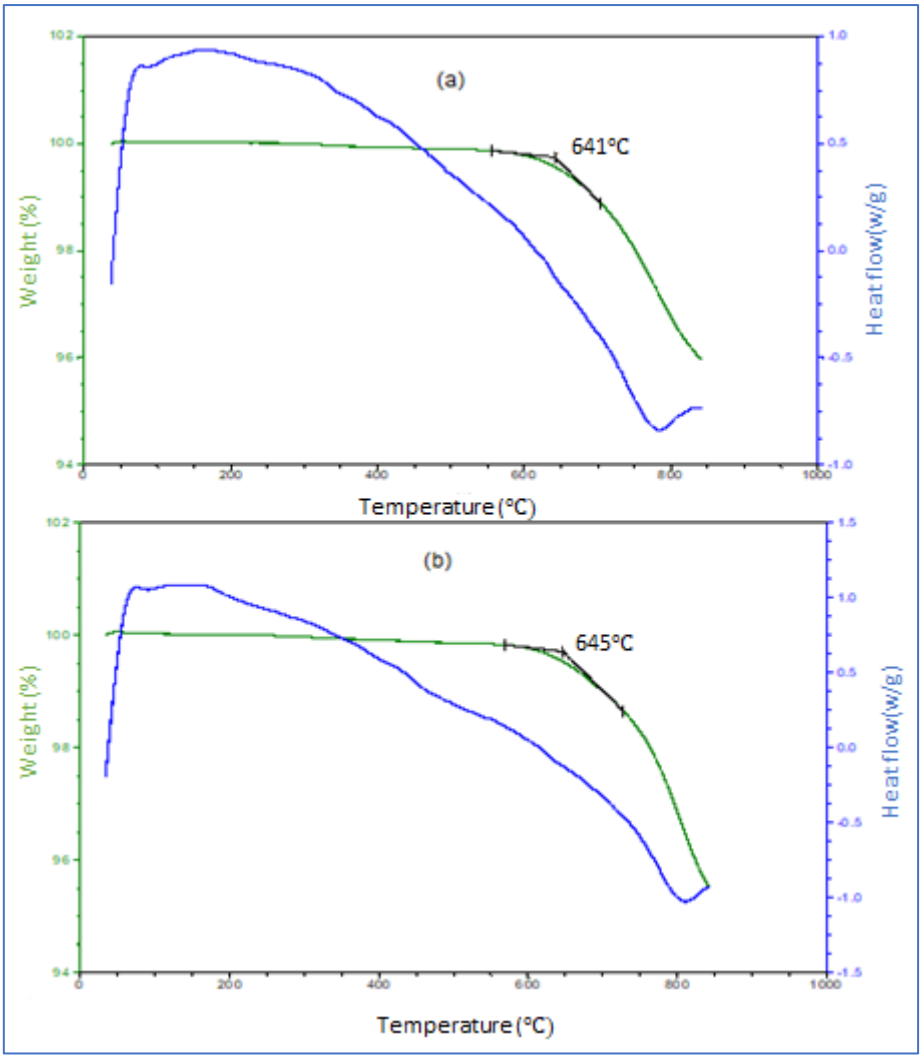

Figure 5-1. Thermogravimetric curve for (a) $LiNi_{0.33}Mn_{0.53}Co_{0.14}O_2$ and (b) $Li_{1.2}Ni_{0.13}Mn_{0.54}Co_{0.13}O_2$.

Table 5-1 summarises the decomposition onset temperature for the NMC oxides of the study. As can be noted in the above table, there seems to be a strong correlation between the increased theoretical wt% Mn content and a higher onset temperature of thermal decomposition. Even though there is a limited amount of literature available to explain this occurrence for lithiated samples, one specific study references the effect of varying; $Ni_xMn_yCo_z$ oxide stoichiometries

on thermal stability and specifically the onset temperature of oxide release in the discharge process of cathode candidate materials.

Table 5-1. Decomposition onset temperature for $LiNi_{0.33}Mn_{0.53}Co_{0.14}O_2$ and $Li_{1.2}Ni_{0.13}Mn_{0.54}Co_{0.13}O_2$.

Sample	Normalised Mn Ratio	Theoretical wt% Mn	Onset Temperature (°C)
$LiNi_{0.33}Mn_{0.53}Co_{0.14}O_2$	0.53	30.43	641
$Li_{1.2}Ni_{0.13}Mn_{0.54}Co_{0.13}O_2$	0.67	38.44	645

5.2. X-Ray Diffraction Analysis

X-ray diffraction (XRD) analysis is a powerful technique used to study the crystalline structure of materials. In the context of cathodes for lithium-ion batteries, such as Nickel Manganese Cobalt Oxide (NMC), XRD can provide valuable insights into the atomic arrangement and crystallographic phases of the material during various stages of battery operation. It is also a very flexible method that gives chemical data for phase analysis as well as elemental and texture analysis. X-ray diffractions for this study were performed using D8 Advance diffractometer equipped with flip-stick sample stage. The XRD technique was utilized to analyse the crystal structure of the carbonate co-precipitation precursors. Figure 6-2 (a) shows our calculated XRD using D8 Advance while Figure 5-2 (b) shows the XRD for $LiNi_{0.4}Mn_{0.4}Co_{0.2}O_2$, $LiNi_{0.3}Mn_{0.5}Co_{0.2}O_2$ and $LiNi_{0.2}Mn_{0.6}Co_{0.2}O_2$ from literature, which was calculated using the Bruker D8 Discover. Comparing the two figures, we note similar characteristics such as the intensity of 003 peak being greater than intensity of 104 peak, however, we also note impurity peaks in our XRD diagrams and this may be due to different

approaches used and different concentrations. Figure 5-3(a) shows the XRD diagram for $Li_{1.2}Ni_{0.13}Mn_{0.54}Co_{0.13}O_2$ and (b) XRD diagram for solution combustion synthesized $Li_{1.2}Ni_{0.13}Mn_{0.54}Co_{0.13}O_2$ respectively. Figure 5-3(b) shows what has been done with similar structure using different method. We note that our XRD compares well with the experimental data as the peaks produced appears at the same 2theta degree. The patterns are indexed to a hexagonal α-NaFeO2 structure with the R3m space group. Moreover, the absence of clear splitting between (108) / (110) peaks confirms high degree of cation mixing in our sample.

The spectra are depicted in the figures with the proposed phase and degree of crystallinity also highlighted. To a first order, the intensity of the peaks gives an indication of the wt. % of the corresponding phase in the sample. Thus, primary phases are given by the intense peaks, whereas, low intensities are indicative of minority phases in the sample**.** The high base line in the patterns is attributed to fluorescence of Ni, Mn and Co atoms by the Cu X-rays. From our results, we note sharp peaks for both figures indicating well-ordered crystalline structures with the most intensive peak appearing at (003).

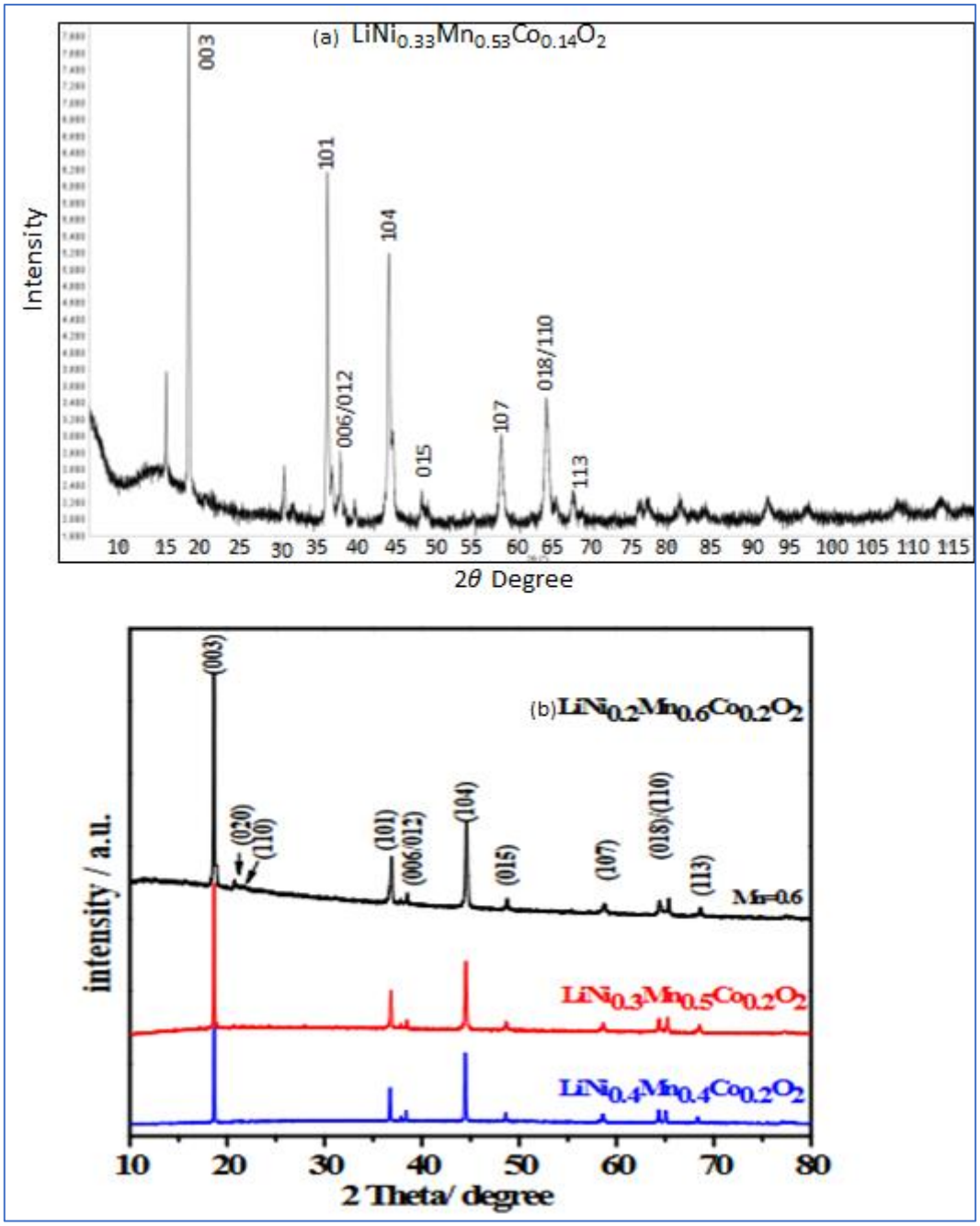

Figure 5-2. XRD for D8 Advance diffractometer (a) $LiNi_{0.33}Mn_{0.53}Co_{0.14}O_2$ and (b) Bruker D8 Discover for $LiNi_{0.4}Mn_{0.4}Co_{0.2}O_2$, $LiNi_{0.3}Mn_{0.5}Co_{0.2}O_2$ and $LiNi_{0.2}Mn_{0.6}Co_{0.2}O_2$ [146].

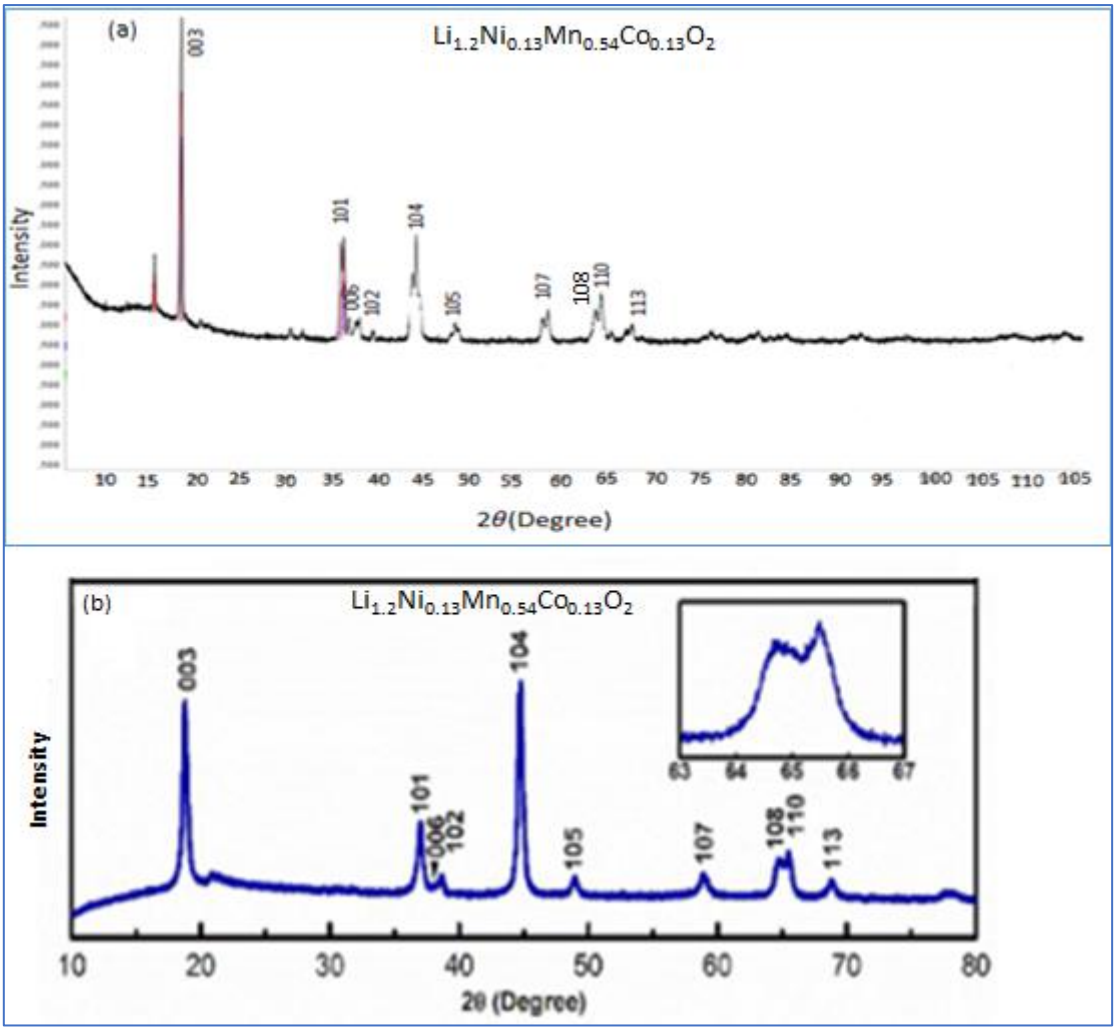

Figure 5-3. XRD for D8 Advance diffractometer (a) $Li_{1.2}Ni_{0.13}Mn_{0.54}Co_{0.13}O_2$ and (b) solution combustion synthesized $Li_{1.2}Ni_{0.13}Mn_{0.54}Co_{0.13}O_2$ [147].

5.3. Raman analysis

Raman spectroscopy can provide information about chemical composition, molecular structure, crystallinity, and phase identification without the need for extensive sample preparation. For this study, the Raman analysis investigation was focused on defining the effect of averaged crystal structure of the stability for cathode precursor matrices. It seems obvious from the data that the spectra for both samples look very similar with relation to the Raman shift positions as shown in Table 5-2. This is to be expected as the lattices are assembled in a similar manner with the bonding configuration following suit. However, peak intensities are

integral in understanding the intrinsic differences. Figure 5-4 and 5-5 present the Raman shift for both $LiNi_{0.33}Mn_{0.53}Co_{0.14}O_2$ and $Li_{1.2}Ni_{0.13}Mn_{0.54}Co_{0.13}O_2$. We note that the Raman active modes are observed between 400 and 1200 cm^{-1}, which are associated to the vibrational modes of different transition metal ions (Ni, Mn, Co). The Raman spectra of our samples consist of highly overlapping bands of different transition metal ions, thus it is difficult to assign the exact band to each vibration mode. However, it can be concluded that the bands > 600 cm^{-1} correspond to E_g and A_{1g} of Mn, while the shoulder at 465 cm^{-1} can be assigned to E_g mode of Ni.

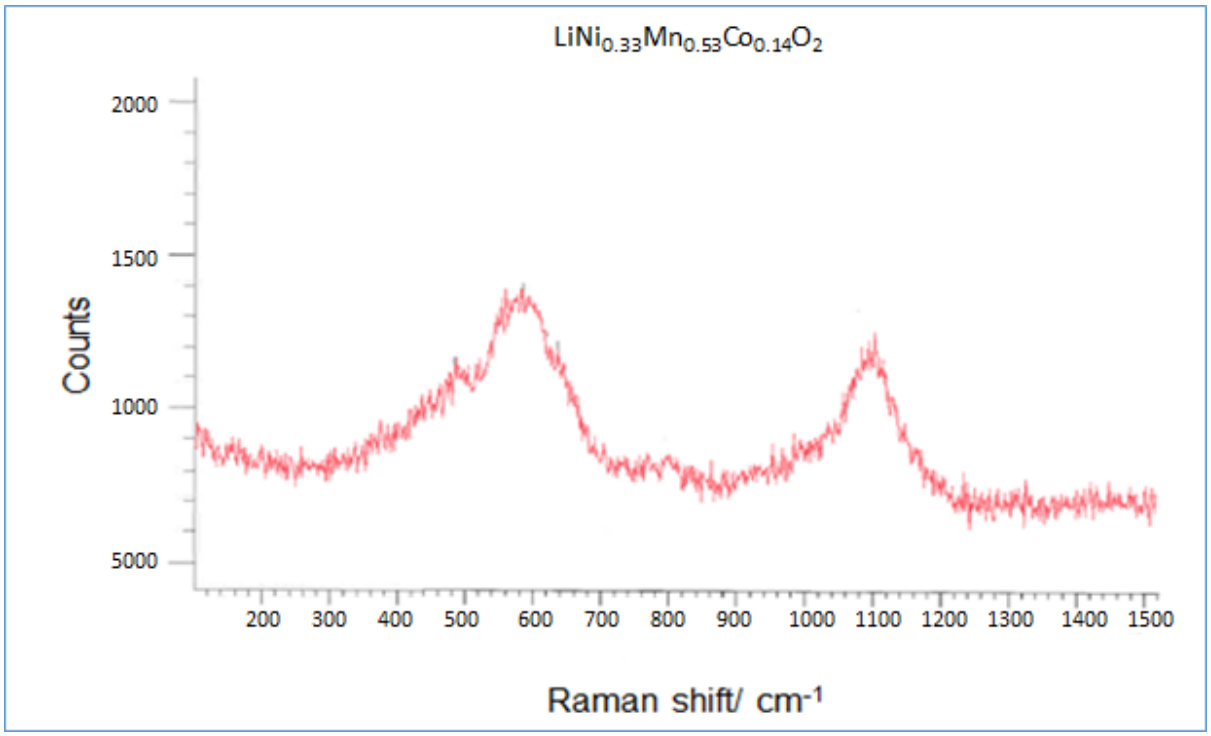

Figure 5-4. Raman spectroscopy for $LiNi_{0.33}Mn_{0.53}Co_{0.14}O_2$.

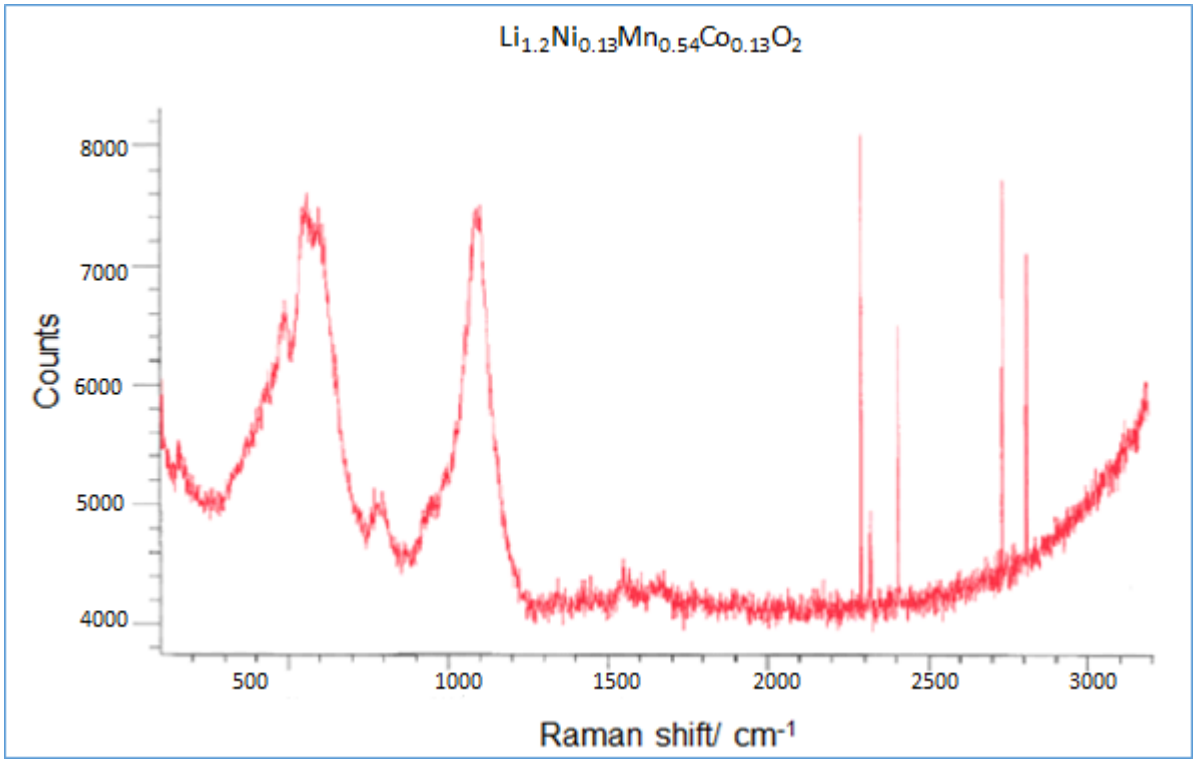

Figure 5-5. Raman spectroscopy for $Li_{1.2}Ni_{0.13}Mn_{0.54}Co_{0.13}O_2$.

Table 5-2. Predominant Raman shifts recorded for $LiNi_{0.33}Mn_{0.53}Co_{0.14}O_2$ and $Li_{1.2}Ni_{0.13}Mn_{0.54}Co_{0.13}O_2$.

$LiNi_{0.33}Mn_{0.53}Co_{0.14}O_2$ (cm^{-1})	$Li_{1.2}Ni_{0.13}Mn_{0.54}Co_{0.13}O_2$ (cm^{-1})
157	159
484	483
586	583
638	638
799	800
1100	1101

5.4. Energy-Dispersive X-ray Spectroscopy (EDX) and X-Ray Fluorescence (XRF) Analysis

An elemental analysis method that offers quantitative chemical data is X-ray fluorescence (XRF). XRF has a higher detection limit than EDS, and it can measure the concentrations of trace elements. The signal gathering technique is the main distinction between EDS and XRF.

XRF employs an analytical crystal to distinguish the X-rays coming off the sample surface, whereas EDS uses a Si (Li) detector. Because of this, XRF's peak resolution is superior to EDS's. An analytical crystal with a known composition has fixed interplanar space between its atoms, which makes it easier to distinguish between X-rays.

Table 5-3 highlights the theoretical wt% for each constituent and Mn/Ni and Mn/Co ratios for $LiNi_{0.33}Mn_{0.53}Co_{0.14}O_2$ and $Li_{1.2}Ni_{0.13}Mn_{0.54}Co_{0.13}O_2$ samples and compares this with the results obtained from the EDX and XRF analysis. As can be observed in Table 5-3, the Mn/Co and Mn/Ni ratios are slightly larger than expected as compared to the expected theoretical composition, in all cases. This could either imply that the stoichiometry isn't exactly what is expected in the sample or more likely that the oxygen and lithium content within the analytes influence the signal outputs in a systematically corrected manner.

Table 5-3. Comparison of theoretical percentage, EDX percentage and XRF percentage for $LiNi_{0.33}Mn_{0.53}Co_{0.14}O_2$ and $Li_{1.2}Ni_{0.13}Mn_{0.54}Co_{0.13}O_2$.

	$LiNi_{0.33}Mn_{0.53}Co_{0.14}O_2$	$Li_{1.2}Ni_{0.13}Mn_{0.54}Co_{0.13}O_2$
Theo wt% Mn	30.43	38.44
EDX wt% Mn	33.85	37.75
XRF wt% Mn	33.79	46.16
Theo wt% Ni	20.24	10.42
EDX wt% Ni	16.81	9.70
XRF wt% Ni	16.72	11.39
Theo wt% Co	8.62	10.46
EDX wt% Co	8.54	9.18
XRF wt% Co	13.62	12.24

5.5. Scanning Electron Microscopy (SEM)

Scanning Electron Microscopy is a powerful tool used to visualize the surface morphology of materials at a very high resolution. In the context of NMC (Nickel Manganese Cobalt) cathode materials used in lithium-ion batteries, SEM can reveal details about the particle size, shape, distribution, and surface features of these materials. NMC cathode materials typically consist of nanoparticles that contribute to the performance of lithium-ion batteries. SEM imaging of NMC materials can show the morphology of these nanoparticles, which is crucial in understanding their electrochemical properties and performance in batteries. For this study, the SEM was determined to check the particle size and distribution which reveal the size range of NMC particles, whether they are agglomerated or dispersed, and their distribution across the sample.

SEM was also determined to check the particle shape of our samples, which can showcase the shapes of individual particles, whether they are spherical, irregular or faceted. Figure 5-6 and 5-7 presents the micrographs for $LiNi_{0.33}Mn_{0.53}Co_{0.14}O_2$ and $Li_{1.2}Ni_{0.13}Mn_{0.54}Co_{0.13}O_2$. As can be seen from the micrographs, there seems to be a homogeneous particle distribution in each sample. The more evenly distributed the sample, the more likely it is to incur even loading during fluorination. So when considering thermal stability as well as morphological aspects, these candidate precursor materials seem to fulfil experimental requirements. We further determined the morphological characteristics such as density, surface area and average pore size for both samples as shown in Table 5-4. As expected, there isn't a massive difference observed in morphological characteristics of each sample. This basically means that the crystallographic 'holes' are more effectively filled, affording a slightly more dense configuration.

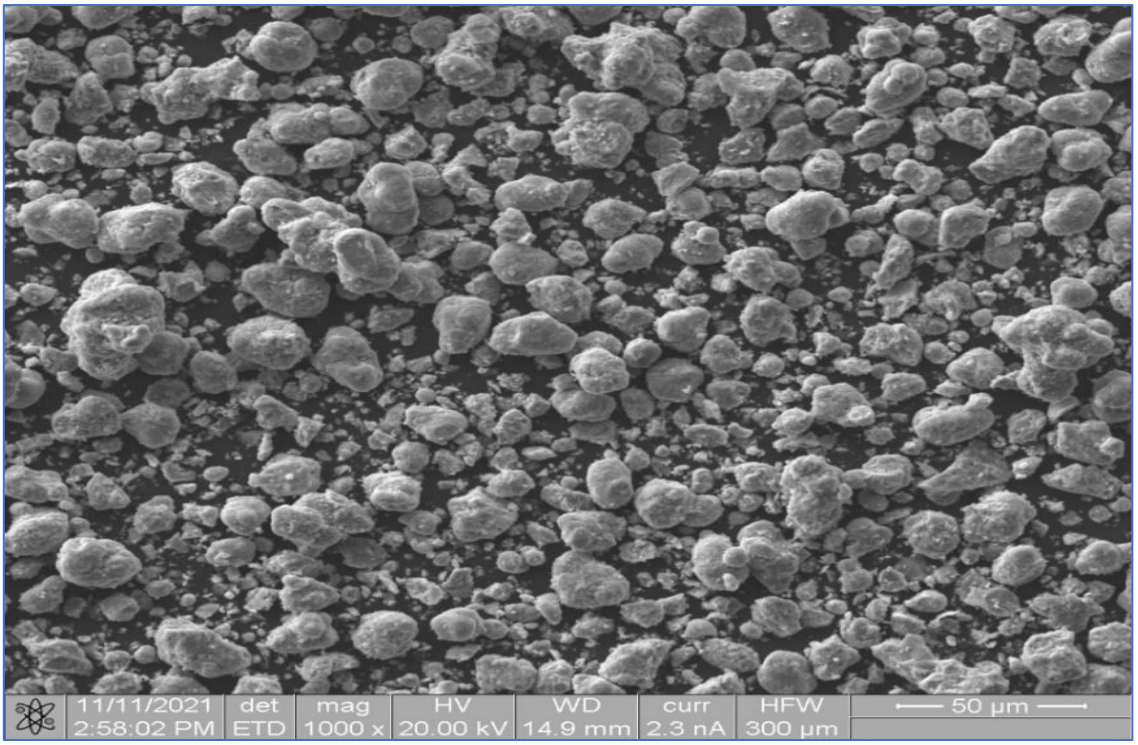

Figure 5-6. Secondary electron images for $LiNi_{0.33}Mn_{0.53}Co_{0.14}O_2$.

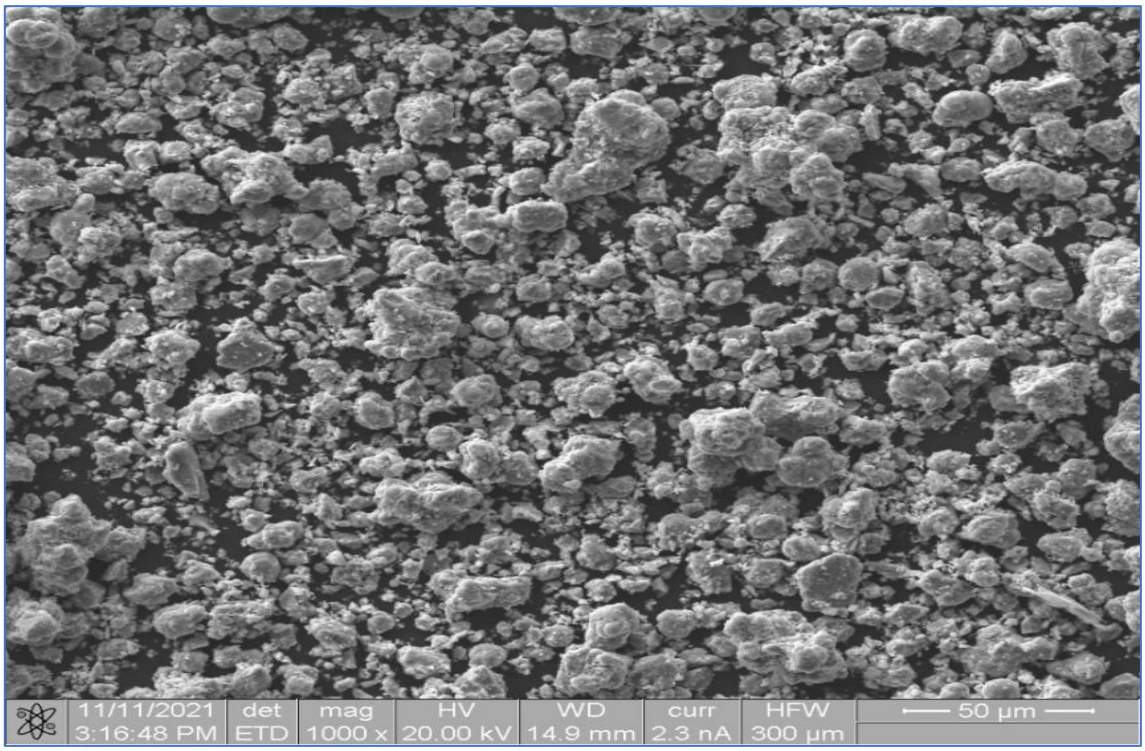

Figure 5-7. Secondary electron images for $Li_{1.2}Ni_{0.13}Mn_{0.54}Co_{0.13}O_2$.

Table 5-4. A summary of surface area (m2/g) and average pore size (Å) for $LiNi_{0.33}Mn_{0.53}Co_{0.14}O_2$ and $Li_{1.2}Ni_{0.13}Mn_{0.54}Co_{0.13}O_2$.

Sample	Surface area (m^2/g)	Average pore size (Å)
$LiNi_{0.33}Mn_{0.53}Co_{0.14}O_2$	1.0029	115.017
$Li_{1.2}Ni_{0.13}Mn_{0.54}Co_{0.13}O_2$	1.1391	103.117

5.6. Particle size distribution for $LiNi_{0.33}Mn_{0.53}Co_{0.14}O_2$ and $Li_{1.2}Ni_{0.13}Mn_{0.54}Co_{0.13}O_2$.

Particle Size Distribution (PSD), describes the range and distribution of particle sizes within a material. Most materials especially the active materials used in battery electrodes, contain a variety of particle sizes instead of a single particle size. The PSD can be described through various metrics like the mean size, median size or mode size and is typically characterized using various techniques. The impact of particle size distribution on the lithium ion battery performance includes the ionic diffusion, whereby smaller particles provide shorter diffusion pathways for lithium ions, which is conducive to faster charge and discharge rates. Therefore, a finer PSD tends to enhance rate capability, especially beneficial for applications requiring rapid energy delivery such as acceleration in electric vehicles. The structural integrity and cycling stability is also included as the impact of PSD whereby finer particles, due to their high surface area to volume ratio, are more prone to degradation mechanisms such as cracking. Therefore, a PSD skewed heavily towards the finer end can compromise the long-term stability of the battery [148].

Figure 5-8 and Figure 5-9 shows the particle size distribution for $LiNi_{0.33}Mn_{0.53}Co_{0.14}O_2$ and $Li_{1.2}Ni_{0.13}Mn_{0.54}Co_{0.13}O_2$. We note that the particle size distribution curve starts at zero and remain constant until it reaches the D10, then gradually increases until it reaches a peak around the median peak at D50 and continues to remain constant. From Table 5-2, we note that D10 =

16.63 and 9.88. This implies that 10% of the $LiNi_{0.33}Mn_{0.53}Co_{0.14}O_2$ sample is smaller than $16.63\mu m$ while 10% of $Li_{1.2}Ni_{0.13}Mn_{0.54}Co_{0.13}O_2$ sample is smaller than $9.88\mu m$. Furthermore, we also note that 50% of $LiNi_{0.33}Mn_{0.53}Co_{0.14}O_2$ sample is smaller than 22.36 μm while 50% of $Li_{1.2}Ni_{0.13}Mn_{0.54}Co_{0.13}O_2$ sample is smaller than 15.24 μm. The D50 is commonly known as the median value as it divides the particle size distribution into equal amounts of "smaller" and "larger" particles. The 90% of $LiNi_{0.33}Mn_{0.53}Co_{0.14}O_2$ sample is smaller than 30.38 μm while the 90% of $Li_{1.2}Ni_{0.13}Mn_{0.54}Co_{0.13}O_2$ sample is smaller than 21.16 μm. Usually the D10, D50 and D90 are the most crucial percentiles for a particle size distribution.

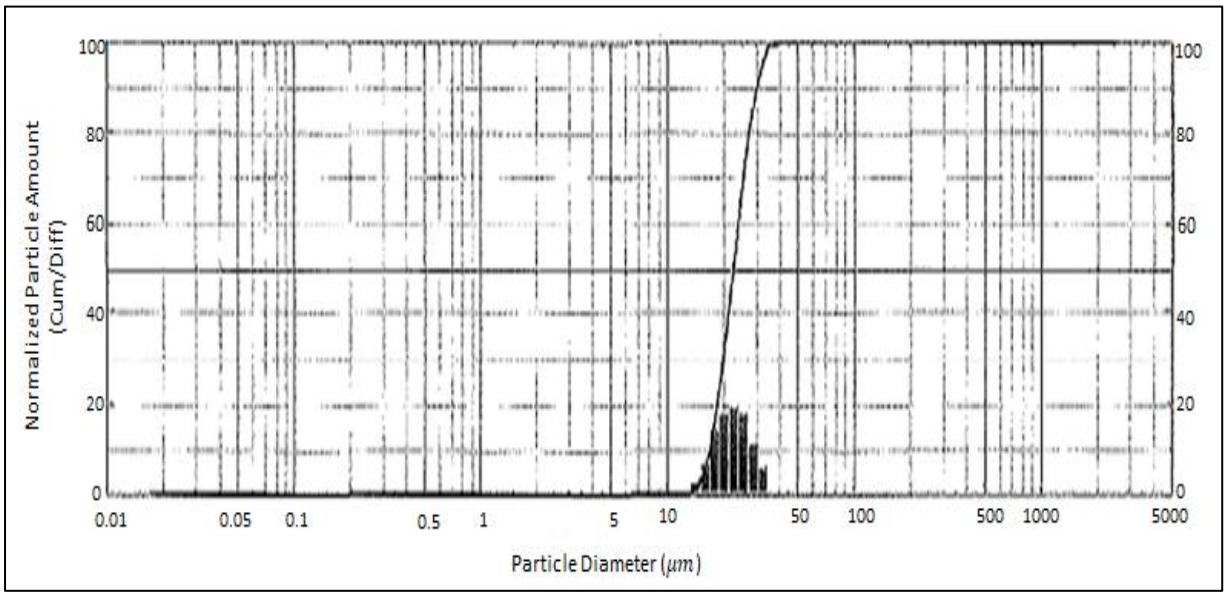

Figure 5-8. Particle size distribution for $LiNi_{0.33}Mn_{0.53}Co_{0.14}O_2$.

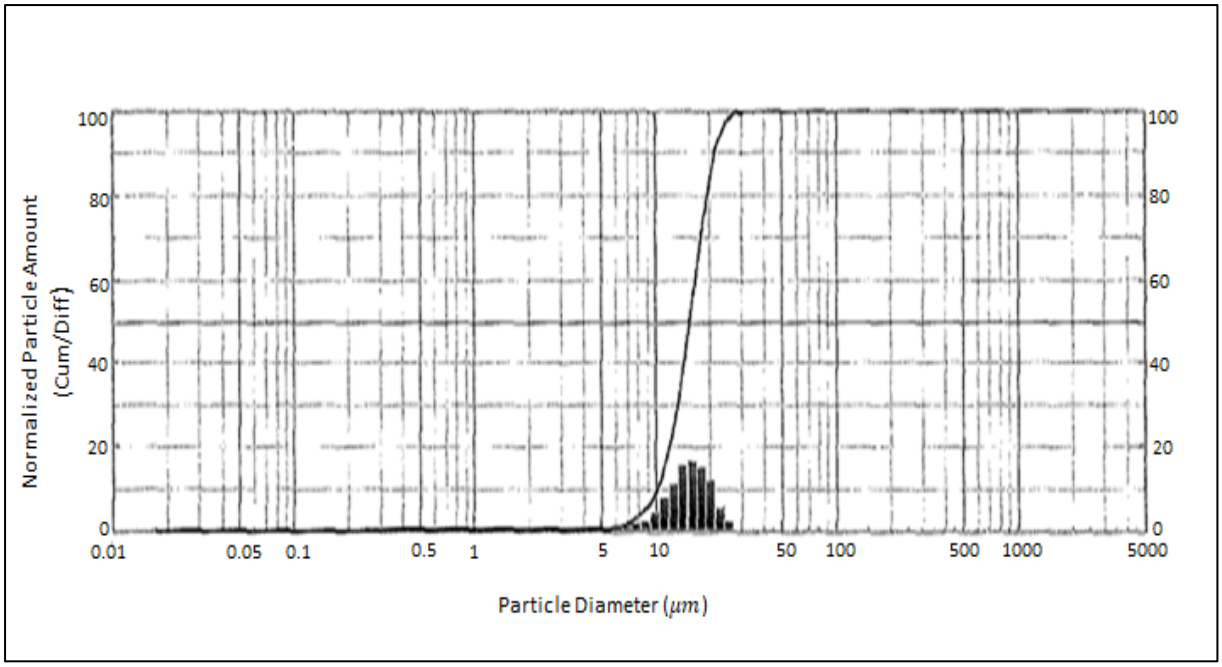

Figure 5-9. Particle size distribution for $Li_{1.2}Ni_{0.13}Mn_{0.54}Co_{0.13}O_2$.

Table 5-5. The particle diameter for $LiNi_{0.33}Mn_{0.53}Co_{0.14}O_2$ and $Li_{1.2}Ni_{0.13}Mn_{0.54}Co_{0.13}O_2$.

Sample	D10	D20	D30	D40	D50	D60	D70	D80	D90
$LiNi_{0.33}Mn_{0.53}Co_{0.14}O_2$	16.63	18.08	19.46	20.94	22.36	23.78	25.30	26.92	30.38
$Li_{1.2}Ni_{0.13}Mn_{0.54}Co_{0.13}O_2$	9.88	11.58	13.08	14.17	15.24	16.39	17.780	19.396	21.16

5.7. Tapped density for $LiNi_{0.33}Mn_{0.53}Co_{0.14}O_2$ and $Li_{1.2}Ni_{0.13}Mn_{0.54}Co_{0.13}O_2$

Tap density refers to the density of a powder material after it has been tapped or subjected to mechanical compaction. Calculating the tapped density of NMC's as cathode materials for lithium-ion batteries provides valuable information for material characterization, electrode optimization, performance prediction, quality control and cost optimization which are essential for the development and production of high-performance lithium-ion batteries. Determining the tap density of a metal powder provides valuable information on the volume occupied by a

specific weight of the powder before and after consolidation through tapping. To determine the tap density, a graduated measuring cylinder containing the powder sample is mechanically tapped to record the final volume after tapping as the initial volume is recorded before tapping. After the weight and volumes of the sample are recorded, the formula below is then used to calculate the tap density for both our samples. We note that the tapped density for both samples was less than 2 g/ cm^3 which is typical for experimental point of view.

$$\text{Tapped density} = \frac{mass\ of\ the\ tapped\ sample}{volume\ of\ the\ tapped\ sample}$$

For $LiNi_{0.33}Mn_{0.53}Co_{0.14}O_2$

Mass = 30g

V_0 = 35 cm^3

V_f = 28 cm^3

Bulk density = $\frac{m}{V0} = \frac{30}{35}$ = 0.86 g/ cm^3

Tap density = $\frac{m}{vf} = \frac{30}{28}$ = 1.07 g/ cm^3

For $Li_{1.2}Ni_{0.13}Mn_{0.54}Co_{0.13}O_2$

Mass = 30g

V_0 = 23 cm^3

V_f = 19 cm^3

Bulk density = $\frac{m}{V0} = \frac{30}{23}$ = 1.30 g/ cm^3

Tap density = $\frac{m}{vf} = \frac{30}{19}$ = 1.58 g/ cm^3

5.8. The synchroton based XAS for $LiNi_{0.33}Mn_{0.53}Co_{0.14}O_2$ and $Li_{1.2}Ni_{0.13}Mn_{0.54}Co_{0.13}O_2$

In this part, we collaborated with the British council to use their Diamond light source synchrotron beam to determine the effect of fluorination in our samples. In particular, we wanted to determine if fluorination changes the oxidation state of our transition metals (Mn, Ni Co). After getting results from the beam, we used a programme called Athena to first normalize our data. We normalized the Ni-K, Mn-K and Co-K edges and the results are shown in the figures below.

5.8.1. Ni-K edge

Figure 5-10 present the brief overview of the X-ray absorption spectrum (XAS), which is a powerful technique used to probe the electronic and structural environment around specific atoms within a material. It is mainly divided into two regions named the x-ray absorption near edge structure (XANES) and extended x-ray absorption fine structure (EXAFS). The XANES spectra exhibits two more features named the pre-edge and the absorbing edge which gives information about the local symmetry, oxidation state and coordination of the absorbing atom while EXAFS provides information about the interatomic distances, coordination number and neighbour identity. From Fig 5-11 we note that the pre-edge feature is at the same position for both pristine and fluorinated samples which indicate that the oxidation state in this regard does not change with fluorination, instead it remains the same. We also note that the pre-edge feature exhibit a single peak which implies that the oxidation state for these samples is a +2. Furthermore, Fig 5-12 as a zoomed spectra for Fig 5-11 shows that some spectra exhibit an additional peak on the absorption edge, which is typically indicative of a ligand transition. However, since the feature appears in both pristine and fluorinated sample, it clearly indicate

that this additional peak is not due to fluorination but may be linked to other transition metals within the sample.

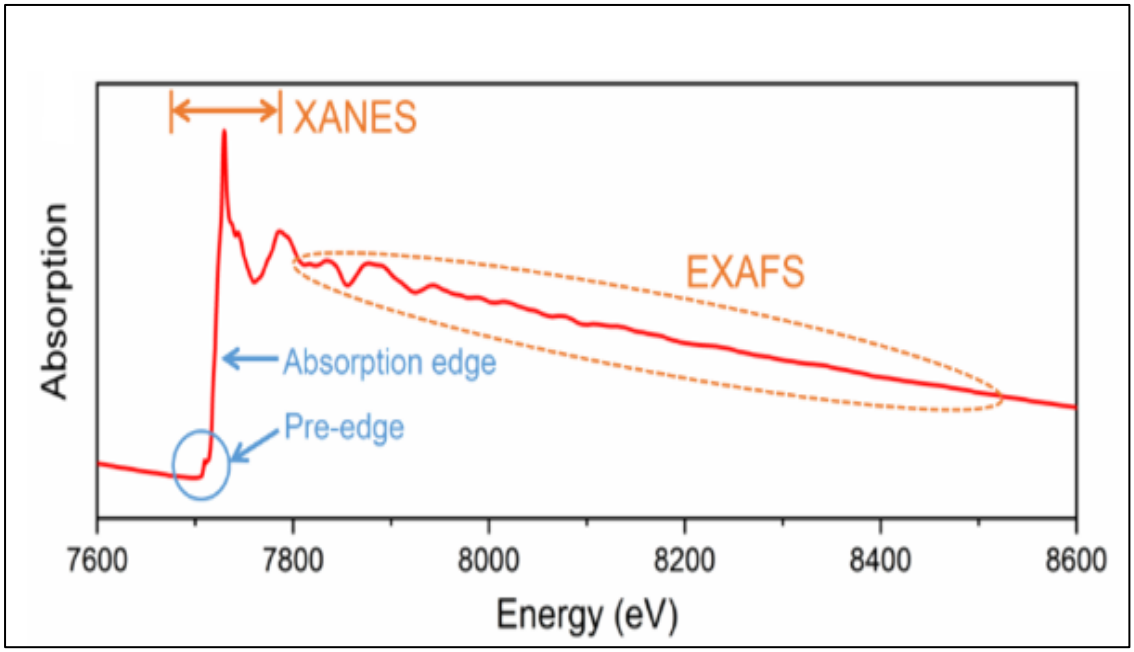

Figure 5-10. Normalized X-ray absorption spectroscopy.

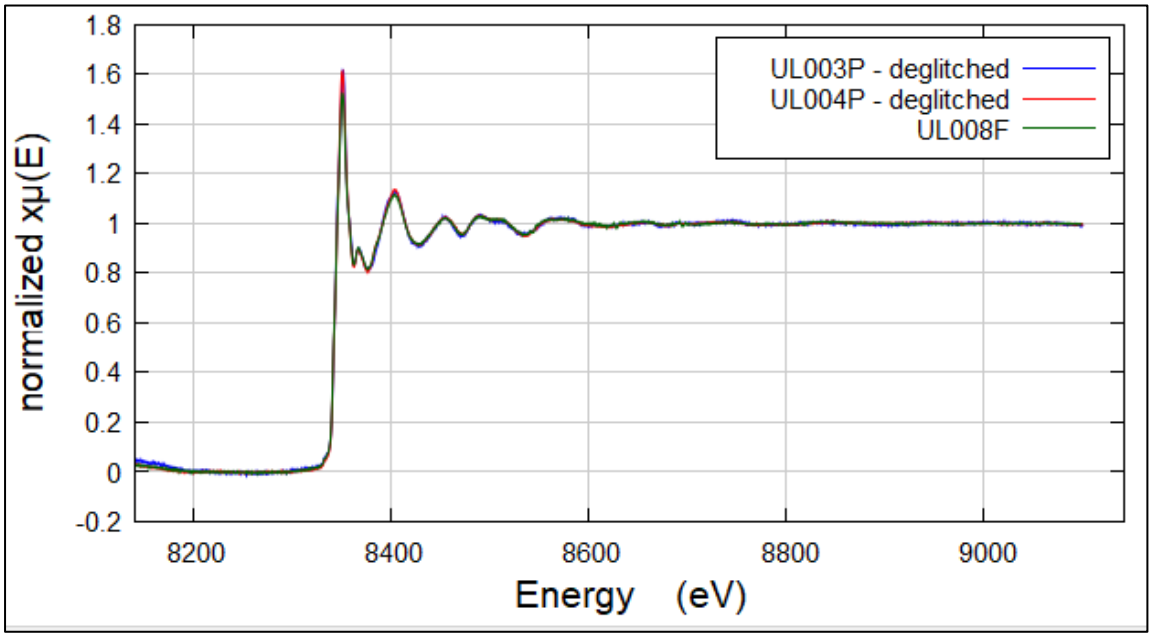

Figure 5-11. Normalized spectra of Ni-K edge for pristine and fluorinated samples.

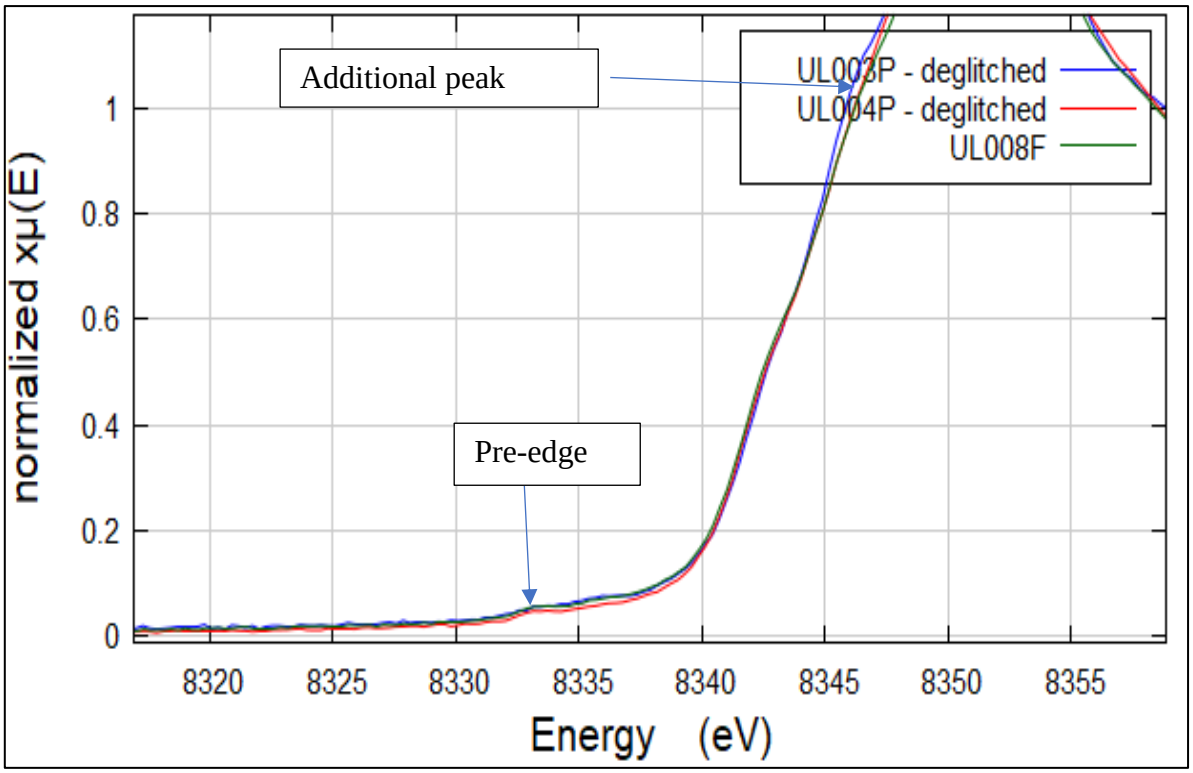

Figure 5-12. Zoomed normalized spectra of Ni-K edge.

Figure 5-13 presents the Fourier transform EXAFS spectra for Ni-K-edge which converts the data from reciprocal space (wave vector k) to real space (radial distance R), revealing distances between the absorbing atom and its neighbours. The first shell reveal that the pathway between nickel and its neighbouring atoms move from nickel to oxygen atom while the second shell corresponds to pathway from nickel to metal or ligand atoms. Their radial distances are recorded in Table 5-6 whereby it is notable that all the structures (pristine and fluorinated) have the same interatomic distances which further confirms that the oxidation state is not changing since there's no change in bond length as this is proportional to the oxidation state (higher oxidation state= shorter bond length).

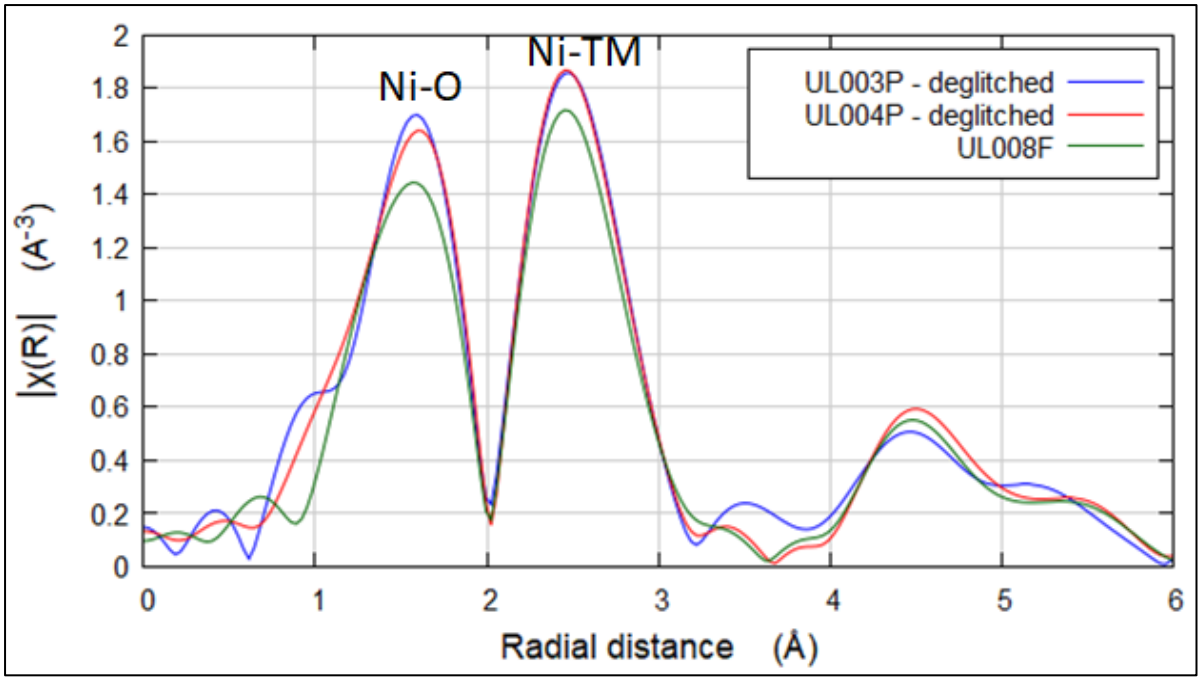

Figure 5-13. The Fourier transform EXAFS of Ni-K edge for both pristine and fluorinated NMC sample

Table 5-6. Radial distances between the absorbing atom (Ni, Mn, Co) to Oxygen and radial distances from metal to metal or ligand.

Sample Composition	R-Factor	Radial distance (M-O)	Radial distance (M-M)
$Li_{1.2}Ni_{0.33}Mn_{0.53}Co_{0.14}O_2$ **(P)**	0.01	1.9	2.9
$Li_{1.2}Ni_{0.13}Mn_{0.54}Co_{0.13}O_2$ **(P)**	0.02	1.9	2.9
$Li_{1.2}Ni_{0.33}Mn_{0.53}Co_{0.14}O_2$ **(F)**	0.01	1.9	2.9

5.8.2. Mn-K edge

The Mn K-edge refers to the absorption edge associated with the excitation of an electron from the 1s core level to higher energy states in manganese (Mn), typically observed in X-ray absorption spectroscopy (XAS) as presented in Fig 5-14. In the case of Mn, the pre-edge features are typically attributed to transitions from the Mn 1s core level to unoccupied Mn 3d

states, often hybridized with ligand orbitals. On the pre-edge feature as shown in the zoomed spectra in Fig 5-15, we can observe two clear peaks of Mn. These two distinct pre-edge peaks often emerge, reflecting the stronger ligand field splitting and multiple d-orbital levels available for transitions. This further imply that the oxidation state cannot be a +2 since there's more than one peak. The oxidation state in this case can either be Mn^{3+} or Mn^{4+}.

Moreover, Figure 5-16 present the Fourier Transform EXAFS for Mn K-edge which provides a way to analyze the local atomic structure around the absorber atom (in this case, manganese). The FT of EXAFS transforms the oscillatory function in terms of wavenumber k (which corresponds to the photoelectron energy) into real space, giving peaks that represent distances between the absorbing Mn atom and its neighbouring atoms. Each peak in the Fourier-transformed EXAFS spectrum corresponds to a different coordination shell or "scattering pathway" of neighbouring atoms around the Mn atom. These pathways are typically grouped by distance whereby the first coordination shell corresponds to the closest atoms to Mn, often oxygen or other ligands while the second shell coordination corresponds to the more distant ligand atoms. From Fig 5-16 we note that the first shell indicate the Mn to Oxygen pathway while the second shell present Mn to oxygen or any other ligands within the sample.

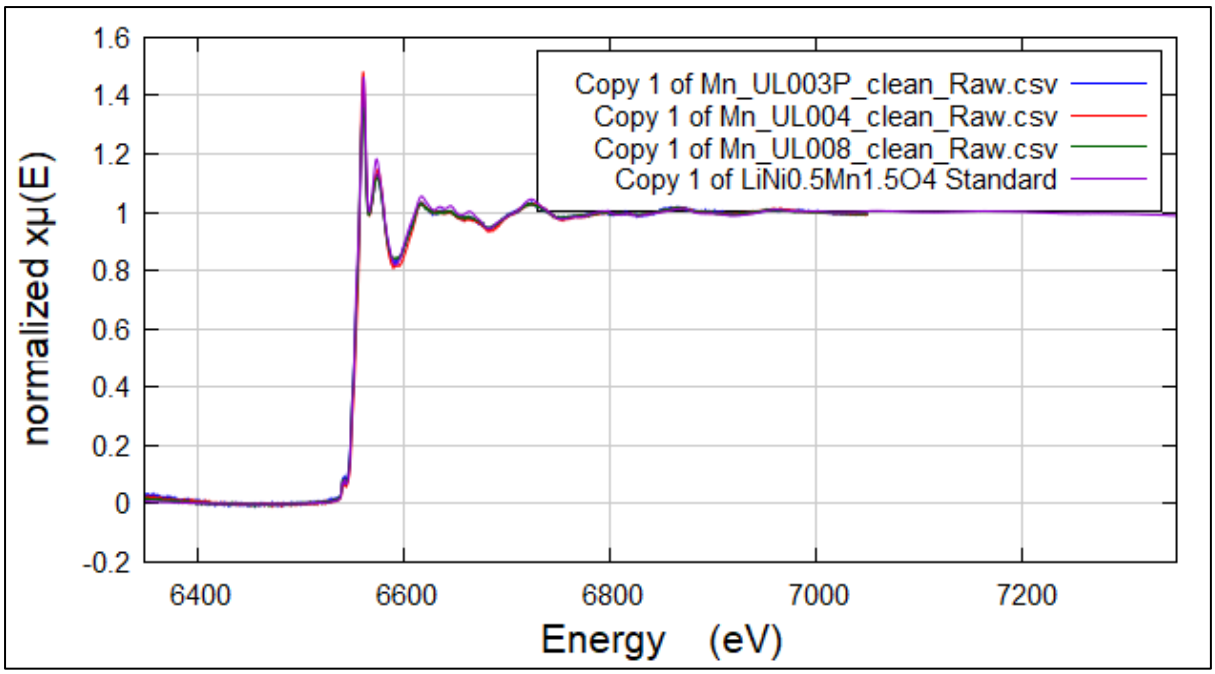

Figure 5-14. Normalized spectra of Mn K-edge for pristine and fluorinated samples.

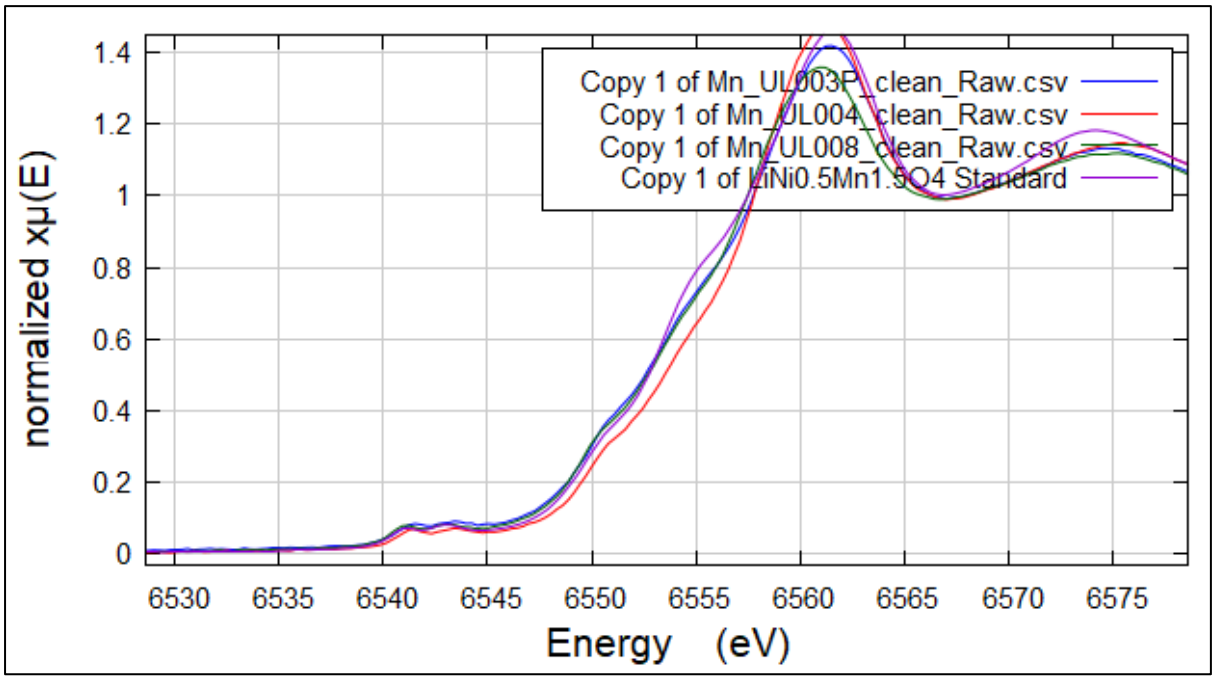

Figure 5-15. Zoomed spectra for Mn K-edge

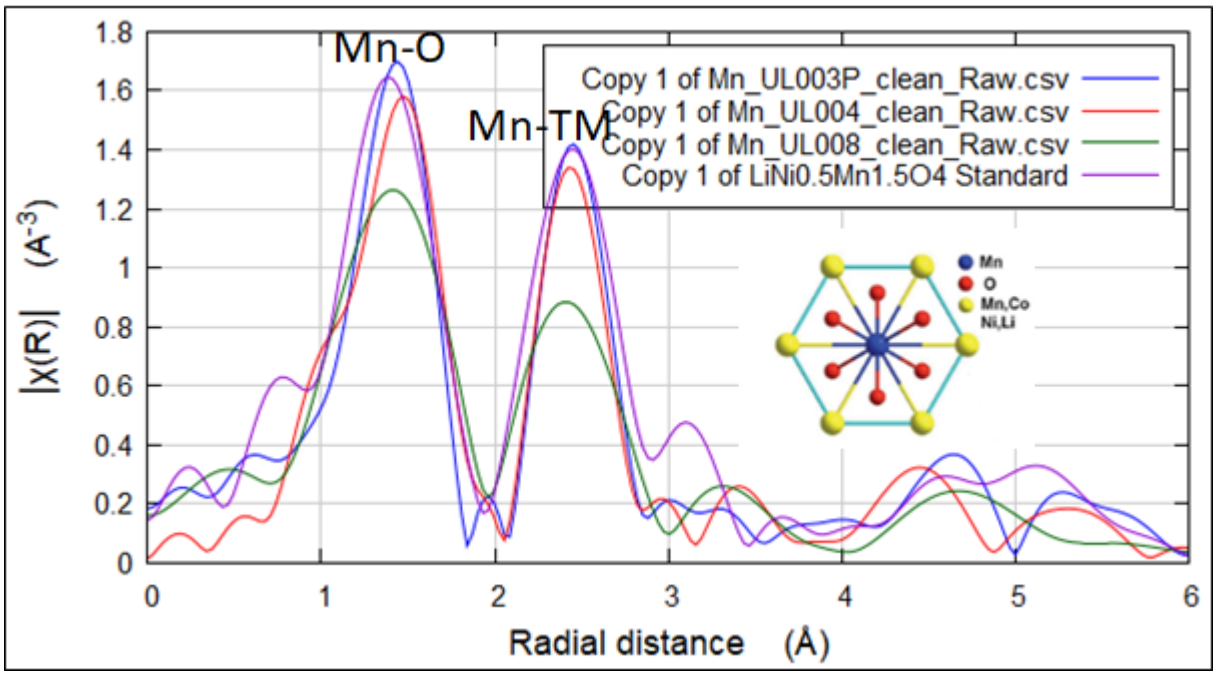

Figure 5-16. Fourier Transform EXAFS for Mn K-edge

5.8.3. Co K-edge

The Co K-edge refers to the X-ray absorption edge associated with the excitation of a core electron from the 1s orbital of cobalt (Co) to unoccupied higher energy states. It is a key feature studied in X-ray Absorption Spectroscopy (XAS), particularly for understanding the local electronic structure, oxidation state, and coordination environment of cobalt in various materials. The pre-edge region in a Co K-edge XAS spectrum often shows weak features due to transitions from the Co 1s level to Co 3d states. These pre-edge features are generally small because 1s → 3d transitions are quadrupole allowed but dipole forbidden. However, these transitions can gain intensity due to hybridization with ligand orbitals or due to distortions in the coordination geometry (such as tetrahedral coordination). As shown in Figure 5-17 and its zoomed spectra in Figure 5-18, we observe the pre-edge feature with a single peak implying that the oxidation state in this regard is Co^{2+}. Its pathway shown in Figure 5-18 indicate that atoms move from Co to oxygen then Co to metal or any ligands within the sample, respectively.

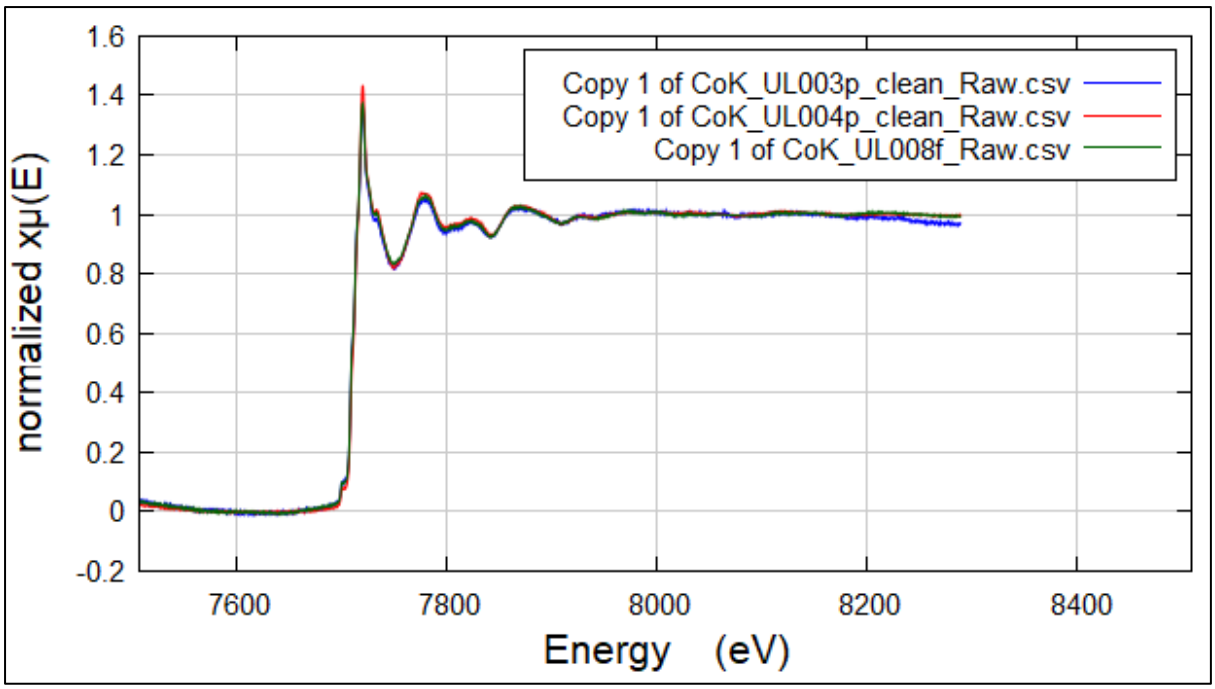

Figure 5-17. Normalized X-ray absorption spectroscopy of Co K-edge for pristine and fluorinated samples.

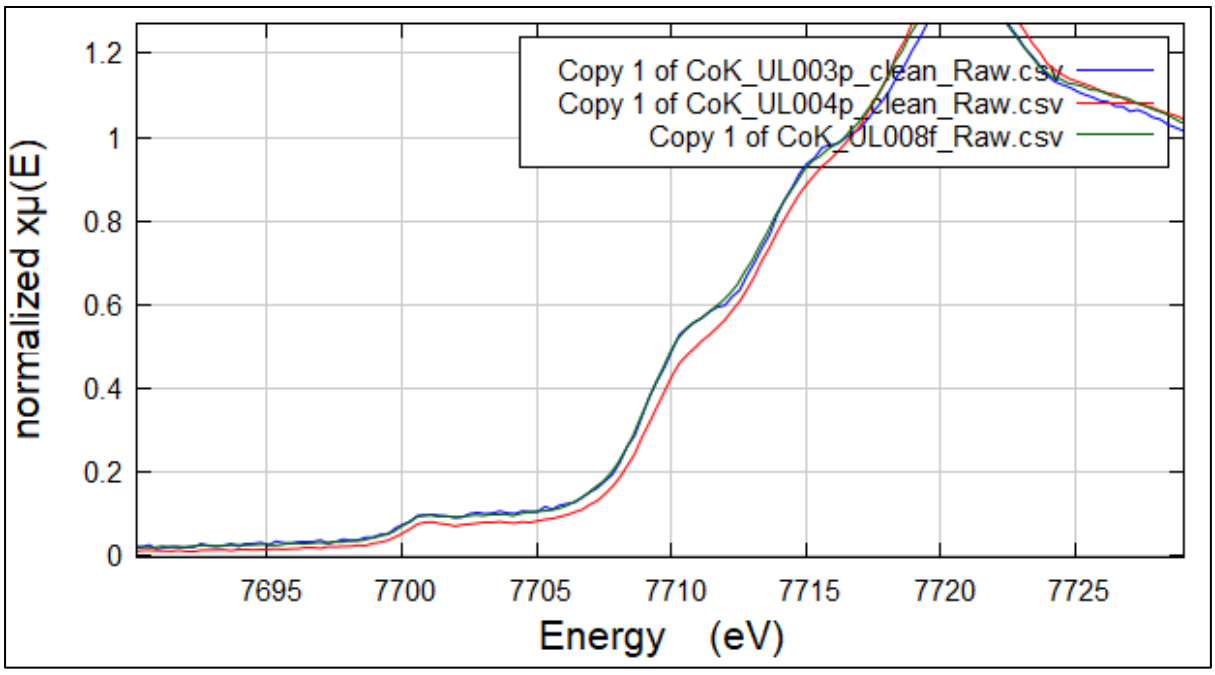

Figure 5-18. Zoomed spectra of Co K-edge XAS

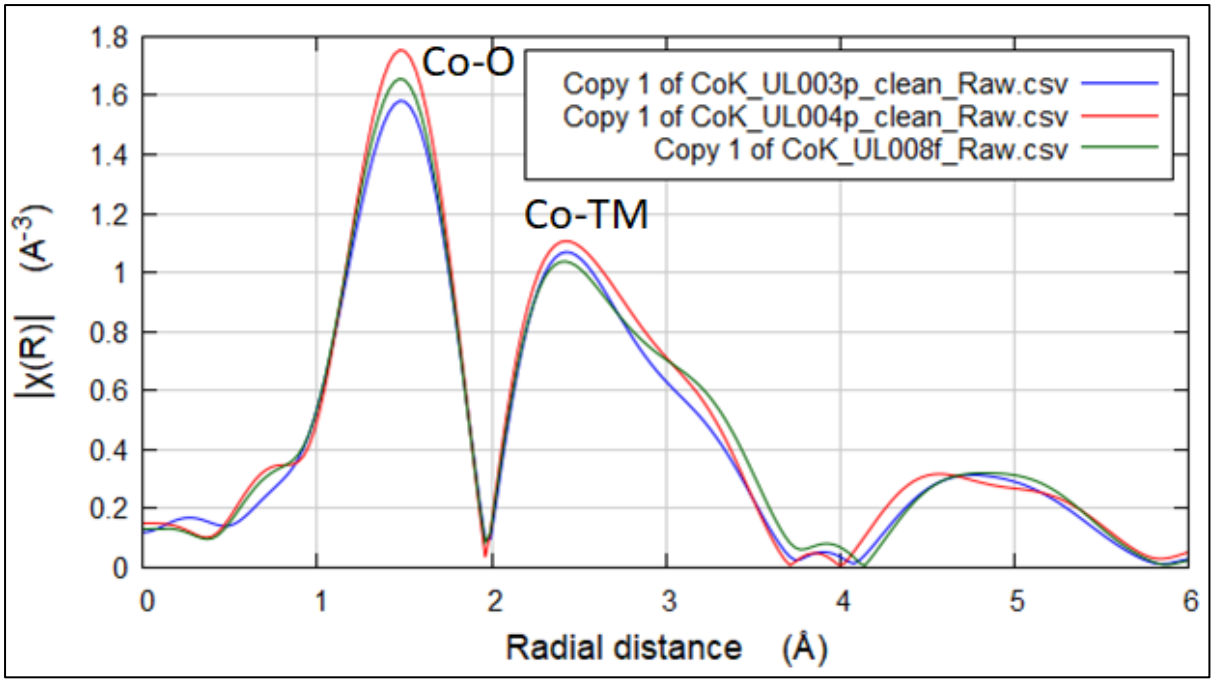

Figure 5-19. Fourier Transform EXAFS for Co K-edge

Chapter 6

6.1. Summary and Conclusions

Density functional theory with Hubbard parameter (U) were employed in this study to investigate the structural, electronic and mechanical properties of Mn-rich $NiMnCoCO_3$ and $NiMnCoO_2$ with high Mn concentration and minor amounts of Ni and Co. We employed DFT with Hubbard correction *U* calculation within the exchange correlation of GGA-PBE as embodied in the VASP code, and the PHONON codes. The equilibrium cell characteristics and energy of formation were determined by full structure optimization. The spin-polarized local density approximation was also used to calculate the electronic total and partial densities of states while mechanical properties were found by computing elastic properties and phonon dispersion curves.

Computational studies on Mn-rich NMC's were not found in literature to compare our results with, hence the computational results of this study will be used for bench-marking in the future. We firstly used Media software to build supercells for $Ni_{0.3}Mn_{0.5}Co_{0.2}CO_3$ and $Ni_{0.3}Mn_{0.5}Co_{0.2}O_2$ structures, then calculate their stability properties. Our calculated lattice parameters for $Ni_{0.3}Mn_{0.5}Co_{0.2}CO_3$ were smaller than the lattice parameters for $Ni_{0.3}Mn_{0.5}Co_{0.2}CO_3$ which typically indicate that $Ni_{0.3}Mn_{0.5}Co_{0.2}CO_3$ structure has a smaller unit cell volume, smaller density and closer atomic packing as compared to $Ni_{0.3}Mn_{0.5}Co_{0.2}CO_3$ supercell. The heats of formation for $Ni_{0.3}Mn_{0.5}Co_{0.2}CO_3$ were found to be more stable than $Ni_{0.3}Mn_{0.5}Co_{0.2}O_2$ due to its lower energy of formation value. We further doped both systems with fluorine, titanium, niobium and chromium to enhance both our system's behaviors. Their heats of formations were calculated and we found that their results are relatively low and negative, suggesting thermodynamic stability for all doped systems. However, F-doped

$Ni_{0.3}Mn_{0.5}Co_{0.2}CO_3$ has the heats of formation of -6765.23 kJ/mol which is more negative as compared to other doped supercells and this implies that F-doped $Ni_{0.3}Mn_{0.5}Co_{0.2}CO_3$ is more energetically favorable or thermodynamically stable.

We have also calculated the band structures and the density of states for both supercells to investigate their electronic structure behavior. From the band structures, we note that $Ni_{0.3}Mn_{0.5}Co_{0.2}CO_3$ and $Ni_{0.3}Mn_{0.5}Co_{0.2}O_2$ shows the direct energy band gap of 0.004 eV and 0.036 eV which suggest that both supercells are either metallic or semiconductors, hence high in electronic conductivity. This was confirmed by calculating the density of states for both systems. With the density of states for $Ni_{0.3}Mn_{0.5}Co_{0.2}CO_3$, we note that peaks that appears on the valence band side of the total DOS are mainly contributed by manganese d-states and carbon p-states with minor amounts of nickel d-states and cobalt d-states. We also note the presence of pseudogap and that the Fermi level lies on the right of it, thus permissible for valence band states to overlap to the conduction band. The existence of pseudogap suggests that $Ni_{0.3}Mn_{0.5}Co_{0.2}CO_3$ has a metallic behavior characteristics and good electronic conduction since no energy band gap is observed, which correspond well with the band structure prediction. Furthermore, from the density of states of $Ni_{0.3}Mn_{0.5}Co_{0.2}O_2$, we note that peaks in the total DOS are dominated by nickel and cobalt d-states and oxygen p-states. We also note a small pseudogap with the Fermi line lying on the left side of the pseudogap. This also indicate a metallic behavior and good electronic conductor because no energy band gap is observed.

For fluorine doped $Ni_{0.3}Mn_{0.5}Co_{0.2}CO_3$ and $Ni_{0.3}Mn_{0.5}Co_{0.2}O_2$ at oxygen sites, we note that there are energy bands crossing the fermi energy level in both spin directions, indicating that both doped system are metallic, hence good electronic conductors. The density of states for fluorine doped $Ni_{0.3}Mn_{0.5}Co_{0.2}CO_3$ and $Ni_{0.3}Mn_{0.5}Co_{0.2}O_2$ shows that both system have the

metallic behavior due to the presence of pseudogap at the Fermi level. We further calculated band structures and density of states for titanium doped $Ni_{0.3}Mn_{0.5}Co_{0.2}CO_3$ and $Ni_{0.3}Mn_{0.5}Co_{0.2}O_2$ at Mn sites. For Ti-doped $Ni_{0.3}Mn_{0.5}Co_{0.2}CO_3$, the system shows a half metallic ferromagnet which indicate that bands for spin 2 are metallic while bands for spin 1 are semiconducting. This behavior indicates that this system is either a semiconductor or metallic, hence good electronic conductor while the band structure and density of states for Ti-doped $Ni_{0.3}Mn_{0.5}Co_{0.2}O_2$ shows a metallic behavior at the Fermi level indicating good electronic conductor. Moreover, we further doped both our systems with niobium to investigate their electronic properties. We note the flow of electrons from the valence bands to the conduction bands which indicate that no energy band gap is recorded for both niobium doped $Ni_{0.3}Mn_{0.5}Co_{0.2}CO_3$ and $Ni_{0.3}Mn_{0.5}Co_{0.2}O_2$ which implies metallic behavior indicating good electronic conductor. Lastly, the electronic properties were calculated for chromium doped $Ni_{0.3}Mn_{0.5}Co_{0.2}CO_3$ and $Ni_{0.3}Mn_{0.5}Co_{0.2}O_2$ by determining their band structures and density of states. We note that their band structures and density of states revealed that both chromium doped systems shows half ferromagnetic behavior since bands for spin one are metallic while bands for spin two are semiconducting. However, this characteristic indicate that both systems are good electronic conductors.

Furthermore, the mechanical properties for $Ni_{0.3}Mn_{0.5}Co_{0.2}CO_3$, $Ni_{0.3}Mn_{0.5}Co_{0.2}O_2$ and their doped systems were determined by calculating the elastic properties. The elastic constants of $Ni_{0.3}Mn_{0.5}Co_{0.2}CO_3$, F-doped $Ni_{0.3}Mn_{0.5}Co_{0.2}CO_3$, Ti-doped $Ni_{0.3}Mn_{0.5}Co_{0.2}CO_3$, Nb-doped $Ni_{0.3}Mn_{0.5}Co_{0.2}CO_3$ and Cr-doped $Ni_{0.3}Mn_{0.5}Co_{0.2}CO_3$ satisfy the necessary conditions for mechanical stability within the triclinic systems. Moreover, we also note that the elastic constants for $Ni_{0.3}Mn_{0.5}Co_{0.2}O_2$ shows a negative value of C_{55}, hence the stability condition for $C_{55} > 0$ is not satisfied, suggesting mechanical instability. We further note that even after

doping $Ni_{0.3}Mn_{0.5}Co_{0.2}O_2$ with fluorine, titanium, niobium and chromium the system remained mechanically unstable as the stability conditions of C_{55} and C_{66} were not satisfied. In this case none of the dopants we used could improve the mechanical stability of $Ni_{0.3}Mn_{0.5}Co_{0.2}O_2$. We further note that Nb-doped $Ni_3Mn_5Co_2CO_3$ has the highest shear modulus value (1134.05 GPa), indicating highest resistance when compared to $Ni_3Mn_5Co_2O_2$, $Ni_3Mn_5Co_2CO_3$, F-doped $Ni_{0.3}Mn_{0.5}Co_{0.2}CO_3$, F-doped $Ni_{0.3}Mn_{0.5}Co_{0.2}O_2$, Ti-doped $Ni_{0.3}Mn_{0.5}Co_{0.2}O_2$, Ti-doped $Ni_{0.3}Mn_{0.5}Co_{0.2}CO_3$, Nb-doped $Ni_{0.3}Mn_{0.5}Co_{0.2}O_2$, Cr-doped $Ni_{0.3}Mn_{0.5}Co_{0.2}O_2$ and Cr-doped $Ni_{0.3}Mn_{0.5}Co_{0.2}CO_3$ respectively. It is interesting to note that the shear modulus is greater than bulk modulus in $Ni_{0.3}Mn_{0.5}Co_{0.2}O_2$, Ti-doped $Ni_{0.3}Mn_{0.5}Co_{0.2}O_2$ and Nb-doped $Ni_{0.3}Mn_{0.5}Co_{0.2}CO_3$. This means that $Ni_{0.3}Mn_{0.5}Co_{0.2}O_2$, Ti-doped $Ni_{0.3}Mn_{0.5}Co_{0.2}O_2$ and Nb-doped $Ni_{0.3}Mn_{0.5}Co_{0.2}CO_3$ have greater stiffness than the hardness and resistance to deformation, thus greater susceptibility cracks when subjected under pressure. In the other systems, the bulk is greater than the shear modulus implying that shear modulus is the parameter limiting stability. The Young modulus (E) which determines stiffness of materials, showed that Nb-doped $Ni_{0.3}Mn_{0.5}Co_{0.2}CO_3$ possesses greater stiffness over other structures respectively.

In order to determine the brittleness and ductility nature of our structures, we have calculated their B/G ratio as proposed by Pugh. We note that B/G ratio is greater than 1.75 for $Ni_{0.3}Mn_{0.5}Co_{0.2}CO_3$, F-doped $Ni_{0.3}Mn_{0.5}Co_{20.2}CO_3$, F-doped $Ni_{0.3}Mn_{0.5}Co_{0.2}O_2$, Ti-doped $Ni_{0.3}Mn_{0.5}Co_{0.2}CO_3$ and Cr-doped $Ni_{0.3}Mn_{0.5}Co_{0.2}CO_3$ suggesting ductility (i.e. the ability to bend without deformation). On the other hand, the Pugh ratio values for $Ni_{0.3}Mn_{0.5}Co_{0.2}O_2$, Ti-doped $Ni_{0.3}Mn_{0.5}Co_{0.2}O_2$, Nb-doped $Ni_{0.3}Mn_{0.5}Co_{0.2}O_2$, Nb-doped $Ni_{0.3}Mn_{0.5}Co_{0.2}CO_3$ and Cr-doped $Ni_{0.3}Mn_{0.5}Co_{0.2}O_2$ are less than 1.75, suggesting brittleness (i.e. structural deformation after bending).

The vibrational properties for $Ni_{0.3}Mn_{0.5}Co_{0.2}CO_3$, $Ni_{0.3}Mn_{0.5}Co_{0.2}O_2$ and their doped systems were determined by calculating the phonon dispersion curves. The phonon dispersion curve for $Ni_{0.3}Mn_{0.5}Co_{0.2}CO_3$ show no soft modes or negative vibrational branches indicating vibrational stability. On the other hand, we note that the phonon dispersion curve for $Ni_{0.3}Mn_{0.5}Co_{0.2}O_2$ shows soft modes or negative vibrations in the high Brillouin zone indicating vibrational instability. For the doped systems, we note that fluorine doped $Ni_{0.3}Mn_{0.5}Co_{0.2}CO_3$ and titanium doped $Ni_{0.3}Mn_{0.5}Co_{0.2}CO_3$ shows no soft modes indicating vibrational stability, while on the other hand the fluorine doped $Ni_{0.3}Mn_{0.5}Co_{0.2}O_2$, titanium doped $Ni_{0.3}Mn_{0.5}Co_{0.2}O_2$ and niobium doped $Ni_{0.3}Mn_{0.5}Co_{0.2}O_2$ shows negative vibrations indicating vibrational instability.

We further used the UNCLE code to build a ternary phase whereby Ni and Co were doped on $MnCO_3$ structure to generate new phases. Cluster expansion generated new phases in Ni-rich side and Mn-rich side. We note that all the generated phases were in the negative energy of formations side (miscible constituent) which indicate thermodynamic stability. The predicted phases in the Mn-rich side were as follows: $Ni_{0.3}Mn_{0.5}Co_{0.17}CO_3$, $Ni_{0.17}Mn_{0.67}Co_{0.17}CO_3$, $Ni_{0.13}Mn_{0.75}Co_{0.13}CO_3$, $Ni_{0.17}Mn_{0.84}Co_{0.17}CO_3$ and $Ni_{0.13}Mn_{0.87}Co_{0.13}CO_3$. We further calculated their first principles to determine their stability properties. The heats of formation for all the predicted phases indicated that all phases were thermodynamically stable with the stability trend as follow: $Ni_{0.13}Mn_{0.87}Co_{0.13}CO_3$ > $Ni_{0.13}Mn_{0.75}Co_{0.13}CO_3$ > $Ni_{0.17}Mn_{0.84}Co_{0.17}CO_3$ > $Ni_{0.17}Mn_{0.67}Co_{0.17}CO_3$ > $Ni_{0.3}Mn_{0.5}Co_{0.17}CO_3$. Their density of states showed that all the predicted phases revealed either a semiconductor or metallic behaviour since some spin up were found to be semiconductors while spin down were found to be metallic and vice versa, which is an indication of a good electronic conductors.

We also calculated their elastic constants to determine their mechanical properties. We found that $Ni_{0.17}Mn_{0.67}Co_{0.17}CO_3$, $Ni_{0.17}Mn_{0.8}Co_{0.17}CO_3$ and $Ni_{0.13}Mn_{0.87}Co_{0.13}CO_3$ phases satisfied the triclinic stability conditions which indicate mechanical stability. On the other hand, $Ni_{0.3}Mn_{0.5}Co_{0.17}CO_3$ and $Ni_{0.13}Mn_{0.75}Co_{0.13}CO_3$ were not satisfying all the stability conditions indicating mechanical instability. Furthermore, Pugh's ratio suggests brittleness if (B/G<1.75) and ductility if (B/G>1.75). Hence, $Ni_{0.3}Mn_{0.5}Co_{0.17}CO_3$ and $Ni_{0.13}Mn_{0.75}Co_{0.13}CO_3$ shows the Pugh ratio being < 1.75 which depicts brittleness while $Ni_{0.17}Mn_{0.67}Co_{0.17}CO_3$, $Ni_{0.17}Mn_{0.8}Co_{0.17}CO_3$ and $Ni_{0.13}Mn_{0.87}Co_{0.13}CO_3$ depicts ductility.

We also calculated their phonon dispersion curves to determine the vibrational stability. We note that the phonon dispersion curve for $Ni_{0.3}Mn_{0.5}Co_{0.17}CO_3$, $Ni_{0.17}Mn_{0.67}Co_{0.17}CO_3$ and $Ni_{0.17}Mn_{0.8}Co_{0.17}CO_3$ shows positive frequencies in the high Brillouin zone implying vibrational stability, while on the other hand the phonon dispersion curves for $Ni_{0.13}Mn_{0.75}Co_{0.13}CO_3$ and $Ni_{0.13}Mn_{0.87}Co_{0.13}CO_3$ display negative frequency phonon branches (here referred to as soft modes) indicating vibrational stability. We further used the same cluster expansion file to plot ternary phase diagram for $NiMnCO_3$ structure. We note that only Ni-rich phases were generated and were not explored by means of calculating their First principles calculations as this study our focus was only on the Mn-rich side. However, the generated Ni-rich phases can be tested at laboratory for those working on Ni-rich NMC's as cathodes for lithium ion batteries. The computational results indicate that when comparing $NMCCO_3$ with $NMCO_2$, we found that $NMCCO_3$ structures performed much better than $NMCO_2$ structures which now lead us to using the carbonate co-precipitation method instead of the hydroxide co-precipitation to synthesize our NMC's as cathodes for lithium ion batteries. Moreover, the Mn-rich phases predicted have never been studied before, which means this work could be used for bench-marking in the near future of studying batteries by testing these phases at the laboratory.

Lastly, the carbonate co-precipitation method was used to synthesize $LiNi_{0.33}Mn_{0.53}Co_{0.14}O_2$ and $Li_{1.2}Ni_{0.13}Mn_{0.54}Co_{0.13}O_2$ samples. For characterization, both samples were tested for thermal decomposition analysis using the TA instruments. The thermogravimetric analysis results revealed that both samples are thermally stable since their mass loss was above 600 ^oC, this is good news from an experimental point of view, as it is significantly above the elevated temperatures required during the fluorination procedures.

We further used the X-Ray diffraction using D8 advance diffractometer to determine the atomic arrangements and crystallographic phases of our samples, which were found to compare well with the experimental data. Furthermore, the Raman analysis for both samples was performed and it was revealed that the Raman spectra of our samples consist of highly overlapping bands of different transition metal ions, thus it is difficult to assign the exact band to each vibration mode. Scanning Electron Microscopy was also tested to determine the particle size and distribution for both samples which reveal the size range of NMC particles, whether they are agglomerated or dispersed, and their distribution across the sample. The results revealed a homogeneous particle distribution in each sample and the more distributed the sample, the more likely it is to incur during fluorination. So when considering thermal stability as well as morphological aspects, these candidate precursor materials seem to fulfil experimental requirements. From our results, it was observed that compounds with higher manganese content have greater stability which is sufficient for fluorination experiments. Moreover, the synchrotron beam of the Diamond light source was successfully used to determine the effect of fluorination in our samples. The x-ray absorption spectroscopy results at the pre-edge feature indicated that oxidation state does not change since the pre-edge peak for all our samples was at the same energy position. This was further confirmed by the Fourier transform EXAFS

which calculated the bond distances of atoms within the sample and they were all the same indicating no change in oxidation state.

6.2. Suggestions for Future Work

Among the energy storage materials that are currently on the market, lithium-ion batteries, which have the advantages of high working voltage, long cycle life, and environmental friendliness, have dominated the energy storage materials market since they first entered the commercial market in 1991. The development of cathode materials has gained a lot of attention as a result of pressing need for high energy density and high output power sources. So since Mn-rich NMC's gained attention as the promising cathode with high energy density for lithium ion batteries, we still have to study various Mn-rich phases and understand their stability properties.

From our results, few phases were generated using the universal cluster expansion. However, the phases were tested using first principles calculations, so for future work those phases can be tested in laboratory or experimentally to check their morphology, energy density and electrochemical properties. Moreover, since this study focused on the carbonate co-precipitation as the method, we can further use hydroxide co-precipitation method to compare the results from both methods. Furthermore, on the synchrotron results, since there was no change on the oxidation state of transition metals due to fluorination, we can further determine the impact of fluorination whilst cycling to check its influence on oxidation of the anions using the synchrotron based techniques.

6.3. Publications

1. M.T. Morukuladi, N.N. Ngoepe, M.C. Masedi, P.E. Ngoepe, “Transition metal carbonate precursors as cathode materials for lithium ion batteries: first principles study”, MATEC Web of Conferences, (2023), 388, 07013

2. M.T. Morukuladi, N.L. Lethole, M.C. Masedi, N.N. Ngoepe and P.E. Ngoepe, “Investigating stability properties for transition metal carbonate precursors using Universal cluster expansion technique (UNCLE) as cathodes for Li-ion batteries”, Journal of Materials Science and Engineering A (2024) 14, 26-33, Doi: 10.17265/2161-6213/2023.1-3.004.

6.4. Papers presented at conferences

1. M.T. Morukuladi, M.C. Masedi, N.N. Ngoepe and P.E. Ngoepe, “Exploring Mn-rich transition metal carbonate precursors as cathode materials for Li-ion batteries”, SAIP conference 2022

2. M.T. Morukuladi, M.C. Masedi, N.N. Ngoepe and P.E. Ngoepe, “Investigate the stability properties of MCO_3 (M: Ni, Co, Mn) precursors as cathodes for Li-ion batteries”, CHPC conference, 2022.

3. M.T. Morukuladi, M.C. Masedi, N.N. Ngoepe and P.E. Ngoepe, “Manganese rich transition metal carbonate precursors as future cathodes for Li-ion batteries”, FSA 2022.

4. M.T. Morukuladi, M.C. Masedi, N.N. Ngoepe and P.E. Ngoepe, “Synthesis of Mn-rich transition metal carbonate precursors as cathode materials for lithium ion batteries: Carbonate co-precipitation method”, SAIP conference 2023.

5. M.T. Morukuladi, M.C. Masedi, N.N. Ngoepe and P.E. Ngoepe, “Transition metal carbonate precursors as cathode materials for lithium ion batteries: First Principles Study”, RAPDASA 2023 conference proceedings.

6. M.T. Morukuladi, M.C. Masedi, N.N. Ngoepe and P.E. Ngoepe, “ Lithium and Manganese rich based materials as possible cathodes for high energy density Li-ion batteries”, CHPC 2023.

7. M.T. Morukuladi, M.C. Masedi, N.N. Ngoepe and P.E. Ngoepe, “Determining the effect of fluorination on the transition metals of $LiNMCO_2$ using synchrotron based techniques” CHPC 2024.

6.5. References

[1] M. Armand and J.M. Tarascon, “Researchers must find a sustainable way of providing the power our modern lifestyles demand,” *Building better batteries,* vol. 451, pp. pages 652–657, 2008.

[2] P.V. Kamat, “Lithium-ion batteries and beyond,” *ACS Publications,* vol. 4, pp. 2757-2759, 2019.

[3] Lyu, Y., Wu, X., Wang, K., Feng, Z., Cheng, T., Liu, Y., Wang, M., Chen, R., Xu, L., Zhou, J., Lu, Y., Guo, B., “An Overview on the Advances of $LiCoO_2$ Cathodes for Lithium-Ion Batteries(Review),” *Advanced Energy Materials,* vol. 11, pp. 11-100, 2021.

[4] L. Meng, G. Wang, K.W. See, Y. Wang, Y. Zhang, C. Zang, R. Zhou and B. Xie, “Document details - Large-Scale Li-Ion Battery Research and Application in Mining Industry,” *Journal of energies,* vol. 15, pp. 30-50, 2022.

[5] D. Deng, “Li-ion batteries: basics, progress, and challenges,” *Energy Science & Engineering,* vol. 3, pp. 230-300, 2015.

[6] M. Winter and R.J. Brodd, “ What Are Batteries, Fuel Cells, and supercapacitors,” *Chemical review,* vol. 10, p. 4245−4270, 2004.

[7] I. Hadjipaschalis, A. Poullikkas and V. Efthimiou, “Overview of current and future energy storage technologies for electric power applications,” *Renewable Sustainable Energy Review,* vol. 13, pp. 1513-1522, 2009.

[8] J.B. Goodenough and Y. Kim, “Challenges for Rechargeable Batteries,” *Chemial Materials,* vol. 22, p. 587−603, 2010.

[9] A. Manthiram, “A reflection on lithium-ion battery cathode chemistry,,” *Natural Communications,* vol. 11, pp. 15-50, 2020.

[10] A. Manthiram, J.C. Knight, S.T. Myung, S.M. Oh and Y.K. Sun, “Nickel-Rich and Lithium-Rich Layered Oxide Cathodes: Progress and Perspectives,” *Advanced Energy Materials,* vol. 6, pp. 15-30, 2016.

[11] J. Xu, F. Lin, M.M. Doeff and W. Tong, “A review of Ni-based layered oxides for rechargeable Li-ion batteries,” *Journal of Materials Chemistry A,* vol. 5, pp. 20-50, 2017.

[12] V.G. Choudhari, A.S. Dhoble and T.M. Sathe, “A review on effect of heat generation and various thermal management systems for lithium ion battery used for electric vehicle,” *Journal of Energy Storage,* vol. 32, pp. 2-10, 2020.

[13] N. Nitta, F. Wu, J.T. Lee and G. Yushin, “Li-ion battery materials: Present and future,” *Materials Today,* vol. 18, p. 252–264, 2015.

[14] K.C. Jiang, S. Xin, J.S. Lee, J. Kim, X.L. Xiao and Y.G. Guo, “Improved Kinetics of $LiNi_{1/3}Mn_{1/3}Co_{1/3}O_2$ Cathode Material through Reduced Graphene Oxide Networks,” *Physical Chemistry Chemical Physics,* vol. 14, pp. 2934-2939, 2012.

[15] M. Yoshio, R.J. Brodd and A. Kozawa, “Lithium Ion Batteries,” *Springer,* vol. 46, pp. 03873-04464, 2009.

[16] R.M. Salgado, F. Danzi, J.E. Oliveira, A. El-Azab, P.P. Camanho and M.H. Braga,, “he latest trends in electric vehicles batteries,” *Molecules,* vol. 26, pp. 30-100, 2021.

[17] Z. Qiu, Y. Zhang, X. Huang, J. Duan, D. Wang, G.P. Nayaka, X. Li and P. Dong, “Beneficial effect of incorporating Ni-rich oxide and layered over-lithiated oxide into high-energy-density cathode materials for lithium-ion batteries,” *Journal of Power Sources,* vol. 400, p. 341–349, 2018.

[18] U. Nisar, N. Muralidharan, R. Essehli, R. Amin, I. Belharouak, “aluation of surface coatings in high-energy density lithium-ion battery cathode materials,” *Energy Storage Materials,* vol. 38, p. 309–328, 2021.

[19] T.F. Yi, J. Mei and Y.R. Zhu,, “Key strategies for enhancing the cycling stability and rate capacity of $LiNi_{0.5}Mn_{1.5}O_4$ as high-voltage cathode materials for high power lithium-ion batteries,” *Journal of Power Sources,* vol. 316, p. 85–105, 2016.

[20] A. Chakraborty, S. Kunnikuruvan, S. Kumar, B. Markovsky, D. Aurbach, M. Dixit and D.T. Major, “ayered cathode materials for lithium-ion batteries: review of computational studies on $LiNi_{1-x-y}Co_xMn_yO_2$ and $LiNi_{1-x-y}Co_xAl_yO_2$,” *Chemical Materials,* vol. 32, p. 915–952, 2020.

[21] M. Malik, K.H. Chan and G. Azimi, “Review on the synthesis of $LiNi_xMn_yCo_{1-x-y}O_2$ (NMC) cathodes for lithium-ion batteries,” *Materials Today Energy,* vol. 20, pp. 30-70, 2022.

[22] C. Tian, F. Lin and M.M. Doeff, “Electrochemical characteristics of layered transition metal oxide cathode materials for lithium ion batteries: Surface, bulk behavior, and thermal properties,” *Accounts of Chemical Research,* vol. 51, p. 89–96, 2017.

[23] S. Aryal, J.L. Durham, A.L. Lipson, K.Z. Pupek and O. Kahvecioglu , “Roles of Mn and Co in Ni-rich layered oxide cathodes synthesized utilizing a Taylor Vortex Reactor,” *Electrochim. Acta,* vol. 391, pp. 138-929, 2021.

[24] C. Liang, F. Kong, R.C. Longo, K.C. Santosh, J.S. Kim, S.H. Jeon, S.A. Choi and K. Cho , “Unraveling the origin of instability in Ni-rich $LiNi_{1-2x}Co_xMn_xO_2$ (NCM) cathode materials.,” *Journal of Physical Chemistry C,* vol. 120, p. 6383–6393, 2016.

[25] S.G. Booth, A.J. Nedoma, N.N. Anthonisamy, P.J. Baker, R. Boston, H. Bronstein, S.J. Clarke, E.J. Cussen, V. Daramalla, M. de Volder, S.E. Dutton, V. Falkowski, N.A. Fleck, H.S. Geddes, N. Gollapally, A.L. Goodwin, J.M. Griffin, A.R. Haworth, M.A. Hayward, “Perspectives for next generation lithium-ion battery cathode material,” *Applied Materials,* vol. 9, p. 10920, 2021.

[26] X. Miao, H. Ni, H. Zhang, C. Wang, J. Fang, G. Yang,, “Li_2ZrO_3-coated $0.4Li_2MnO_3 \cdot 0.6LiNi_{1/3}Co_{1/3}Mn_{1/3}O_2$ for high performance cathode material in lithium-ion battery,” *Journal of Power Sources,* vol. 264, p. 147–154, 2014.

[27] C. Li, H.P. Zhang, L.J. Fu, H. Liu, Y.P. Wu, E. Rahm, R. Holze and H.Q. Wu, “athode materials modified by surface coating for lithium ion batteries,” *Electrochim.Acta,* vol. 51, p. 3872–3883, 2006.

[28] I. Meatza, M.I. Landa, I.S. Sananes, B. Eguia, O. Bondarchuk, P.S. Lijo and T. Roto, ". Influence of the Ambient Storage of $LiNi_{0.8}Mn_{0.1}Co_{0.1}O_2$ Powder and Electrodes on the Electrochemical performance in Li-ion Technology," *Batteries*, vol. 8, pp. 79-90, 2022.

[29] L. Wang, B. Huang, W. Xiong, M. Tong, H. Li, S. Xiao, Q. Chen, Y. Li and J. Yang, "proved solid-state synthesis and electrochemical properties of," *Journal of Alloys Compounds*, vol. 844, p. 15603, 2020.

[30] P. Yue, Z. Wang, W. Peng, L. Li, H. Guo, X. Li, Q. Hu and Y. Zhang, "eparation and electrochemical properties of submicron $LiNi_{0.6}Co_{0.2}Mn_{0.2}O_2$ as cathode material for lithium ion batteries," *Scripta Materialia,* vol. 65, p. 1077–1080, 2011.

[31] B. Wu, J. Bi, Q. Liu, D. Mu, L. Wang, J. Fu and F. Wu, "Role of current density in the degradation of $LiNi_{0.6}Co_{0.2}Mn_{0.2}O_2$ cathode material," *Electrochimica.Act,* vol. 298, p. 609–615, 2019.

[32] W. Ahn, S.N. Lim, K.N. Jung, S.H. Yeon, K.B. Kim, H.S. Song and K.H. Shin, "ombustion-synthesized $LiNi_{0.6}Mn_{0.2}Co_{0.2}O_2$ as cathode material for lithium ion batteries," *Journal of Alloys Compound,* vol. 609, p. 143–149, 2014.

[33] D. Zhuang and M.Z. Bazant , "Theory of layered-oxide cathode degradation in Li-ion batteries by oxidation-induced cation disorder," *Journal of Electrochemical Society*, vol. 169, p. 100536, 2022.

[34] M. Evertz, F. Horsthemke, J. Kasnatscheew, M. Börner, M. Winter and S. Nowak , "Unraveling transition metal dissolution of $Li_{1.04}Ni_{1/3}Co_{1/3}Mn_{1/3}O_2$ (NCM 111) in lithium ion full cells by using the total reflection X-ray fluorescence technique," *Journal of Power Sources*, vol. 329, p. 364–371, 2016.

[35] T. Kim, L.K. Ono, N. Fleck and S.R. Raga , “Transition metal speciation as a degradation mechanism with the formation of a solid-electrolyte interphase (SEI) in Ni-rich transition metal oxide cathodes.,” *Journal of Materials Chemistry A,* vol. 6, p. 14449–14463, 2018.

[36] H.R. Kim, S.W. Woo, J.H. Kim, W. Cho and Y.K. Kim , “Capacity fading behavior of Ni-rich layered cathode materials in Li-ion full cells.,” *Journal of Electroanal Chemistry,* vol. 782, p. 168–173, 2016.

[37] J. Cui, X. Ding, D. Luo, H. Xie, Z. Zhang, B. Zhang, F. Tan, C. Liu and Z. Lin , “Effect of cationic uniformity in precursors on Li/Ni mixing of Ni-rich layered cathodes,” *Energy Fuels,* vol. 35, p. 1842–1850, 2021.

[38] I. Hwang, C.W. Lee, J.C. Kim, and S. Yoon, “Particle size effect of Ni-rich cathode materials on lithium ion battery performance,” *Materials Research Bulletin,* vol. 47, p. 73–78, 2012.

[39] Y. Xia, J. Zheng, C. Wang and M. Gu, “Designing principle for Ni-rich cathode materials with high energy density for practical applications,” *Nano Energy,* vol. 49, p. 434–452, 2018.

[40] A. Ritchie and W. Howard, “Recent developments and likely advances in lithium-ion batteries,” *Journal of Power Sources,* vol. 162, p. 809–812, 2006.

[41] J. Wang, B. Qiu, H. Cao, Y. Xia and Z. Liu, “Electrochemical properties of $Li[Li_{1/3}Mn_{2/3}]O_{2-0.4}LiNi_xMn_yCo_{1-x-y}O_2$ cathode materials for lithium-ion batteries,” *Journal of Power Sources,* vol. 218, p. 128–133, 2012.

[42] D. Mohanty, A.S Sefat, S. Kalnaus, J. Li, R.A. Meisner, E.A Payzant, D.P. Abraham, D.L Wood and C. Daniel, “ Investigating phase transformation in the

$Li_{1.2}Co_{0.1}Mn_{0.55}Ni_{0.15}O_2$ lithium-ion battery cathode during high-voltage hold (4.5 V) via magnetic, X-ray diffraction and electron microscopy studies.," *Journal of Materials Chemistry A,* vol. 1, p. 6249, 2013.

[43] Z. Lu, L.Y Beaulieu, R.A Donaberger, C.L Thomas and J.R. Dahn, "Synthesis, Structure, and Electrochemical Behavior of $Li[Ni_xLi_{1/3-2x/3}Mn_{2/3-x/3}]O_2$," *Journal of Electrochemical Society,* vol. 149, p. A778, 2002.

[44] G. Hautier, A. Jain, S.P. Ong, "From the computer to the laboratory: materials discovery and design using first-principles calculations," *Journal of Materials Science,* vol. 47, p. 7317–7340, 2012.

[45] K. Park, J.H. Park, S.G. Hong, B. Choi, S.W. Seo, J.H. Park, K. Min, "Enhancement in the electrochemical performance of zirconium/phosphate bi-functional coatings on $LiNi_{0.8}Co_{0.15}Mn_{0.05}O_2$ by the removal of Li residuals," *Journal of Physical Chemistry,* vol. 18, p. 29076–29085, 2016.

[46] Y.S. Meng, M.E. Arroyo-De Dompablo, "Recent advances in first principles computational research of cathode materials for lithium-ion batteries,," *Accounts of Chemical Research,* vol. 46, p. 1171–1180, 2013.

[47] T.N. Vu, S.K. Nayak, N.T.T. Nguyen, S.P. Alpay, H. Tran, "Atomic configurations for materials research: a case study of some simple binary compounds," *AIP Advances,* vol. 11, pp. 150-300, 2021.

[48] Y.S. Meng, M.E. Arroyo-De Dompablo, "First principles computational materials design for energy storage materials in lithium ion batteries," *Energy Environmental Science,* vol. 2, p. 589–609, 2009.

[49] . Jain, Y. Shin, K.A. Persson, “Computational predictions of energy materials using density functional theory,” *Nature Reviews Materials,* vol. 1, pp. 190-400, 2016.

[50] F Wu, J Maier and Y Yu, “Guidelines and trends for next-generation rechargeable lithium and lithium-ion batteries,” *Chemical Society Reviews,* vol. 49, pp. 1569-1614, 2020.

[51] M.D. Bhatt and C. O'Dwyer, “ Recent progress in theoretical and computational investigations of Li-ion battery materials and electrolytes,” *Physical chemistry chemical physics,* vol. 17, pp. 4799-4844, 2015.

[52] V. Aravindan, K. Karthikeyan, K.S. Kang, W.S. Yoon, W.S. Kim and Y.S. Lee, “Influence of carbon towards improved lithium storage properties of Li 2 MnSiO4 cathodes,” *Journal of Materials Chemistry,* pp. 2470-2475, 2011.

[53] N. Nitta, F. Wu, J.T. Lee and G. Yushin, “Li-ion Battery Materials: Present and Future,” *Materialstoday,* vol. 18, pp. 252-264, 2015.

[54] A. Manthiram,, “ reflection on lithium-ion battery cathode chemistry,” *Nature Communications,* vol. 11, pp. 165-285, 2020.

[55] J.M. Tarascon and M. Armand,, “Issues and challenges facing rechargeable lithium batteries,” *Nature,* vol. 414, p. 359–67, 2001.

[56] A. Kraytsberg, Y. Ein-Eli, A. Kraytsberg, Y. Ein-Eli, “A review of 5 volt cathode materials for advanced lithium-ion batterie,” *Advanced Energy Materials* , vol. 2, p. 922–939, 2012.

[57] J. Li, S. Li and S. Xu, “Synthesis and Electrochemical properties of $LiNi_{0.5}Mn_{1.5}O_4$ cathode materials with Cr3+ and F-composite doping for lithium-ion batteries,” *Nanoscale research letters,* vol. 12, pp. 116-217, 2017.

[58] Y. Zhang, Q.Y. Huo, P.P. Du, L.Z. Wang, A.Q. Zhang, Y.H. Song, Y. Lv, G.Y. Li, "Advances in new cathode material $LiFePO_4$for lithium-ion batteries," *Synthetic Metals* , vol. 162, p. 1315–1326, 2012.

[59] Y. Liu, Y. Gao and A. Dou, "Influence of Li content on the structure and electrochemical performance of $Li_{1+x}Ni_{0.25}Mn_{0.75}O_{2.25+x/2}$ cathode for Li-ion battery," *Journal of power sources,* vol. 248, pp. 679-684, 2014.

[60] P. Guan, L. Zhou, Z. Yu, Y. Sun, Y. Liu, F. Wu, Y. Jiang and D. Chu, "Recent progress of surface coating on cathode materials for high-performance lithium-ion batteries," *Journal of Energy Chemistry,* vol. 43, pp. 220-235, 2020.

[61] B. Xu, D.N. Qian, Z.Y. Wang and Y.S.L. Meng, "Recent progress in cathode materials research for advanced lithium ion batteries," *Materials science and engineering R,* vol. 73, pp. 51-65, 2012.

[62] A.A. Ghany, K. Zaghib, F. Gendron, A. Mauger and C.M. Julien, "Structural, magnetic and electrochemical properties of $LiNi_{0.5}Mn_{0.5}O_2$ as positive electrode for Li-ion batteries," *Electrochimica Acta,* vol. 52, pp. 4092-4100, 2007.

[63] Z. Liu, A. Yu, and J. Y. Lee, "Synthesis and characterization of $LiNi_{1-x-y}Co_xMn_yO_2$ as the cathode materials of secondary ithium batteries," *Journal of Power Sources,* Vols. 81-82, pp. 416-419, 1999.

[64] P. Rozier and J.M. Tarascon, "Review—Li-Rich Layered Oxide Cathodes for Next-Generation Li-Ion Batteries: Chances and Challenges," *Journal of The Electrochemical Society,* vol. 162, pp. 2490-2499, 2015.

[65] M. Li, J. Lu, Z. Chen and K. Amine, "30 years of lithium ion batteries," *Advanced Materials,* vol. 30, pp. 30-70, 2018.

[66] N. Nitta, F. Wu, J.T. Lee andd G. Yushin, “Li-ion battery materials: present and future,” *Materials Today,* vol. 18, pp. 252-264, 2015.

[67] B. Dunn, H. Kamath and J.M. Tarascon, “Electrical Energy Storage for the Grid: A Battery of Choices,” *Science,* vol. 334, pp. 928-935, 2011.

[68] J.S. Won, S.E. Lee, J.H. Lim, J. Choi, and J. Kim, “. Performance and Life Degradation Characteristics Analysis of NCM LIB for BESS,” *Electronics,* vol. 7, pp. 50-150, 2018.

[69] L. Xu, F. Zhou, B. Liu, H. Zhou, Q. Zhang, J. Kong and Q. Wang, “Progress in Preparation and Modification of $LiNi_{0.6}Mn_{0.2}Co_{0.2}O_2$ Cathode Material for High Energy Density Li-Ion Batteries,” *International Journal of Electrochemistry*, vol. 2018, pp. 1-12, 2018.

[70] M. Malik, K.H Chan and G. Azimi , “eview on the synthesis of $LiNi_xMn_yCo_{1-x-y}O_2$ (NMC) cathodes for lithium-ion batteries,” *Materials Today Energy,* vol. 28, p. 101066, 2022.

[71] J. Ma, P. Hu, G. Cui and L. Chen, “Surface and interface issues in spinel LiNi0.5Mn1.5O4: Insights into a potential cathode material for high energy density lithium ion batteries,” *Chemical Materials,* vol. 28, p. 2016, 3578–3606.

[72] L. Simonelli, A. Sorrentino, C. Marini, N. Ramanan, D. Heinis, W. Olszewski, A. Mullaliu, A.; Birrozzi, N. Laszczyn-ski and M. Giorgetti , “ole of Manganese in Lithium-and Manganese-Rich Layered Oxides Cathodes.,” *Journal of Physical Chemistry Letters,* vol. 10, p. 3359–3368, 2019.

[73] S. Zhang, J. Ma, Z. Hu, G. Cui and L. Chen, “. Identifying and addressing critical challenges of high-voltage layered ternary oxide cathode materials,” *Chemical Materials,* vol. 31, p. 6033–6065, 2019.

[74] I. Hwang, C.W. Lee, J.C. Kim and S. Yoon, " Particle size effect of Ni-rich cathode materials on lithium ion battery performance," *Materials Research Bulletin* , vol. 47, p. 73–78., 2012.

[75] A.K. Thapa, B.W. Lavery, R.K. Hona, N. Sapkota, M.K. Koralalage, A. A DENIRAN, B.P. Ajayi, M.A. Zain, H.Wang, T. Druffel, J.B. Jasinki, G.U. Sumanasekera, M.K. Sunkara and M. Yoshio, "Mn-Rich NMC Cathode for Lithium-Ion Batteries at High-Voltage Operation," *Energies,* vol. 15, pp. 1-14, 2022.

[76] J.J. Liu, J.Wang, Y.G. Xia, X.F. Zhou, Y. Saixi and Z.P. Liu, "Synthesis and Electrochemical Performance of $Li_{1+x}Ni_{0.5}Mn_{0.3}Co_{0.2}O_{2+delta}$ (0 <= x <= 0.15) Cathode Materials for Lithium-ion Batteries," *Materials Research Bulletin,* vol. 47, pp. 807-812, 2012.

[77] P. Mohan and G.P. Kalaignan, "Structure and Electrochemical Performance of $LiV_x Mn_{2-x} O_4$ ($0 \leq x \leq 0.20$) Cathode Materials for Rechargeable Lithium ion Batteries," *Ionics,* vol. 19, pp. 895-900, 2014.

[78] K.S. Lee, S.T. Myung, J.S. Moon and Y.K. Sun, "Particle Size Effect of $Li[Ni_{0.5}Mn_{0.5}]O_2$ Prepared by Co-Precipitation," *Electrochimica Acta,* vol. 53, pp. 6033-6037, 2008.

[79] G. Koenig, G. Zhou and K.Amine, "Growth Mechanism of $Ni_{0.3}Mn_{0.7}CO_3$ Precursor for High Capacity Li-ion," *Journal of Materials Chemistry,* vol. 21, pp. 9290-9300, 2011.

[80] N. Yabuuchi and T. Ohzuku, "Novel lithium insertion material of $LiCo_{1/3}Ni_{1/3}Mn_{1/3}O_2$ for advanced lithium-ion batteries," *Journal of Power Sources,* vol. 119, p. 171–174, 2003.

[81] J.H. Lim, H. Bang, K.S. Lee, K. Amine and Y.K Sun, “Electrochemical characterization of Li_2MnO_3–$Li[Ni_{1/3}Co_{1/3}Mn_{1/3}]O_2$ $LiNiO_2$ cathode synthesized via co-precipitation for lithium secondary batteries,” *Journal of Power Sources,* vol. 189, p. 571–575, 2009.

[82] T.H. Cho, S.M. Park, M. Yoshio, T. Hirai and Y. Hideshima, “Effect of Synthesis Condition on the Structural and Electrochemical Properties of $Li[Ni_{1/3}Mn_{1/3}Co_{1/3}]O_2$ Prepared by Carbonate Co-Precipitation Method,” *Journal of Power Sources,* vol. 142, pp. 306-312, 2005.

[83] R.C. Longo, K.C. Santosh, F. Kong and M.S. Park, “Phase Stability of Li-Mn-O Oxides as Cathode Materials for Li-ion Batteries: Insights from ab initio Calculations,” *Physical Chemistry Chemical Physics,* vol. 16, pp. 11233-11242, 2014.

[84] D.H. Kwon, J. Lee, N. Artrith, H. Kim, L. Wu, Z. Lun, Y. Tian, Y. Zhu, and G. Ceder, “The Impact of Surface Structure Transformations on the Performance of Li-Excess Cation-Disordered Rocksalt Cathodes,” *Cell Reports Physical Science,* vol. 1, p. 100187, 2020.

[85] T.Y. Huang, M. J. Crafton, Y. Yue, W. Tong, and B. D. McCloskey, “Deconvolution of intermixed redox processes in Ni-based cation-disordered Li-excess cathodes,” *Energy & Environmental Science* , vol. 14, pp. 1553-1562 , 2021.

[86] H. Kim, S.B. Kimm, D.H. Park and K.W. Park, “Fluorine-Doped $LiNi_{0.8}Mn_{0.1}Co_{0.1}O_2$ Cathode for High-Performance Lithium-Ion Batteries,” *Energies,* vol. 13, pp. 1-10, 2020.

[87] F. Kong, C. Liang, R.C. Longo, D.H. Yeon, Y. Zheng, J.H. Park, S.G. Doo, K. Cho, “Conflicting Roles of Anion Doping on the Electrochemical Performance of Li-Ion Battery Cathode Materials.,” *Chemical Materials,* vol. 28, p. 6942–6952, 2016.

[88] J.O. Binder, S.P. Culver, R. Pinedo, D.A. Weber, M.S. Friedrich, K.I. Gries, K Volz, W.G Zeier, J. Janek, "Investigation of Fluorine and Nitrogen as Anionic Dopants in Nickel-Rich Cathode Materials for Lithium-Ion Batteries," *ACS Applied Material Interfaces*, vol. 10, p. 44452–4446, 2018.

[89] U. Nisar, R. Amin, A. Shakoor, R. Essehli, S. Al-Qaradawi, R. Kahraman and I. Belharouak, "Synthesis and Electrochemical Characterization of Cr-doped Lithium-rich $Li_{1.2}Ni_{0.16}Mn_{0.56}Co_{0.08-x}Cr_xO_2$ Cathodes," *OSTI.GOV (.gov),* vol. 12, pp. 12-100, 2018.

[90] F. Bizzotto, W. Dachraoui, R. Grissa, W. Zhao, F. Pagani, E. Querel, R.S. Kuhnel and C. Battaglia, "Modification of NMC811 with titanium for enhanced cycling and high-voltage stability," *Electrochimica Acta,* vol. 462, p. 142758, 2023.

[91] Z. Yang, W. Xiang, Z. Wu, F. He, J. Zhang, Y. Xiao, B. Zhong and X. Guo, "Effect of niobium doping on the structure and electrochemical performance of $LiNi_{0.5}Co_{0.2}Mn_{0.3}O_2$ cathode materials for lithium ion batteries," *Ceramics International,* vol. 43, pp. 3866-3872, 2017.

[92] M. Isabel and A. Camacho, "Influence of the Hubbard U Parameter on the Structural, Electronic, Magnetic, and Transport Properties of Cr/Fe/Zr-Based MBenes," *ACS Omega.,* vol. 8, p. 45003–45012, 2023.

[93] W. Yu, C. Jin, and A. Kohlmeyer, "First principles calculation of phonon dispersion, thermodynamic properties and B1-to-B2 phase transition of lighter alkali hydrides.," *Journal of Physics Condensed Matter,* vol. 19, p. 086209 , 2007.

[94] W. Kohn and P. Hohenberg, "Inhomogeneous Electron Gas," *Physical Review,* vol. 136, p. 864–871, 1964.

[95] P. Hohenberg and W. Kohn, “Inhomogeneous electron gas,” *Physical Review,* vol. 136, pp. 871-880, 1964.

[96] L. H. Thomas, “The Calculation of Atomic Fields,” *Mathematical Proceedings of the Cambridge Philosophical Society,* vol. 23, pp. 542-548, 1927.

[97] D.R. Hartree and V.A. Fock, “The Wave Mechanics of an Atom with a Non-Coulomb Central Field. Part I. Theory and Methods,” *Mathematical Proceedings of the Cambridge Philosophical Society,* vol. 24, pp. 89-110, 1928.

[98] J.C. Slater, “A Generalized Self-Consistent Field Method,” *Physical Review,* vol. 81, pp. 385-395, 1951.

[99] D.M. Hanson, E. Harvey, R. Sweeney and T.J. Zielinski, “Quantum States of Atoms and Molecules,” *Chemistry LibreTexts,* vol. 10, pp. 50-80, 2019.

[100] P. W. Ayers, S. Golden and M. Levy, “Generalizations of the Hohenberg-Kohn Theorem: I. Legendre Transform Constructions of Variational Principles for Density Matrices and Electron Distrbution Functions,” *Journal of Chemical Physics,* vol. 124, pp. 054101-054107, 2006.

[101] W. Kohn and L. Sham, “Self-Consistent Equations Including Exchange and Correlation Effects,” *Physical Review Journals Archive,* vol. 140, pp. 1133-1248, 1965.

[102] M. Chakraverty, H.M. Kittur and P.A. Kumar, “First Principle Simulations of Various Magnetic Tunnel Junctions for Applications in Magnetoresitive Random Access Memories,” *IEEE Transactions on Nanotechnology,* vol. 12, pp. 971-985, 2013.

[103] B. J. Alder and D.M. Ceperley, “Ground State of the Electron Gas by a Stochastic Method,” *Physical Review Letters,* vol. 45, p. 566–569, 1980.

[104] K. Horn and M. Scheffler, “In Electronic Structure,” *Handbook of Surface Science,* vol. 2, pp. 1-1058, 2000.

[105] P. J Perdew, “Density-Functional Approximation for the Correlation Energy of the Inhomogeneous Electron Gas,” *Physical Review B,* vol. 34, p. 7406–7809, 1986.

[106] A. D. Becke, “Density-Functional Exchange-Energy Approximation with Correct Asymptotic Behavior,” *Physical Review,* vol. 38, p. 3098–3100, 1988.

[107] Y. Wang and J.P. Perdew, “Accurate and Simple Analytic Representation of the Electron-Gas Correlation Energy,” *Physical Review,* vol. 45, p. 13244–13249, 1992.

[108] J.P. Perdew, K. Burke and M. Ernzerhof, “Generalized Gradient Approximation Made Simple,” *Physical Review Letters,* vol. 77, pp. 3865-3880, 1996.

[109] E. Wimmer and J. Andzelm, “Density Functional Gaussian-type-Orbital Approach to Molecular Geometries, Vibrations and Reaction Energies,” *The journal of Chemical Physics,* vol. 96, pp. 1280-1289, 1992.

[110] M. Meyer and V. Pontikis, “Application of Computer Simulation in Material Science,” *Applied Mechanics and Materials,* vol. 112, pp. 257-321, 1991.

[111] M. L. Cohen and M. T. Yin, “Theory of Lattice-Dynamical Properties of Solids: Application to Si and Ge,” *Physical Review B,* vol. 26, pp. 3259-3270, 1982.

[112] M. Massimi, “Pauli's Exclusion Principle: The Origin and Validation of a Scientific Principle,” *Cambridge,* vol. 5, pp. 437-590, 2016.

[113] D.R. Hamman, M. Schluter and C. Chiang, “Norm Conserving Pseudopotentials,” *Physical Review Letters,* vol. 43, pp. 1494-1499, 1979.

[114] M. Suzuki and I. S. Suzuki, “Lecture Note on Solid State Physics,” *ResearchGate,* pp. 13902-6000, 2006.

[115] D. J. Cohen and M. L. Chadi, “Special Points in the Brillouin Zone,” *Physical Review,* vol. 8, p. 5747–5753, 1973.

[116] H.J. Monkhorst and J.D. Pack, “Special Points for Brillouin-zone Integrations,” *Physical Review,* vol. 13, pp. 5188-5190, 1976.

[117] P. P. Pratapa and P. Suryanarayana, “Restarted Pulay mixing for efficient and robust acceleration of fixed-point iterations,” *Chemical Physics Letters,* vol. 635, pp. 69-74, 2015.

[118] P. E. Blöchi, “Projector Augmented-Wave Method,” *Physical Review,* vol. 50, pp. 17953-17980, 1994.

[119] P.E. Blochl, “ Projector Augmented-Wave Method,” *Physical Review ,* vol. 50, pp. 17953-17979, 1994.

[120] K.Parlinski, “Molecular Dynamics Simulation of Incommensurate Phases,” *Computer Physics Reports,* vol. 8, pp. 153-219, 1988.

[121] M. Zbiri, R. Mittal, S. Rols, Y. Su, Y. Xiao, H. Schober, S.L.Chaplot, M.R. Johnson, T. Chatterji, Y. Inoue, S. Matsuishi, H. Hosono and T.Brueckel, “Magnetic Lattice Dynamics of the Oxygen-free FeAs,” *Journal for Physical Review,* vol. 22, pp. 315-701, 2010.

[122] M.F. Lu, C.P. Zhou, Q.Q. Li, C. Zhang and H.F. Shi, “Effects of B site Doping on Electronic Structures of InNbO4 based on Hybrid Density Functional Calculations,” *Materials Science and Engineering,* vol. 292, pp. 1757-8992, 2017.

[123] I. Harald and H. Luth, “An Introduction to Principles of Materials Science 2nd edition,” *Solid State Physics,* vol. 2, pp. 541-560, 1996.

[124] Q. Li, S. Danilkin, G. Deng, Z. Li, R.L. Withers, Z. Xu and Y. Liu, “Soft Phonon Modes and Diffuse Scattering in relaxor ferroelectrics,” *Journal of Materiomics,* vol. 4, pp. 345-352, 2018.

[125] M.J. Mehl, B.M. Klein and D.A. Papaconstantopoulos, “First Principle Calculation of Elastic Properties of Metals,” *Naval Research Laboratory,* vol. 4, pp. 589-598, 1993.

[126] L.L Boyer and M.J. Mehl, “Getting off the Bain path: Are there any Metastable States of Cubic Elements?,” *Physical Review,* vol. 43, pp. 9498 - 9502, 1991.

[127] P. Saxeb and Y. Le Pagea, “Ab Initio vs Literature Stiffness Values for Ga: A Caveat about Crystal Settings,” *Physica B: Condensed Matter,* vol. 307, pp. 1-308, 2001.

[128] F. Mouhat and F.X. Coudert, “Necessary and Sufficient Elastic Stability Conditions in Various Crystal Systems,” *Physical Review,* vol. 90, pp. 104-224, 2014.

[129] Q. Wu, B. He, T. Song, J. Gao and S. Shi, “Cluster Expansion Method and its Application in Computational Materials Science,” *Computational Material Science,* vol. 125, pp. 243-254, 2016.

[130] G. L. W. Hart, V. Blum, M. J. Walorski, and A. Zunger, “Evolutionary Approach for Determining First-Principles Hamiltonians,” *Nature Materials,* vol. 4, pp. 391- 394, 2005.

[131] M. Malik, K.H. Chan and G. Azimi, “Review on the synthesis of LiNi xMnyCo 1-x-yO 2 (NMC) cathodes for,” *Materials Today Energy,* vol. 28, p. 101066, 2022.

[132] Q. Chen, A.J. Rondinone, B.C. Chakoumakos and Z.J. Zhan, " Synthesis of super paramagnetic $MgFe_2O_4$ nanoparticles by coprecipitation," *Journal of Magnetism and Magnetic Materials*, vol. 194, pp. 1-7, 1999.

[133] H. Li. Q. Xu, X.X. Shi, D.W. Song and L.Q. Zhan, "Electrochemical performance of $LiNi_{0.5}Mn_{0.5}O_2$ with different synthesis methods," *Rare Metals*, vol. 34, pp. 580-585, 2015.

[134] D. Wang, I. Belharouak, G.M. Koenig, G. Zhou and K. Amin, " Growth mechanism of $Ni_{0.3}Mn_{0.7}CO_3$ precursor for high capacity Li-ion battery cathodes," *Journal of Material Chemistry*, vol. 21, pp. 9290-9295, 2011.

[135] Z. Xu, L. Xiao, F. Wang, K. Wu, L. Zhao, M.R. Li, H.L. Zhang, Q. Wu and J. Wang, *Journal of Power Sources*, vol. 248, pp. 180-189, 2014.

[136] J. Li, M. Zhang, D. Zhang, Y. Yan, Z. Li and Z. Nie, "Effect of sintering conditions on electrochemical properties of $LiNi_{0.8}Co_{0.1}Mn_{0.1}O_2$ as cathode material," *International Journal of Electrochemical Science*, vol. 15, pp. 1881-1892, 2020.

[137] J. Li, M. Zhang, D. Zhang, Y. Yan, Z. Li and Z. Nie, "e, Effect of sintering conditions on electrochemical properties of $LiNi_{0.8}Co_{0.1}Mn_{0.1}O_2$ as cathode material," *International Journal of Electrochemical Science*, vol. 15, pp. 1881-1892, 2020.

[138] S. Zhang, C. Deng, B. Fu, S. Yang and L. Ma, ", Synthetic optimization of spherical $Li[Ni_{1/3}Mn_{1/3}Co_{1/3}]O_2$ prepared by a carbonate co-precipitation method," *Power Technology*, vol. 198, pp. 373-380, 2010.

[139] J.Z. Kong, F. Zhou, C.B. Wang, X.Y. Yang, H.F. Zhai, H. Li, J.X. Li, Z. Tang and S.Q. Zhang, " Effects of Li source and calcination temperature on the electrochemical

properties of $LiNi_{0.5}Co_{0.2}Mn_{0.3}O_2$ lithium-ion cathode materials," *Journal of Alloys Compound*, vol. 554, pp. 221-226, 2013.

[140] K. Wu, F. Wang, L. Gao, M.-R. Li, L. Xiao, L. Zhao, S. Hu, X. Wang, Z. Xu and Q. Wu, "Effect of precursor and synthesis temperature on the structural and electrochemical properties of Li $(Ni_{0.5}Co_{0.2}Mn_{0.3})O_2$," *Electrochimica Acta*, vol. 75, pp. 393-398, 2012.

[141] Z. Xu, L. Xiao, F. Wang, K. Wu, L. Zhao, M.-R. Li, H.-L. Zhang, Q. Wu and J. Wang, *Journal of Power Sources*, vol. 248, pp. 180-189, 2014.

[142] L. Liang, K. Du, Z. Peng, Y. Cao, J. Duan, J. Jiang and G. Hu,, "Co-precipitation synthesis of $Ni_{0.6}Co_{0.2}Mn_{0.2}(OH)_2$ precursor and characterization of LiNi0. 6Co0. 2Mn0. 2O2 cathode material for secondary lithium batteries," *Electrochimica Acta*, vol. 130, pp. 82-89, 2014.

[143] H. Dong and G.M. Koenig Jr, ", Compositional control of precipitate precursors for lithium-ion battery active materials: role of solution equilibrium and precipitation rate," *Journal of Material Chemistry*, vol. 5, pp. 13785-13798, 2017.

[144] N. Ngoepe, A. Gutierrez, P. Barai, J. Chen, P.E. Ngoepe and J.R. Croy, "The effect of process parameters on the properties of manganese-rich carbonate precursors: A study of co-precipitation synthesis using semi-batch reactors," *Argon National Laboratory*, pp. 5-6, 2021.

[145] B. Ravel and M. Newville, "X-ray absorption spectroscopy and related techniques," *Early View Articles*, vol. 1, 2020.

[146] Z. Wu, W.K. Pang, L. Chen, B. Johannessen and Z. Guo, “In Situ synchrotron x-ray absorption spectroscopy studies of anode materials for rechargeable batteries,” *Batteries&Supercaps,* vol. 10, 2021.

[147] J. Furthmüller and G. Kresse, “Efficient Iterative Schemes for Ab Initio Total-Energy Calculations using a Plane-Wave Basis Set,” *Physical Review,* vol. 54, pp. 11169-12150, 1996.

[148] P.E. Blochl, “Projector Augmented-Wave Method,” *IBM Research Division, Zurich Research Laboratory,* vol. 50, pp. 17953-17979, 1994.

[149] G. Kresse and D. Joubert, “From Ultrasoft Pseudopotentials to the Projector Augmented-Wave Method,” *Physical Review B,* vol. 59, pp. 1758-1856, 1999.

[150] H.S. Cheng, “Elasic Anisotropy of Metals,” *Metallurgy Industry Press, Beijing,* p. 20, 1996.

[151] F. Mouhat and F.X. Coudert, “Necessary and Sufficient Elastic Stability Conditions in Various Crystal Systems,” *Physical Review,* vol. 90, pp. 224104-234405, 2014.

[152] L. Kantorovich, “Quantum Theory of the Solid State: An introduction, London,” *Kluwer Academic Publishers,* vol. 65, pp. 10244-10201, 2014.

[153] R. Hill, “The Elastic Behaviour of a Crystalline Aggregate,” *Proceedings of the Physical Society, Section A,* vol. 65, pp. 349-355, 1952.

[154] A. Reuss and Z. Angew, “Calculation of the Flow Limits of Mixed Crystals on the Basisof the Plasticity of Monocrystals.,” *Zeitschrift fur Angewandte Mathematik und Mechanik,* vol. 9, pp. 49-58, 1929.

[155] W. Voigt, “Lehrbuch der Kristallpysik Taubner,” *Leipzig,* vol. 213, pp. 29-35, 1928.

[156] S.F. Pugh, “Relations Between Elastic Moduli and the Plastic Properties of Polycrystalline Pure Metals.,” *The Philosophical Magazine,* vol. 45, pp. 823-843, 1954.

[157] K. Lau, “Elastic Anisotropy Factors for Orthorombic, Tetragonal and Hexagonal Crystals,” *Physical Review B,* vol. 58, pp. 8981-8984, 1998.

[158] R.J. Bosco and B.G. Jeyaprakash, “Lattice Vibrations, Phonons, Specific Heat Capacity, Thermal Conductivit,” *School of Electrical & Electronics Engineering,* vol. 5, pp. 20-24, 2007.

[159] N.W. Ashcroft and N.D. Mermin, “Solid States Physics,” *New York Holt, Rinehart and Winston,* vol. 8, pp. 826-833, 1976.

[160] K. Parlinski and Y. Kawazoe, “Ab Initio Study of Phonons in Hexagonal GaN,” *Physical Review B,* vol. 60, pp. 15511-15628, 1999.

[161] O.E. Alon and L.S. Cederbaum, “Degenerate Perturbation Theory,” *Physical Review B,* vol. 68, pp. 3310-3430, 2003.

[162] J.M. Zheng, P.F. Yan, J.D. Zhang.,et al, “Suppressed oxygen,” *Nano Res,* vol. 10, p. 4221–423, 2017.

[163] A.K. Lavery, B.W. Hona, R.K. Sapkota, N.K. Koralalage, M. Adeniran, A. Ajayi, B.P. Zain, M.A. Wang, H. Druffel et al, “Mn-Rich NMC Cathode for Lithium-Ion Batteries at,” *Energies (MDPI),* vol. 15, pp. 1-14, 2022.

[164] A.S. Prakash and K.R. Prakasha, “Time and energy conserving solution combustion synthesis of nano $Li_{1.2}Ni_{0.13}Mn_{0.54}Co_{0.13}O_2$ cathode material and of nano $Li_{1.2}Ni_{0.13}Mn_{0.54}Co_{0.13}O_2$ cathode material and of nano $Li_{1.2}Ni_{0.13}Mn_{0.54}Co_{0.13}O_2$ cathode material and its performance in Li-ion batteri,” *RSC Advances,* vol. 00, pp. 5-6, 2015.

[165] S. Jeong, S. Park, M. Beak, J. Park, J.S. Park and K. Kwon, “Effect of residual trace amounts of Fe and Al in $Li[Ni_{1/3}Mn_{1/3}Co_{1/3}]O_2$ cathode active material for the sustainable recycling of lithium ion batteries,” *Materials,* vol. 14, no. 9, p. 2464, 2021.

[166] M.A. Hannan, M.S.H. Lipu, A. Hussain and A. Mohamed, “A review of lithium-ion battery state of charge estimation and management system in electric vehicle applications: Challenges and recommendations,” *Renewable and sustainable energy reviews,* vol. 78, pp. 834-845, 2017.

[167] J. Arai, T. Yamaki, S. Yamauchi, T. Yuasa, T. Maeshima, T. Sakai, M. Koseki and T. Horiba, “Development of high power lithium secondary battery for hybrid electric vehicles,” *Journal of power sources,* vol. 146, pp. 788-792, 2005.

[168] M.A. Hannan, M.M. Hoque, A. Mohamed and A. Ayob, “Review of energy storage systems for electric vehicle applications: Issues and challenges,” *Renewable and Sustainable Energy Reviews,* vol. 69, pp. 771-789, 2017.

[169] V. Etacheri, R. Marom, R. Elazari, G. Salitra and D. Aurbach, “Challenges in the Development of Advanced Li-ion Batteries: A Review,” *Energy Environmental Science,* vol. 4, pp. 3243-3262, 2011.

[170] C.M. Julien, A. Mauger, K. Zaghib and H. Groult, “Comparative Issues of Cathode Materials for Li-Ion Batteries,” *Inorganics,* vol. 2, pp. 132-154, 2014.